Experimental investigation of methods to improve the field gradient produced by a superconducting Halbach array

Auteur : Kollasch, Killian
Promoteur(s) : Vanderbemden, Philippe
Faculté : Faculté des Sciences appliquées
Diplôme : Master en ingénieur civil physicien, à finalité approfondie
Année académique : 2024-2025
URI/URL : http://hdl.handle.net/2268.2/23369

Academic year 2024-2025

University of Liège - Faculty of Applied Sciences

Experimental investigation of methods to improve the field gradient produced by a superconducting Halbach array

Master thesis submitted in fulfilment of the requirements for the degree of Master in Engineering Physics by Killian Kollasch

Author
Kollasch Killian

Supervisor
Prof. P. Vanderbemden

Jury
Prof. B. Vanderheyden
Prof. T. Gilet
Prof. J-M. Redouté

Acknowledgements

I would first like to express my sincere gratitude to my supervisor, Professor Philippe Vanderbemden, for his invaluable guidance, constant support, and availability throughout the entire year. His expertise and encouragement were essential at every stage of this project.

I am also deeply grateful to Dr Jean-François Fagnard, who was always willing to answer even the smallest questions during experimental procedures, and who provided invaluable assistance in the fabrication of various components. My thanks also go to Mr Pascal Harmeling for his helpful insights and for answering all questions related to mechanical aspects.

I warmly thank Dr Michel Houbart for allowing me to use his experimental setup and for his consistent availability whenever I needed help or clarification.

I would also like to express my appreciation to Mr Calderon Jimenez Angel, who produced the new parts required for additional experiments, and to Thor and Nicolas for their unfailing good humour and the support they provided throughout this work. I am particularly grateful for the numerous trips they made to collect liquid nitrogen — a substance I used in large quantities.

Lastly, I wish to extend my heartfelt thanks to my family and friends, whose unwavering support and encouragement sustained me throughout this journey. Their advice, patience, and presence have been invaluable.

A sincere and warm thank you to all of you.

Abstract

This Master's thesis investigates the enhancement of magnetic field gradients using superconducting Halbach arrays, with the ultimate aim of improving applications such as magnetic drug targeting. While Halbach arrays made of permanent magnets offer enhanced magnetic fields compared to single magnets, their performance is fundamentally limited by magnetic saturation. To overcome this, the study explores the use of bulk high-temperature superconductors (HTS), which can trap significantly stronger magnetic fields.

Two novel configurations are experimentally tested: the elevated Halbach array, designed to reduce central demagnetisation, and the five-superconductor Halbach array, aimed at increasing the field gradient despite expected demagnetisation. Theoretical models based on electromagnetism and Biot-Savart's law are developed and adjusted to account for defects within superconducting samples. Comparisons between experimental measurements and simulations reveal the influence of demagnetisation, sample geometry, and material defects on the magnetic field profile.

The results confirm that superconducting Halbach arrays can generate higher magnetic gradients than their permanent magnet counterparts. These findings open perspectives for designing more efficient magnetic assemblies in medical and engineering applications, with future work suggested on optimising sample alignment and geometry.

Contents

List of Figures

CHAPTER 1

Introduction

1.1 Motivations

Drug delivery is a method studied in order to target specific regions in the body with certain compounds. For instance, this method is investigated for cancer treatment [1]. Nowadays, chemotherapy is used to try to destroy cancerous cells. However, this method requires a large amount of drugs that are distributed throughout the body. As a result, the drug attacks both cancerous and healthy cells, leading to side effects for the patient. By using drug delivery methods, the drug can be transported directly to cancerous cells and only affect them. This method offers at least two benefits. First, it reduces side effects, as the drug is delivered only to the tumour. Second, fewer agents are needed, as the treatment is targeted solely at the cancerous cells. One way to achieve this precise delivery is by using magnetic drug targeting (MDT). The drug is attached to a biocompatible magnetic nanoparticle. A force can be applied to this nanoparticle by placing it in a magnetic field. More precisely, the force exerted on the nanoparticles is proportional to the gradient of the magnetic field $\nabla||\vec{B}||$ [2, 3]. This method is illustrated in Fig. 1.1 (a). This magnetic field can come from a permanent magnet such as Nd-Fe-B, fixed outside the body [4].

Using a single magnet is possible, but performance can be improved by employing a configuration of permanent magnets known as a Halbach array. This configuration was introduced in 1973 by J. C. Mallison [5] and later studied by K. Halbach [6, 7] for several arrangements. It has the distinctive feature of having a strong side, where the magnetic field is high, and a weak side, where the magnetic field is significantly lower, almost zero. A basic configuration of three permanent magnets is illustrated in Fig. 1.1 (b). As it increases both the magnetic field and its gradient, Halbach arrays are used in various applications such as brakes, brushless motors, Maglev trains, and particle separation [8–12]. Moreover, Halbach arrays are also studied for magnetic drug targeting, both numerically and experimentally, with permanent magnets, showing an increase in the magnetic field gradient [13].

The main limitation of permanent magnets is due to magnetic saturation. Each type of magnet has a saturation field that cannot be exceeded. For Nd-Fe-B, this saturation field is approximately 1.5 T [14–16]. One idea to overcome this limitation is to use superconductors, and more specifically, bulk

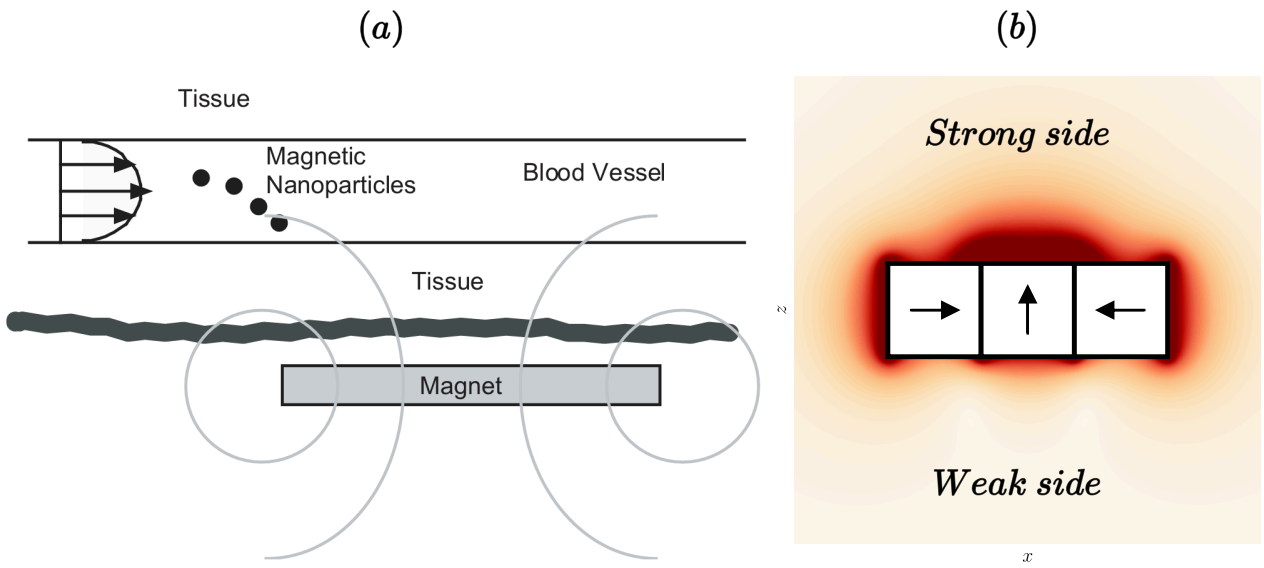

Figure 1.1: (a) Schematic illustration of drug delivery using magnetic nanoparticle and directed by a magnet. Schematic illustration from [4]. (b) Illustration of the magnetic field of an Halbach array with the indication of the strong and weak side.

superconductors. These bulks are capable of trapping a magnetic field through a specific magnetisation procedure. They can be used in various applications such as flywheels, motors, or magnetron sputtering devices [17–19]. So far, a maximum magnetic field of 17.6 T has been achieved with YBCO superconductors at 29 K [20]. Compared to permanent magnets, this represents an increase of approximately one order of magnitude in magnetic field strength, highlighting the significant potential of bulk superconductors.

The design and fabrication of Halbach arrays using bulk superconductors were studied in the PhD thesis of M. Houbart [21]. The experimental results of superconducting Halbach arrays with 3 cubic superconductors shows an improvement in the magnetic field and its gradient. However, a demagnetisation process occurs in the central sample as the samples are brought closer together. This demagnetisation leads to a lower magnetic field than expected. In this PhD thesis, several perspectives were proposed to further increase the field gradient generated by the superconducting Halbach array, including using an array with an offset between the central and the side samples, or using a larger Halbach arrays.

1.2 Goals and outline

The goal of this master thesis is to experimentally study two new configurations proposed in [21]. The thesis is organised as follows:

- Chapter 2 explains the theoretical background of magnetism and the specific properties of superconductors. Additionally, a model for the magnetic field is presented in order to compare it with the magnetic field measured during the different experiments.
- Chapter 3 is dedicated to the characterisation of permanent magnets and superconductors. As some defects may occur in the superconducting samples, the model developed in Chapter 2 is modified to take these defects into account.
- Chapter 4 is a study of linear Halbach arrays. This chapter highlights the differences between

permanent magnets and superconductors. Moreover, it focuses on the demagnetisation process, demonstrating its impact on the magnetic field.

- Chapter 5 investigates two new configurations. The first configuration, called the elevated Halbach array, is designed so that no demagnetisation is expected in the central superconductor. The second configuration, called the linear Halbach array with five samples, involves assembling five samples into a Halbach array to increase the magnetic field. In this configuration, demagnetisation is expected. A brief discussion is also included about ideal cases and the importance of the size of the superconductor and the permanent magnet.
- Chapter 6 concludes the results presented in this master thesis. And some ideas of perspectives are proposed.

CHAPTER 2

Theoretical background and analytical model

2.1 Electromagnetism

Electromagnetism is described by Maxwell's equations,

$$\vec{\nabla} \times \vec{H} = \vec{J} + \frac{\partial \vec{D}}{\partial t}, \tag{2.1}$$

$$\vec{\nabla} \times \vec{E} = -\frac{\partial \vec{B}}{\partial t}, \tag{2.2}$$

$$\vec{\nabla} \cdot \vec{B} = 0, \tag{2.3}$$

$$\vec{\nabla} \cdot \vec{D} = \rho. \tag{2.4}$$

The first equation (Eq. 2.1) is the Ampère-Maxwell law. It describes the fact that a magnetic field $\vec{H}$ [A/m] can be generated from two sources: a current density $\vec{J}$ [A/m^2] or a time-varying electric displacement field $\vec{D}$ [C/m^2]. The second equation (Eq. 2.2) corresponds to the Maxwell-Faraday law. It states that a time-varying magnetic flux density $\vec{B}$ [T] induces an electric field $\vec{E}$ [V/m]. The third equation (Eq. 2.3) is the Maxwell-Thomson law, which states that there are no magnetic monopoles, only dipoles. As a result, the magnetic flux density is described by field lines that always form closed loops. The last equation (Eq. 2.4) states that a charge density ρ [C/m^3] generates an electric field.

To solve these equations and to link the vector fields between them, some constitutive equations are needed. In a conventional conductor, these constitutive equations are:

$$\vec{B} = \mu \vec{H} \tag{2.5}$$

$$\vec{D} = \varepsilon \vec{E} \tag{2.6}$$

$$\vec{E} = \frac{1}{\sigma} \vec{J}, \tag{2.7}$$

where three physical parameters appear: the magnetic permeability μ [H/m], the electric permittivity ε [F/m], and the conductivity σ [S/m]. These characteristics depend on the material used and can vary with temperature, pressure, frequency, humidity, etc. If these equations are considered in a vacuum,

we have $\mu = \mu_0 = 4 \times 10^{-7}$ H/m, $\varepsilon = \varepsilon_0 = 8.85 \times 10^{-12}$ F/m, and $\sigma = 0$ S/m. All these equations (Maxwell's equations and the constitutive equations) can be used to derive two wave equations, one for the electric field $\vec{E}$ and one for the magnetic field $\vec{H}$, which describe the behaviour of an electromagnetic wave in a given medium.

In many applications, one of the two fields ($\vec{E}$ or $\vec{H}$) is predominant, and the energy is primarily stored in that field. This assumption is known as the quasi-static approximation, which is valid when the characteristic length l of the system under study is much smaller than the wavelength of the electromagnetic field. This leads to two different behaviours depending on whether the dominant field is electric or magnetic. Since we are interested in superconductors, we will consider the case of a "good" conductor, where the dominant field is $\vec{H}$. A criterion to determine whether a system is in the magnetoquasistatic regime rather than the electroquasistatic regime is $\sigma > \frac{1}{l}\sqrt{\frac{\varepsilon}{\mu}}$ [22]. This explains why we consider a good conductor: because of its high conductivity σ compared to an insulator. The derivation of the magnetoquasistatic regime leads to a diffusion equation. For example, if we consider an infinite slab of thickness $2a$, the magnetic field will penetrate the normal conductor with a characteristic length known as the skin depth, $\delta = \sqrt{\frac{2}{\sigma \mu \omega}}$, where ω is the angular frequency [rad/s].

2.2 Superconductors

2.2.1 The zero resistance property

In 1911, Kamerlingh Onnes discovered superconductivity. He made this discovery by measuring the electrical resistance of mercury at cryogenic temperatures and observed that the resistance dropped to zero at a temperature around 4.2 K, as shown in Fig. 2.1. Over the years, other elements were found to exhibit superconducting behaviour at different temperatures at which the resistance drops, such as 7.2 K for Pb and 9.25 K for Nb. The temperature at which this drop occurs is called the critical temperature and is denoted by T_C.
Due to the zero resistance, the conductivity σ in Ohm's law (Eq. 2.7) should tend to infinity, which is not physically possible. For type I superconductors (the difference between type I and type II is explained in Sec. 2.2.3), this constitutive equation must be replaced. The new constitutive equation is London's first equation,

$$\vec{E} = \frac{\partial}{\partial t}\left(\Lambda \vec{J}\right), \tag{2.8}$$

where $\Lambda = \frac{m_e}{n\, q_e^2}$, with m_e the mass of an electron, n the number density of electrons, and q_e the charge of an electron.

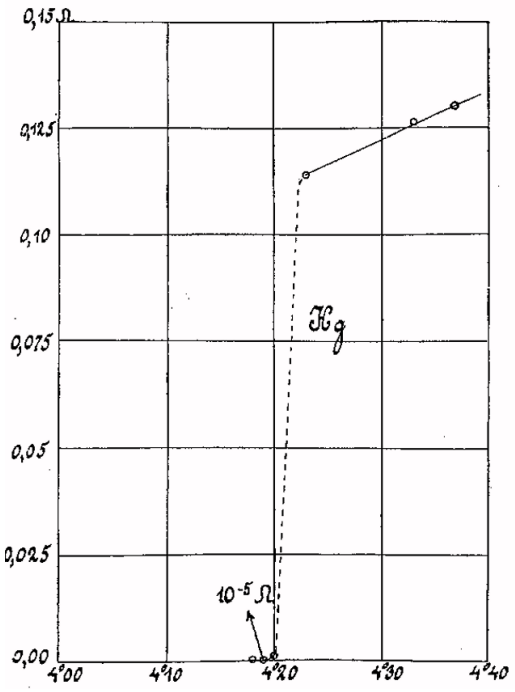

Figure 2.1: Representation of the zero resistance of mercury from [23].

This new constitutive equation is derived by considering the Drude model, which uses Newtonian mechanics without electrostatic interactions between electrons and without the effect of any magnetic flux density on electrons. This model introduces a time constant corresponding to the time between

two collisions for an electron, and this time tends to infinity in a superconductor, which leads to London's first Eq. 2.8.

The diffusion equation yields a similar type of solution as in a normal conductor, but with a characteristic length $\lambda = \sqrt{\frac{\Lambda}{\mu_0}}$, called the London penetration depth. In comparison, a normal conductor such as copper has a skin depth of around 1 cm at 50 Hz, while a superconductor has a London penetration depth of about 0.1 mm.

2.2.2 The Meissner effect

Up to now, superconductors have been considered as perfect conductors. However, in 1933, Meissner discovered that below the critical temperature, a superconductor expels all magnetic flux density from its interior and behaves as a perfect diamagnetic material. This phenomenon is known as the Meissner effect. The difference with a perfect conductor can be observed in Fig. 2.2, where two experiments are carried out. Experiment 1 consists of cooling down the sample and then applying a magnetic field. In both cases, perfect conductor and superconductor, the magnetic flux density is expelled from the sample (except within a thin layer of thickness λ). This procedure is called zero-field cooling (ZFC). Experiment 2 is the reverse: first, a magnetic field is applied, then the sample is cooled down below the critical temperature. In this case, there is a clear difference. The magnetic flux density remains trapped in the perfect conductor but is expelled from the superconductor. This method is called field cooling (FC). To describe this property, another equation is needed: London's second equation,

$$\nabla \times \left(\Lambda \vec{J}\right) = -\vec{B} \tag{2.9}$$

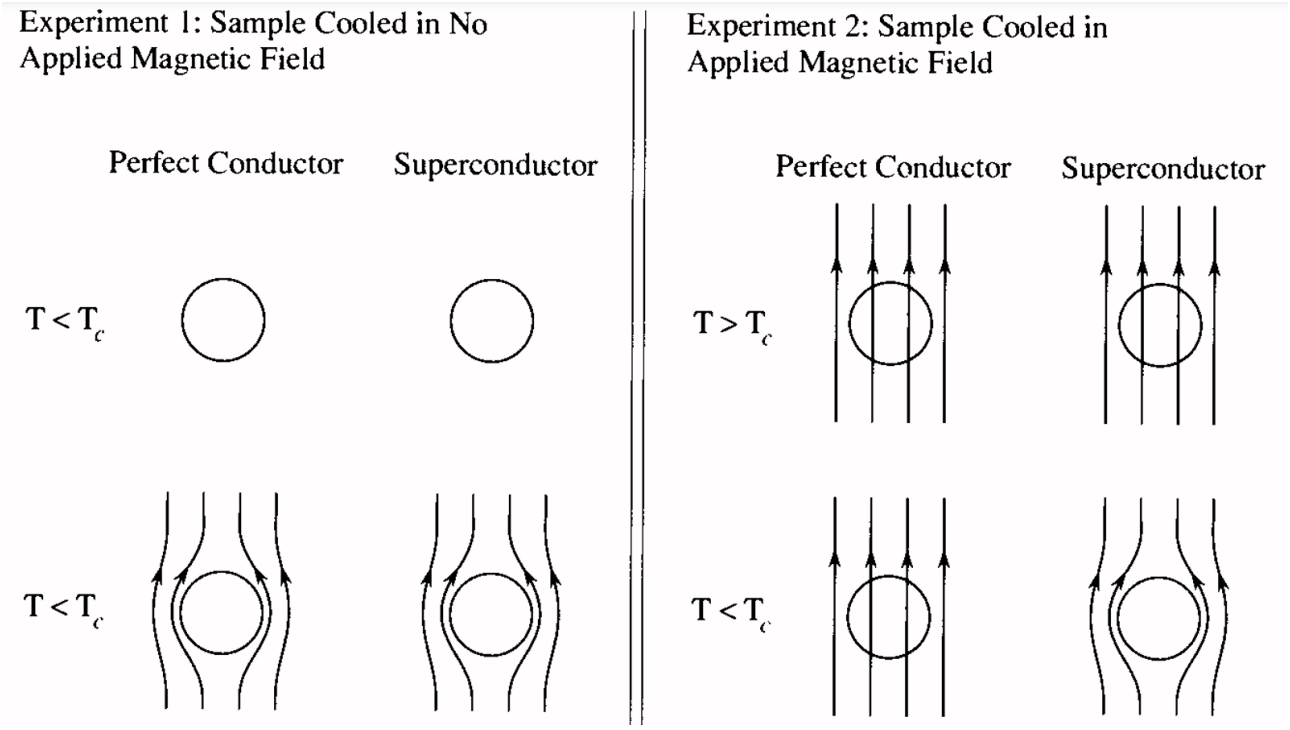

Figure 2.2: Schematic illustration of two experiments, zero-field cooling (ZFC) on the left, experiment 1, and the field cooling (FC) on the right, experiment 2, for both perfect conductor and superconductor. Illustration from [22].

2.2.3 Types of superconductors

As mentioned, superconducting samples become superconductor when a critical temperature falls below a certain critical value. However, temperature is not the only parameter that must remain below a threshold. In fact, the magnetic field $\vec{H}$ and the current density $\vec{J}$ also have an impact and must remain below their respective critical values, H_c and J_c. These two critical values depend on temperature, and also on each other. They can be expressed as $\vec{J}_c(\vec{H}, T)$ and $\vec{H}_c(\vec{J}, T)$. This allows the definition of a critical surface in the ($\vec{H}$, $\vec{J}$, T) space, which represents the boundary between the superconducting and non-superconducting states. For instance, the vector quantities $\vec{H}$ and $\vec{J}$ can be reduced to their norms $H = ||\vec{H}||$ and $J = ||\vec{J}||$. The corresponding critical surface is illustrated in Fig. 2.3.

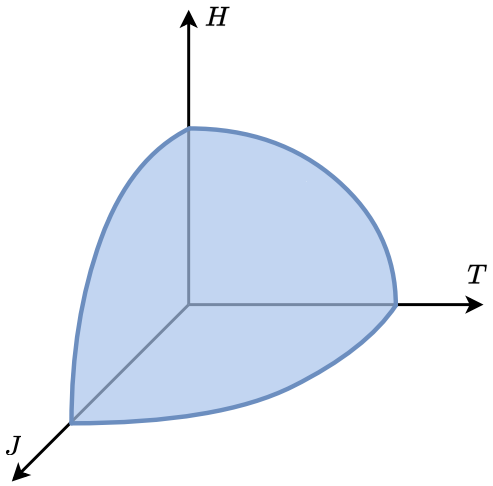

Figure 2.3: Schematic illustration of the (H,J,T) surface for an isotropic superconductor.

Superconductors can be categorised into two types: type I and type II. Type I superconductors exhibit a single phase transition, passing directly from the normal state to the Meissner state. Type II superconductors, on the other hand, undergo two phase transitions. In addition to the normal and Meissner states, they also exhibit an intermediate phase known as the mixed state or vortex state. Due to these two phase transitions, type II superconductors are characterised by two critical magnetic fields: H_{c1} and H_{c2}. This distinction is illustrated in Fig. 2.4, an additional parameter appears H_{irr} and is discussed in Sec. 2.2.5.

In the mixed state, vortices appear. Vortices are normal cores of typical size $\xi = 100$ nm, around which a current circulates. Each vortex carries a quantised magnetic flux $\Phi_0 \approx 2 \times 10^{-15}$ Wb, which results from two physical constants: Planck's constant h and the electron charge q_e, with $\Phi_0 = \frac{h}{2q_e}$. When a magnetic field increases and exceeds H_{c1}, vortices begin to enter the material. As the field continues to increase (but remains below H_{c2}), the number of vortices also increases. Vortices tend to repel each other, which often leads them to form a triangular lattice, as shown in Fig. 2.5. In a perfectly pure superconductor, meaning one without impurities or defects, vortices can move freely. As a result, if the applied magnetic field is reduced, they will disappear. However, if the goal is to magnetise the superconductor, it is necessary to retain these vortices even after the external magnetic field is removed. To achieve this, impurities are introduced into the material, creating what are known as pinning centres. These pinning centres are useful because when vortices are pinned to them, it becomes more difficult for the vortices to move or escape, allowing them to remain even when the external field is turned off. Because some vortices remain pinned and cannot be removed, the superconductor is said to exhibit an irreversible behaviour.

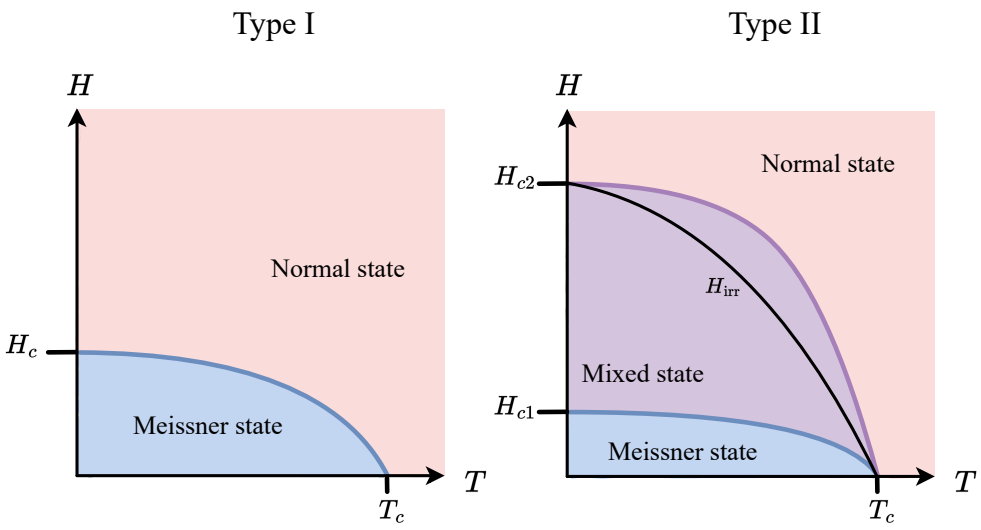

Figure 2.4: Schematic illustration of the difference between a type I and a type II superconductors.

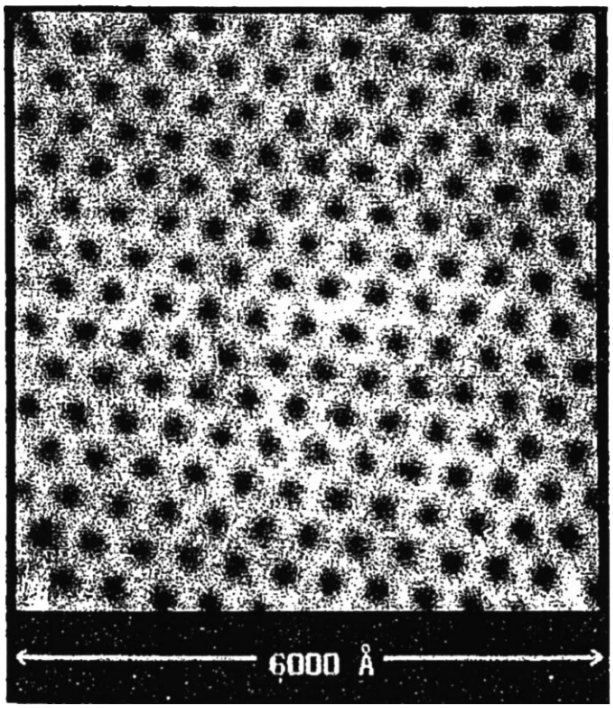

Figure 2.5: Picture of vortices in $NbSe_3$ from [24].

Type II superconductors can be classified into two sub-categories. The first, low-temperature superconductors (LTS), refers to superconductors with a critical temperature below approximately 30 K. Examples include NbTi and Nb_3Sn. The second type is called high-temperature superconductors (HTS). HTS are superconductors whose critical temperature is above 30 K, and most often 77 K. Thanks to this relatively high critical temperature, HTS materials can be cooled using liquid nitrogen. Common examples include $YB_2Cu_3O_7$, $Bi_2Sr_2CaCu_2O_8$, and $Bi_2Sr_2Ca_2Cu_3O_{10}$. These materials contain CuO planes, referred to as a-b planes. These planes are important because the current density in the superconductor tends to flow preferentially within them, leading to an anisotropic behaviour. The direction perpendicular to the a-b planes is called the c-axis.

2.2.4 The Bean model

In order to model superconductors, a model was proposed in 1962 by Charles P. Bean [25, 26]. This model is based on the assumption of strong pinning. This means that a large number of pinning centres prevent the vortices from moving. These pinning centres are assumed to be uniformly distributed, and the current reaches its maximum value, i.e., $||\vec{J}|| = J_c$. Under this assumption, the local form of Biot–Savart's law can be written as:

$$||\nabla \times \vec{B}|| = \mu_0 J_c. \tag{2.10}$$

In the simplest case, J_c is considered independent of $||\vec{B}||$, meaning its scalar value is either J_c, $-J_c$, or 0 A/m^2. Additionally, another simplification is made concerning the two critical magnetic fields: H_{c1} is assumed to tend to zero, and H_{c2} tends to infinity. With these assumptions in place, let us reconsider the two previously mentioned experiments (zero-field cooling and field cooling) to illustrate this model for an infinite slab extending along the y and z directions, with a thickness $2a$ along the x-axis and a magnetic field applied along the z direction.

Bean model applied to the zero field cooling case

Because this example considers an infinite slab along y and z, the Biot-Savart law can be simplified as

$$\frac{\partial B}{\partial x} = \pm \mu_0 J_c \text{ or } 0. \tag{2.11}$$

Which means that the space variation along x of B is directly linked to the critical current density.

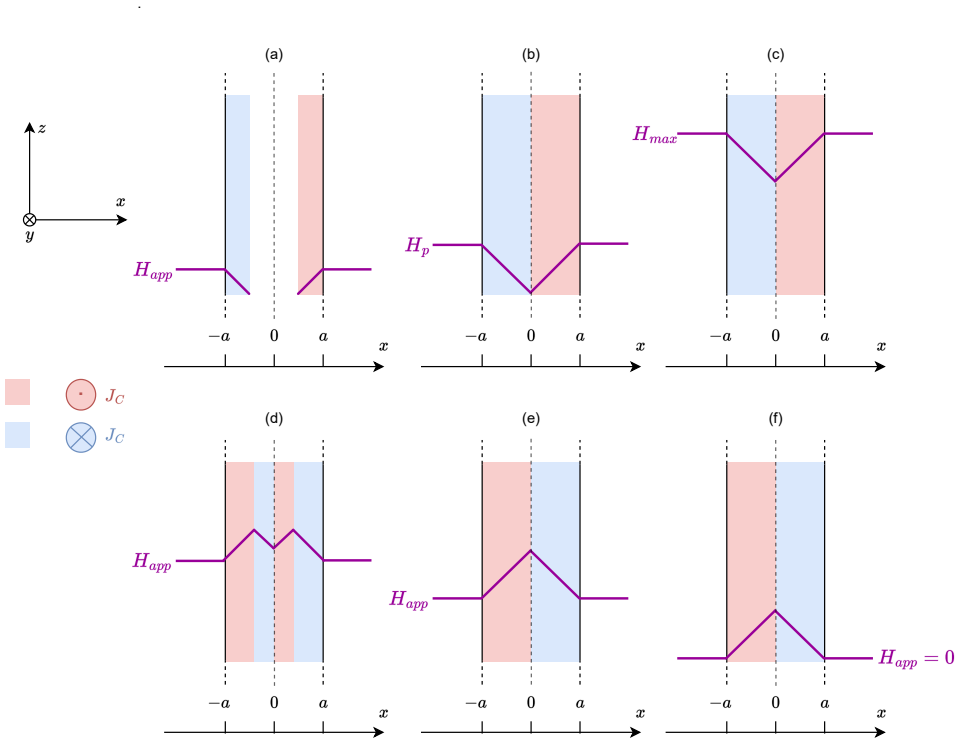

Figure 2.6: Schematic illustration of the Bean model applied in the zero field cooling conditions. The applied field H_{app} is along z, the current is flowing in the y direction. For the (a), (b), (c) case the applied magnetic field is increased utile H_{max} in (c) and for (d), (e), (f) is applied field is decreased until 0 for (f). H_p represents the penetration magnetic field which is the field we need to apply so that the field penetrates up to the center of the superconductor.

Fig. 2.6 shows a schematic illustration of the Bean model for the zero-field cooling (ZFC) procedure. The magnetic field is applied along the z-direction. During the first three steps (a, b, c), the applied magnetic field is gradually increased up to a maximum value $H_{\max}$. In step (b), the magnetic field reaches H_p, known as the penetration field, which is given by:

$$H_p = \frac{\mu_0 J_c a}{2}. \tag{2.12}$$

It represents the magnetic field required for the flux to fully penetrate into the core of the superconductor. Step (f) corresponds to the moment when the superconductor is fully magnetised and a magnetic field is trapped inside it. To magnetise the superconductor and trap magnetic flux effectively, the applied magnetic field must reach at least twice the penetration field.

Bean model for the field cooling case

Eq. 2.11 is still valid for the field cooling (FC) procedure. Fig. 2.7 illustrates the FC case. The main difference from the ZFC case is that the maximum magnetic field required to magnetise the superconductor is no longer twice the penetration field, but only once. In other words, the applied magnetic field needs to reach H_p instead of $2H_p$. Because this procedure requires a lower maximum magnetic field to magnetise the superconductor, it is generally preferred. For both methods, the mean remaining magnetic field is given by:$\langle B \rangle = \mu_0 \frac{H_p}{2}$, in the case of an infinite slab.

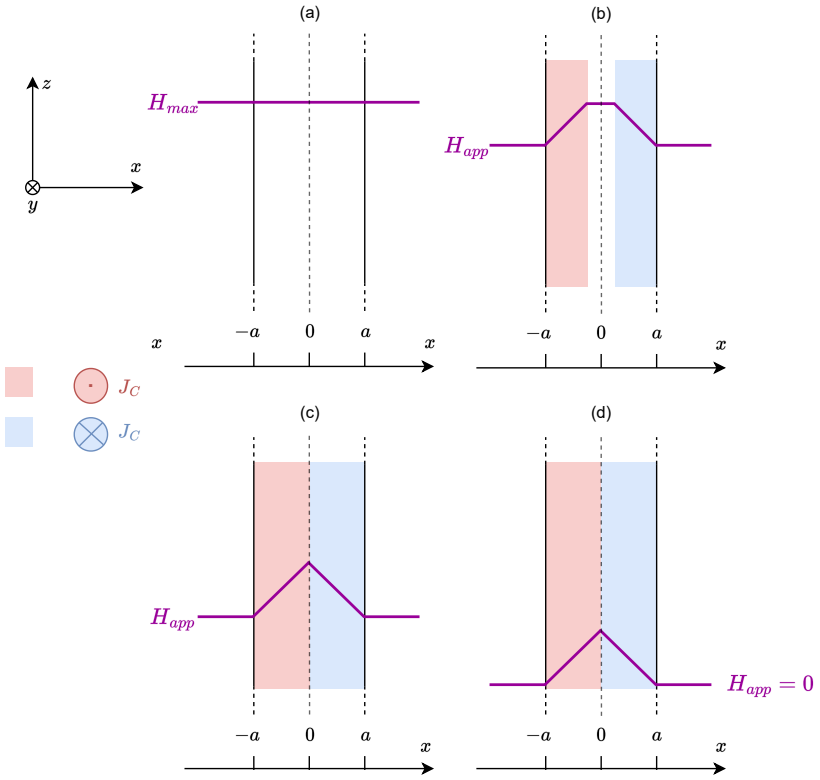

Figure 2.7: Schematic illustration of the Bean model applied in the field cooling conditions. The applied field H_{app} is along z, the current is flowing in the y direction. For the (a), (b), (c), (d) case the applied magnetic field is decreased utile 0. In (a) H_{max} represents the applied field at the beginning of the magnetization process.

2.2.5 Power law and flux creep

The Bean model is an idealised model in which vortices are assumed to be immobile due to strong pinning. However, two phenomena can cause vortices to move: the flux flow regime and flux creep. The flux flow regime occurs when vortices are set into motion by a force. This force, known as a Lorentz-like force, arises from the interaction between the current density and an external magnetic field. If this Lorentz-like force exceeds the force exerted by the pinning centres, vortices are able to move within the superconducting material. Since vortices are normal cores that carry magnetic flux, their motion induces a time-dependent variation of the magnetic flux density at a given point. According to Faraday's law, described by Eq. 2.2, this variation generates an electric field. Because this electric field and the current density are in phase, their interaction produces power dissipation and thus energy losses in the system. These losses can be characterised by a resistivity, referred to as the flux flow resistivity ρ_{ff}. For a given current density, the maximum magnetic field at which the material remains in the pinned state, before entering the flux flow regime, is denoted by H_{irr}, as shown in Fig. 2.4. When the magnetic field is greater than H_{irr} but still below H_{c2}, the superconductor is in the mixed state, but vortices can move. This is known as the reversible regime. Therefore, the important upper magnetic field limit is not H_{c2} but H_{irr}, as it defines the threshold beyond which the superconductor can no longer trap magnetic flux effectively. This regime is illustrated in Fig. 2.8 (a). In this context, the critical current density is defined as the current density at which the Lorentz-like force exceeds the pinning force and initiates vortex motion.

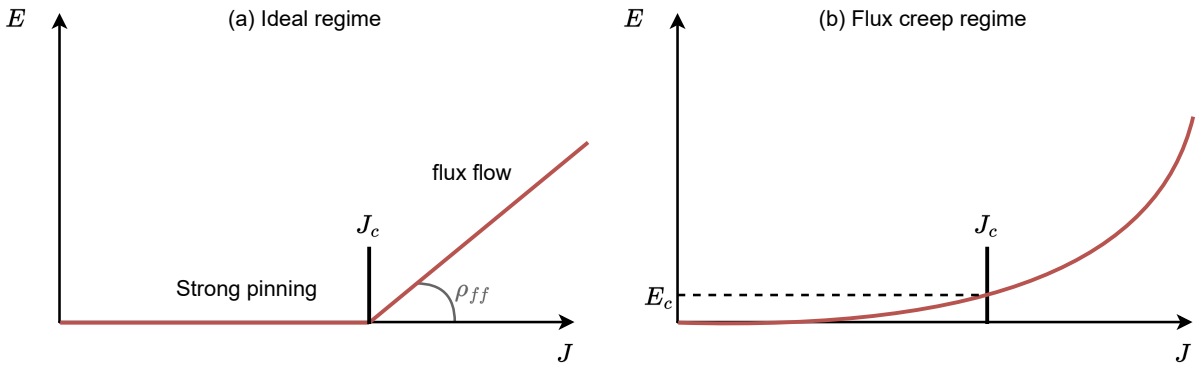

Figure 2.8: Schematic illustration between the strong pinning assumption (a), and the flux creep regime (b).

Even when the Lorentz-like force is insufficient to overcome the pinning force, there remains a probability that vortices move due to thermal fluctuations. This phenomenon is known as flux creep. As a result, the ideal E–J curve shown in Fig. 2.8 (a) becomes unrealistic, whereas Fig. 2.8 (b) offers a more accurate representation. For the flux creep regime, the definition J_c as the vortices moves is not longer possible. To define J_c in this context, a threshold electric field is introduced. A commonly used criterion is $E_C = 1\ \mu\text{V/cm}$, as mentioned in [27, 28].

Because vortices that are unpinned can move, they can also leave the material. As they leave the material, the number of vortices decreases, and thus the average magnetic flux density trapped in the superconductor also decreases.

This decay can be modelled as shown in [29]:

$$B(x,t) = B(x,t_0)\left(1+\frac{t}{t_0}\right)^{\frac{1}{1-n}}, \tag{2.13}$$

where t_0 is the time at which the measurement begins, and n is a material-dependent parameter. The parameter n can be determined experimentally and typically lies between 20 and 50 [30, 31]. Eq. 2.13 shows that the magnetic flux density decreases over time, but this decrease becomes progressively slower. Because of this slowing decay, a waiting period is introduced after the magnetisation process to ensure that the magnetic flux density can be considered stable. This period, known as the relaxation time, is at least 45 minutes in the context of this master's thesis.

2.3 Analytical model

In the previous section, the case of an infinite slab was studied. In order to model the magnetic flux density generated by a permanent magnet or trapped in a superconductor, the Biot-Savart law is used for a parallelepiped geometry.

2.3.1 Biot-Savart law applied for a cubic permanent magnet

The magnetic field generated by a permanent magnet can be modelled as a surface current, denoted K_c [A/m]. The Biot–Savart law for a surface current is expressed as:

$$\vec{B} = \frac{\mu_0}{4\pi} \int\int_S \frac{\vec{K_c} \times (\vec{x_p} - \vec{x_m})}{||\vec{x_p} - \vec{x_m}||^3} \, ds, \tag{2.14}$$

where $\vec{x_m}$ represents the coordinate vector (x_m, y_m, z_m) in the magnet, $\vec{x_p}$ the coordinate vector (x_p, y_p, z_p) of the point P where the magnetic field is evaluated, and S is the surface over which the surface current density flows. To compute the magnetic field generated by a cubic magnet of side l, the magnet is divided into four subsections. These subsections correspond to the different directions of the surface current density. Fig. 2.9 illustrates the subdivision and the surface current density on one face of the magnet. For one subsection, Eq. 2.14 can be simplified into two equations, one along either x or y (due to symmetry), and one along z. These equations are:

$$B_x^{\text{sub}} = \frac{\mu_0}{4\pi} \int_{-\frac{l}{2}}^{\frac{l}{2}} \int_{-\frac{l}{2}}^{\frac{l}{2}} \frac{K_c \, (z_p - z_m)}{\left[(x_p - x_m)^2 + (y_p - y_m)^2 + (z_p - z_m)^2\right]^{3/2}} \, dy_m \, dz_m \tag{2.15}$$

$$B_z^{\text{sub}} = \frac{\mu_0}{4\pi} \int_{-\frac{l}{2}}^{\frac{l}{2}} \int_{-\frac{l}{2}}^{\frac{l}{2}} \frac{K_c \, (x_p - x_m)}{\left[(x_p - x_m)^2 + (y_p - y_m)^2 + (z_p - z_m)^2\right]^{3/2}} \, dy_m \, dz_m. \tag{2.16}$$

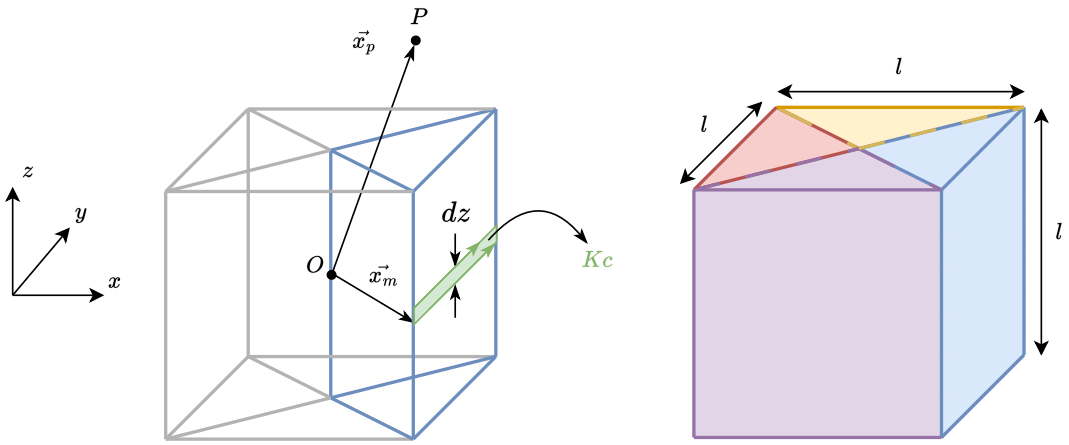

Figure 2.9: Schematic illustration of a sub section of the permanent magnet where a critical surface current density in flowing (left), and the 4 sub section of the cubic permanent magnet (right).

Eq. 2.15 and Eq. 2.16 are solved in Appendix A, assuming K_c is constant. The resulting expressions for B_x and B_z for a single subsection are:

$$B_x^{\text{sub}}(x_p, y_p, z_p) = -\frac{K_c \mu_0}{4\pi} \left[\left[\sinh \frac{y_p - y_m}{\sqrt{(x_p - \frac{l}{2})^2 + (z_p - z_m)^2}} \right]_{-\frac{l}{2}}^{\frac{l}{2}} \right]_{-\frac{l}{2}}^{\frac{l}{2}} = f(x_p, y_p, z_p) \tag{2.17}$$

$$B_z^{\text{sub}}(x_p, y_p, z_p) = -\frac{K_c \mu_0}{4\pi} \left[\left[\tan \frac{(y_p - y_m)(z_p - z_m)}{(x_p - \frac{l}{2})\sqrt{(x_p - \frac{l}{2})^2 + (y_p - y_m)^2 + (z_p - z_m)^2}} \right]_{-\frac{l}{2}}^{\frac{l}{2}} \right]_{-\frac{l}{2}}^{\frac{l}{2}} = g(x_p, y_p, z_p) \tag{2.18}$$

Eq. 2.17 and Eq. 2.18 can be developed to find the same expressions as in [21]. To obtain the total magnetic field components along x, y, and z (B_x, B_y, and B_z), the contributions from the four subsections are summed. Each component is given by:

$$B_x = f(x_p, y_p, z_p) - f(-x_p, -y_p, z_p) \tag{2.19}$$

$$B_y = f(y_p, -x_p, z_p) - f(-y_p, x_p, z_p) \tag{2.20}$$

$$B_z = g(x_p, y_p, z_p) + g(y_p, -x_p, z_p) + g(-y_p, x_p, z_p) + g(-x_p, -y_p, z_p) \tag{2.21}$$

The change of sign in the variables is due to coordinate transformations required to account for the contributions of the other subsections, starting from the reference (blue) subsection.

2.3.2 Biot-Savart law applied for a cubic superconductor

From the Bean model, it is assumed that the applied magnetic field was high enough (at least $\mu_0 H_p$) to completely magnetise the superconductor. And so, a critical current density J_c is flowing in it. As in the case of the permanent magnet, the superconductor must also be divided into four subsections. However, Eq. 2.14 must be modified to use the critical current density J_c instead of the critical surface current density K_c. The Biot–Savart law then becomes:

$$\vec{B} = \frac{\mu_0}{4\pi} \int\int\int_V \frac{\vec{J_c} \times (\vec{x_p} - \vec{x_m})}{||\vec{x_p} - \vec{x_m}||^3} \, dv, \tag{2.22}$$

where the integration is no longer performed over the surface S but over the volume V. For a cubic superconductor of side l, the magnetic flux density components along x and z for a subsection are given by:

$$B_x^{\text{sub}}(x_p, y_p, z_p) = -\frac{J_c \mu_0}{4\pi} \int_{-\frac{l}{2}}^{\frac{l}{2}} \left[\left[\sinh \frac{y_p - y_m}{\sqrt{(x_p - x_m)^2 + (z_p - z_m)^2}} \right]_{-x_m}^{x_m} \right]_{-\frac{l}{2}}^{\frac{l}{2}} dx_m = f^*(x_p, y_p, z_p) \tag{2.23}$$

$$B_z^{\text{sub}}(x_p, y_p, z_p) = -\frac{J_c \mu_0}{4\pi} \int_{-\frac{l}{2}}^{\frac{l}{2}} \left[\left[\tan \frac{(y_p - y_m)(z_p - z_m)}{(x_p - x_m)\sqrt{(x_p - x_m)^2 + (y_p - y_m)^2 + (z_p - z_m)}} \right]_{-x_m}^{x_m} \right]_{-\frac{l}{2}}^{\frac{l}{2}} dx_m = g^*(x_p, y_p, z_p). \tag{2.24}$$

The main differences with Eq. 2.15 and Eq. 2.16 are that a third integral must be evaluated, and that the y-component now varies between $-x_m$ and x_m, and is therefore no longer constant. This model is so a semi-analytical model as the third integral is solved numerically. However, Eq. 2.19, Eq. 2.20, and Eq. 2.21 remain valid by replacing the functions f and g with f^* and g^* as explain in [21].

In order to model cracks, defects, or impurities where the critical current density does not flow in certain regions of the superconductor, it is necessary to compute the magnetic flux density for a superconductor with a parallelepiped shape, i.e., with different lengths along the x, y, and z directions, denoted respectively as l_x, l_y, and l_z. For example, if a geometry with $l_x < l_y$ is considered, Eq. 2.23 and Eq. 2.24 must be adapted. A schematic illustration of the top face of the superconductor is shown in Fig. 2.10. The red arrows represents the direction of the critical current density. In this configuration, the y-coordinate does not vary from $-x$ to x for all subsections. It only does so for the yellow and purple subsections. For the red and blue subsections, the y-integration limits vary from $-(l_y/2 - l_x/2 + x)$ to $(l_y/2 - l_x/2 + x)$. For all four subsections, the integration limits for x and z must be modified to $\pm l_x/2$ and $\pm l_z/2$, respectively.

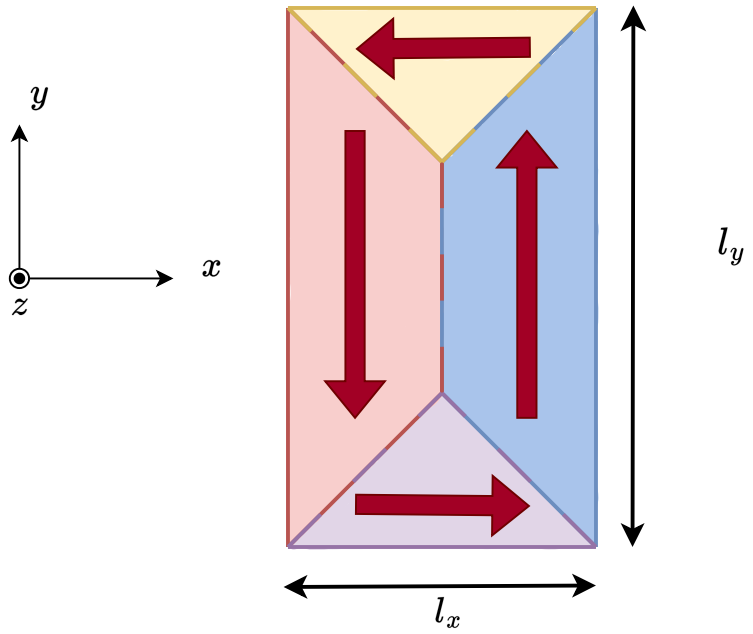

Figure 2.10: Schematic illustration of the top face of the superconductor where the red arrows represents the critical current density in the superconductor.

This approach makes it possible to model the fact that the critical current density flows in certain regions of the superconductor and not in others. The superconductor (that is, the actual object) will be modelled as an assembly of ideal superconductors with different geometries, in which the current flows only within these ideal superconducting regions. Some parts of the superconductor will thus be considered as carrying no current density. A more detailed explanation is provided in Sec. 3.2.

These defects might come from several elements such as cracks, impurities or even pores in the material. In [32], they studied the impacts of the pores on the critical current density. A photograph of one of their sample is shown in Fig. 2.11. They concluded that the pores have an influence on the critical current density and so on the trapped magnetic field. These impurities are modelled in this

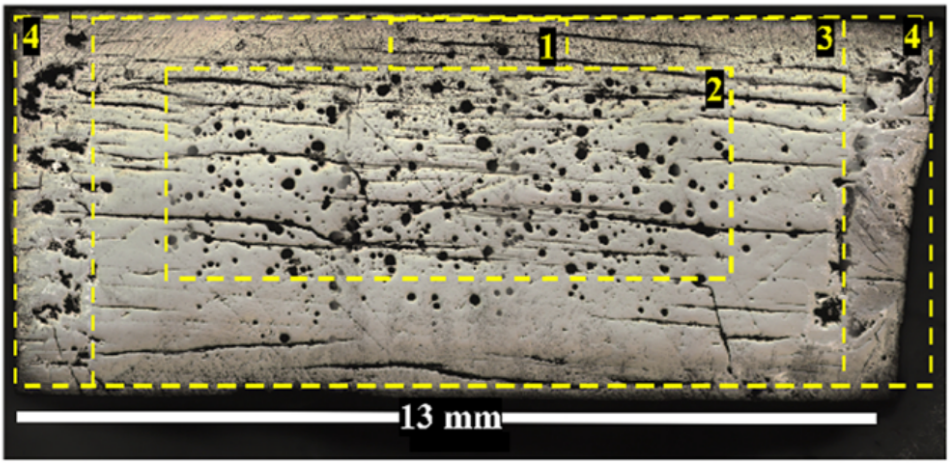

Figure 2.11: Photograph of the cross section of a superconductor from [32].

master's thesis as non-superconducting regions where no supercurrents flow. This results in a reduced effective size of certain parts of the sample, leading to different dimensions l_x, l_y , and l_z.

CHAPTER 3

Sample characterisation and modelling of defects

In order to assemble a Halbach array, the characteristics of the samples must be known. The first step is to determine the surface current density for the permanent magnets and the critical current density for the superconductors. The second step involves modelling the defects in the superconductors. Finally, a brief discussion is provided on the possible sources of error.

Unlike applications in which only one trapped-field superconductor is used, and for which the magnetic field of interest is close to the north and south pole faces, it is relevant to examine the lateral surfaces. For permanent magnets, they are assumed to be isotropic and unaffected by impurities, meaning their magnetic field follows the magnetic flux density profile given by Eq. 2.17. Therefore, the lateral surfaces of the permanent magnets are not studied, and the analytical model using surface current density is applied. For superconducting magnets, cracks may occur, damaging parts of the superconductor and creating regions where the critical current density cannot flow. The key difference between permanent magnets and bulk textured superconductors lies in the ceramic nature of the latter, which are composed of platelets. When subjected to mechanical shocks, cracks can form between these platelets, preventing the flow of the critical current density. In addition to mechanical damage, water and humidity can also degrade the superconductor through chemical reactions. Specifically, $YBa_2Cu_3O_7$ reacts with H_2O to form compounds that are not superconducting. As a result, the superconducting material deteriorates, reducing the amount of material available for current flow [33].

In this section, measurements are represented with solid lines, while models are shown with non-solid lines (dotted, dashed, dash-dot, etc.). The x, y, and z axes are oriented as in Fig 3.1 (a), which also shows the parameter d_m, representing the measurement distance, i.e., the distance between the top of the magnet and the measurement point. Moreover, instead of using N and S to denote the north and south poles of a magnet, an arrow is used to simplify the figures.

3.1 Permanent magnet

For the permanent magnet, which are Nd-Fe-B permanent magnets, the measurement is conducted at ambient temperature at a distance d_m from the top surface, as illustrated in Fig 3.1 (a). The red line indicates the path along which the measurement is performed, and point P is located at the centre of the magnet, at a distance d_m from the top. The dimensions of the cubic magnet are shown in Fig 3.1 (b). The cryogenic Hall probe used for the measurement is manufactured by AREPOC. It has an active area of 50 µm $\times$50 µm, and a distance of 150 µm between the probe surface and the active area. Fig 3.1 (c) shows a picture of the Hall probe and the sample in the sample holder.

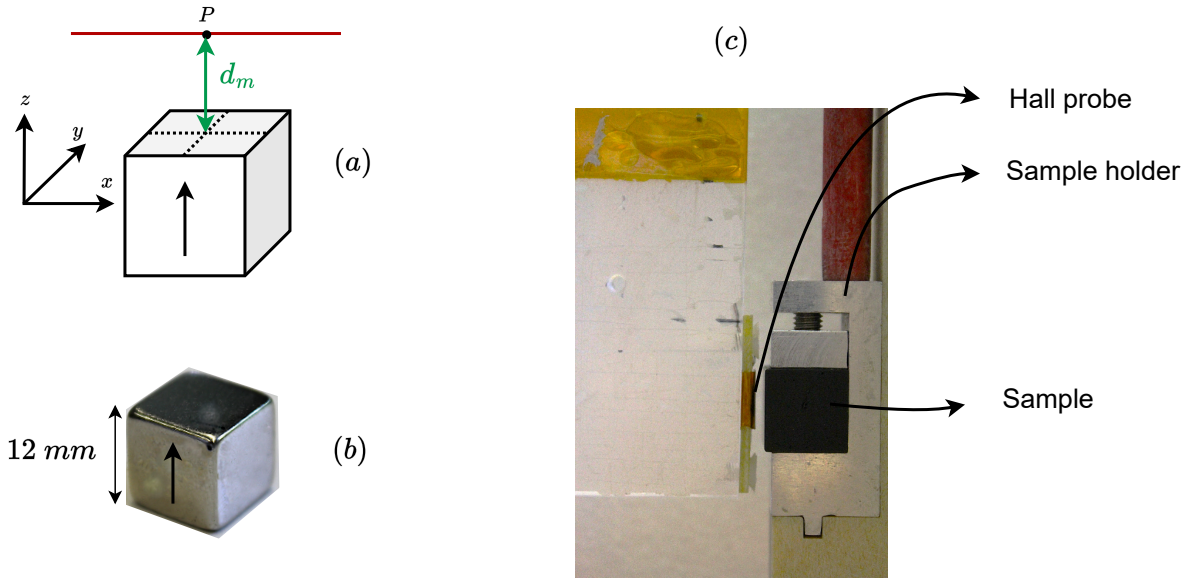

Figure 3.1: (a) Schematic illustration of the permanent magnet where d_m represents the measurement distance and P the point in the middle of the permanent magnet at a distance d_m. (b) Picture of a cubic permanent magnet with a size of 12 mm. (c) Photograph of the Hall probe, the sample holder and the sample.

In order to experimentally find the centre of the magnet, two measurements are performed, one along the x-axis and one along the y-axis, at a distance $d_m \approx 5$ mm from the surface, and a parabola is fitted to these points. The position of the maximum of the parabola provides an initial estimate of the coordinates of the centre of the sample. This method is valid because the permanent magnets are expected to be uniform and free of defects, so the maximum magnetic field is assumed to occur above the centre. A distance of 5 mm is chosen because, if the measurement is too close to the surface, the magnetic field profile becomes flattened. Conversely, if the measurement is carried out too far, the magnetic field becomes too small, making the fitting unreliable. Next, a measurement is carried out at a distance $d_m \approx 1.9$ mm to measure the flux distribution of the magnetic flux density (red line), which is then compared with the model given by Eq 2.18. From this measurement, the surface current density K_c is estimated by fitting the model to the data, as illustrated in Fig 3.2. This process is repeated for all available magnets in order to determine their respective K_c values. This parameter is important, as it is used in Sec. 4.1, where the magnetic field measurement is performed on a Halbach array. For the different permanent magnets (PMs), their respective flux density profiles can be fitted with a surface current density value K_c of 1.1 $\times 10^6$ A/m. The model shows good agreement with the experimental data, and the expected isotropy is observed.

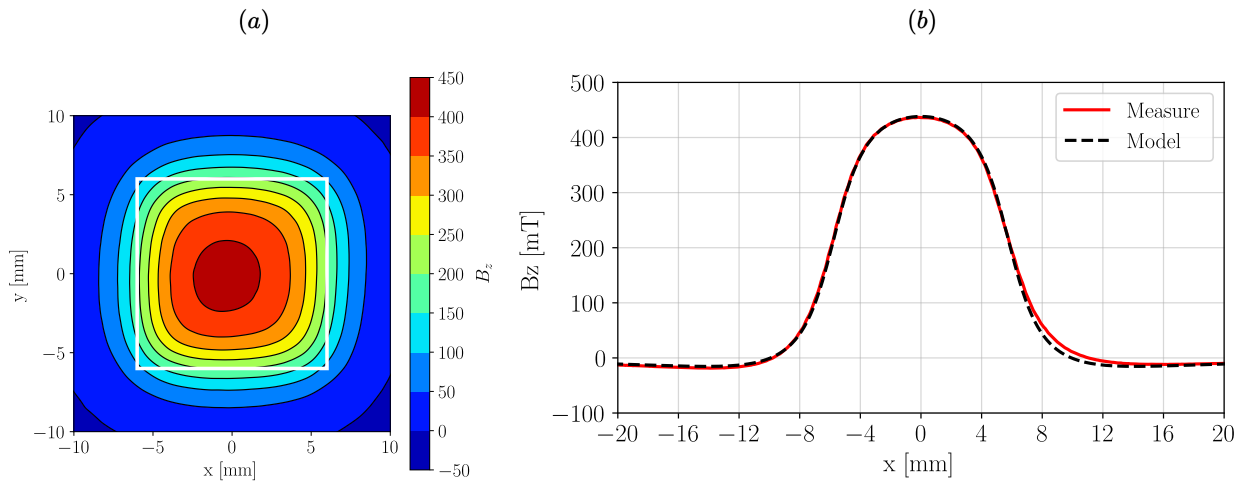

Figure 3.2: (a) Mapping of the magnetic flux density measured on a 12 mm side cubic Nd-Fe-B permanent magnet, in a pane located at 1.9 mm above the surface corresponding to the north pole of the magnet. (b) Measurement of B_z along x at a distance $d_m = 1.9$ mm for a permanent magnet (red line) and fitting of K_c with the model (black dashed line).

3.2 Superconductors

In order to obtain a magnet based on a superconductor, the sample must first be magnetised. The superconductors used in this master's thesis are commercial superconductor from ATZ company. To achieve this, the field cooling procedure is applied. The superconductor is initially at ambient temperature, placed inside an electromagnet and a magnetic field of 1.2 T is applied (corresponding to $\mu_0 H_{\max}$ in Fig. 2.7). The sample is then cooled down using liquid nitrogen (77K), transitioning into the superconducting state (below 92K). After a few minutes, ensuring the temperature has stabilised at 77K, the magnetic field is decreased at a rate of 1 mT/s. Fig. 3.4 (a) shows a picture of the electromagnet used, and Fig. 3.4 (b) presents a schematic of the electromagnet with the superconductor placed inside. Since superconductors may exhibit differing behaviours, the first step is to select which samples will be used to assemble a Halbach array. The objective is to obtain a large magnetic field at the surface of the array and the central sample plays a key role. Therefore, the central sample should generate the strongest field. A magnetic field mapping at $d_m \approx 2.5$ mm from the surface is performed on the six superconducting samples. These mappings are illustrated in Fig. B.1 in Appendix B. The maximum values are listed in Tab. 3.1.

Sample	I	II	III	IV	V	VI
$B_{\max}$ [mT]	247.8	298.2	363.5	292.3	280.6	211

Table 3.1: Table of the maximum magnetic field measure above the superconductors

Since sample III exhibits the highest magnetic field among the superconducting samples, it is selected as the central superconductor for the different Halbach arrays. Samples II and IV have maximum magnetic fields of the same order of magnitude and are therefore chosen to be placed to the left and right of the central one, respectively. As explained in Sec. 2.2.3, YBCO superconductors are composed of a–b planes along which the current density preferentially flows. They are therefore always magnetized with the field parallel to the c-axis and the trapped field is also directed mainly along the c-axis. The a-b planes can be identified via the face where the single crystal seed used to growth the bulk superconductor is visible. For sample III, now referred to as the "central" superconductor,

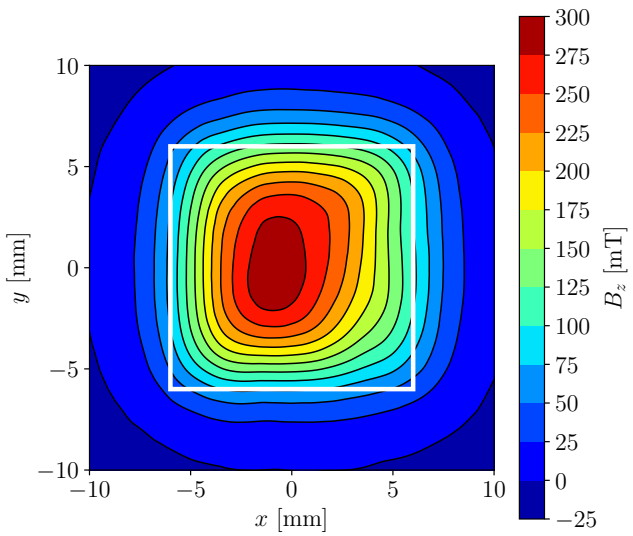

Figure 3.3: Mapping of B_z on the x-y plane at a distance $d_m = 2.5mm$ of the sample II of 13 mm side. The white square represents the position of the superconductor.

the face closest to the region of interest for the Halbach array is chosen to be the one with the seed. This is because the seeded face (referred to as the "top face" hereafter) is expected to contain fewer impurities than the opposite face (referred to as the "bottom face"). Samples II and IV are henceforth referred to as the "left" and "right" superconductors, respectively. For each of them, four faces could potentially be oriented toward the region of interest for the Halbach array. To choose the face, the x–y mappings are studied. The direction for which the gradient of B_z is the largest ($\partial B_z/\partial x$ or $\partial B_z/\partial y$) is chosen to face the region of interest. For example, Fig. 3.3 shows the distribution of magnetic flux density mapped 2.5 mm above of Sample II. The greatest gradient occurs in the negative x-direction, as the black lines are closer to each other. So this side of the superconductor is used for the assembly of the Halbach array. Finally, Samples I and V are used to complete the Halbach array composed of five superconductors. Sample VI is excluded due to its having the lowest maximum magnetic field.

As with the permanent magnets, a characterisation of the critical current density J_C must be performed. The same procedure is applied: the z-component of the magnetic field is measured along a line at a distance d_m from the surface of the superconductor. Additionally, since defects may be present on the faces, measurements along lines on the lateral surfaces are also carried out for the left and right superconductors.

Central superconductor

For the central superconductor, only the seeded face is measured. Fig. 3.5 shows the measurement performed at a distance $d_m = 2.5$ mm along the x-axis. The critical current density J_c obtained is 2.5×10^8 A/m^2.

Left superconductor

For the left superconductor, a measurement is carried out along the face used in the Halbach array, as shown in Fig. 3.6, and the model assuming a uniform J_c throughout the sample (called the ideal model, as it assumes an ideal superconductor without any defects) is applied. Eq. 2.23 is fitted to the data to determine J_c, leading to a value of $J_c = 2.5 \times 10^8$ A/m^2. The top face of the superconductor is placed to the right, while the bottom face points to the left. Even if the critical current density is the

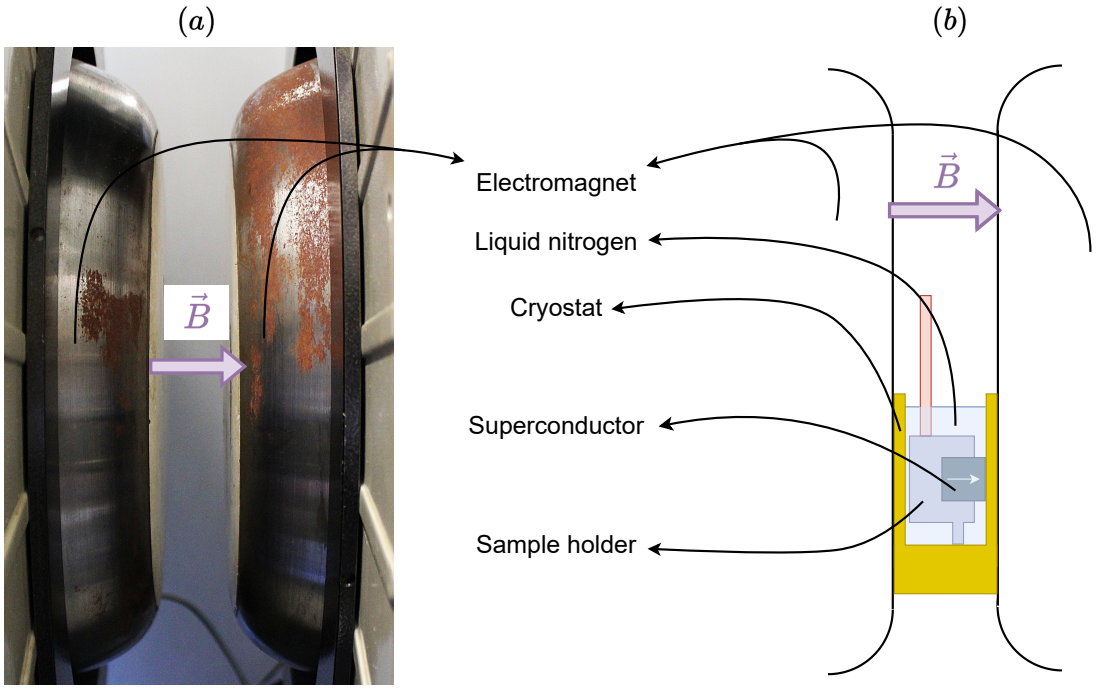

Figure 3.4: (a) Picture of the electromagnet used to magnetize the superconductors. (b) Schematic illustration of the cross section of the electromagnet during the magnetization procedure. The white arrow on the superconductor represents the orientation of the magnetization.

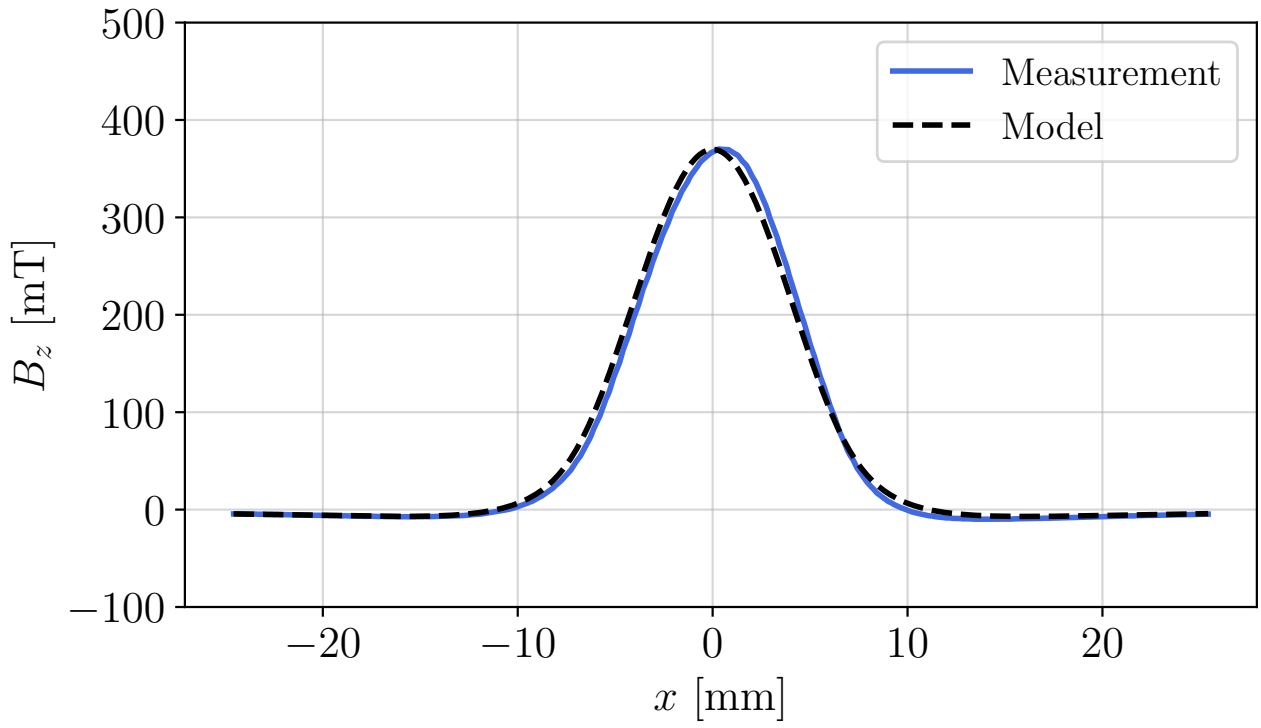

Figure 3.5: Measurement of the top face of the central superconductor of the z component of the magnetic field along the x axis at a distance d_m = 2.5 mm (blue line) and fitting of the critical current density of the model (dashed black line).

same as that of the central superconductor, several discrepancies can be observed between the model and the experimental data.

1. The point at which the magnetic field changes sign does not coincide: in the ideal model, the sign change occurs above the centre of the superconductor, whereas in the experimental data, it occurs at $x = 0.8$ mm to the left.
2. There appears to be a shoulder in the measured profile near $x = 0$. The presence of a shoulder in the flux density profile could displace the location of the zero crossing. This irregularity is likely due to defects in the superconductor.
3. The absolute values of the maximum and minimum magnetic fields are not equal. The measured maximum field is 132mT, while the minimum is –145mT. However, the model predicts symmetry between these values. This asymmetry likely indicates a defect near the top of the superconductor that affects the distribution of the flux density.
4. The positions of the maximum and minimum peaks differ between the model and the measurement. In the model, these peaks are farther apart than in the measurement. This may suggest that small regions near the top and bottom of the superconductor are not superconducting.

In order to model these various features, the ideal model must be modified. The chosen approach is to consider that the superconducting sample is composed of several superconductors of different sizes stacked on top of each other, while keeping the same critical current density for each of them.

The first two points, the shift in the sign change and the shoulder, can be modelled using three parameters, c, d, and e, which represent a crack in the superconductor. The parameter c describes the length of the cavity, d represents the distance of this cavity from the origin, and e is used to model the depth of the cavity. This cavity model is shown in Fig. 3.7 (a), where the impact of the different parameters is illustrated. Fig. 3.7 (b) shows how the flux density profile changes when varying the parameter e while keeping c and d constant. Changing the depth of the cavity yields three effects. First, the shoulder appears due to the presence of the cavity, creating an inflection point. Depending on the value of e, it may even generate a local maximum and minimum. For instance, when $e = 0.5$ mm, only an inflection point appears, whereas for $e = 2$ mm, both a local minimum and maximum are observed. Since no local extremum is visible in the measurement shown in Fig. 3.6, it suggests that the value of e should be close to 0.5 mm. Second, increasing e shifts the zero crossing to the left, as desired. Third, it introduces an asymmetry between the maximum and minimum values, also consistent with observations. In Fig. 3.7 (c), the parameter c is kept constant while the other two vary. The main effect of this parameter is that it creates a plateau in the flux density profile. The greater the value of c, the longer the plateau. The last parameter d is illustrated in Fig. 3.7 (d), where it allows to move the shoulder on the curve.

The third point, concerning the difference between the maximum and minimum values, is not resolved by the cavity alone. Therefore, an additional defect is introduced. This defect consists of a thin layer of thickness $e/2$, extending from the end of the first cavity to the top of the sample. Although the layer is small, it has a significant impact on the distribution of flux density predicted by the model, in a similar way as changing the distance d_m leads to a noticeable variation in the measurement, as explained in Sec. 3.3. The difference between the model with and without the $e/2$ layer is illustrated in Fig. 3.8. This new feature has two effects. As expected, it reduces the value of the maximum, which aligns with the experimental data. Moreover, it alters the impact of the shoulder in the model. This difference is particularly visible near $x = 0$, where the two models diverge significantly. However, adding the $e/2$ layer does not affect the distance between the two extrema.

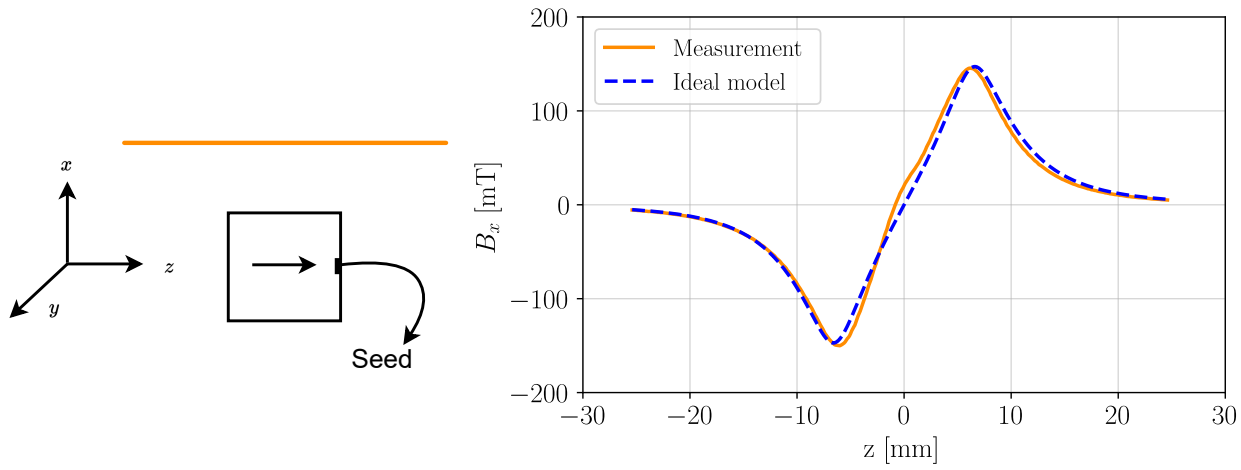

Figure 3.6: Measurement of B_x along the face used for the Halbach array (orange line) and comparison with the ideal model (dashed blue line)

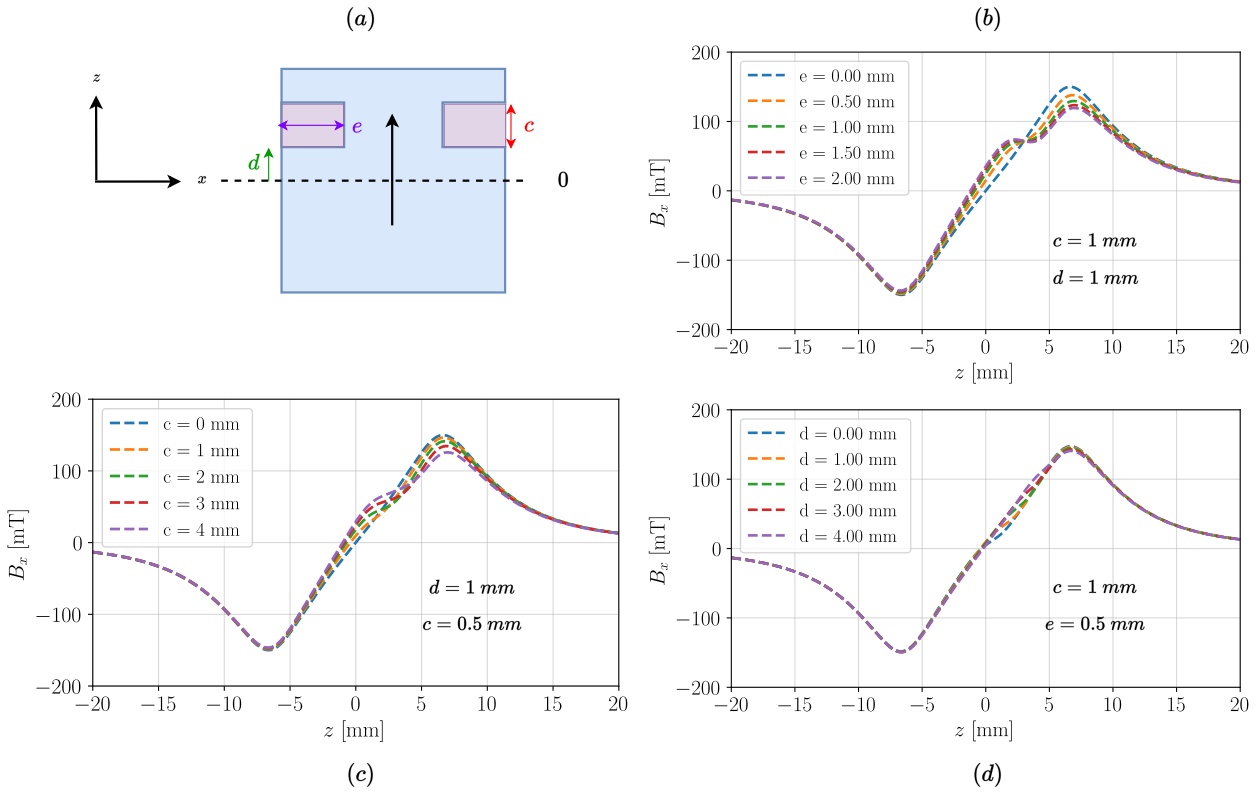

Figure 3.7: (a) Schematic illustration of the model with the different parameters, at a distance d_m = 1.5 mm. (b) numerical example of the model by varying e. (c) numerical example of the model by varying c. (d) numerical example of the model by
varying d

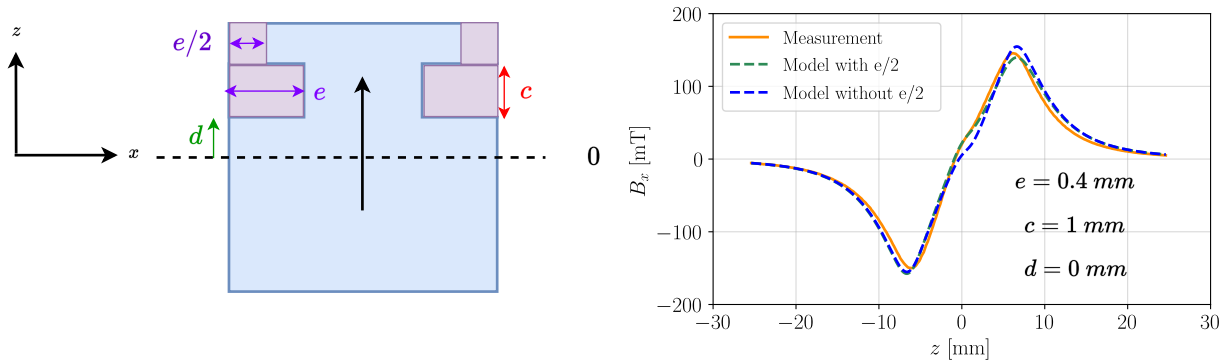

Figure 3.8: Schematic illustration of the model with $e/2$ and comparison of the model with and without $e/2$ with respect to the measurement

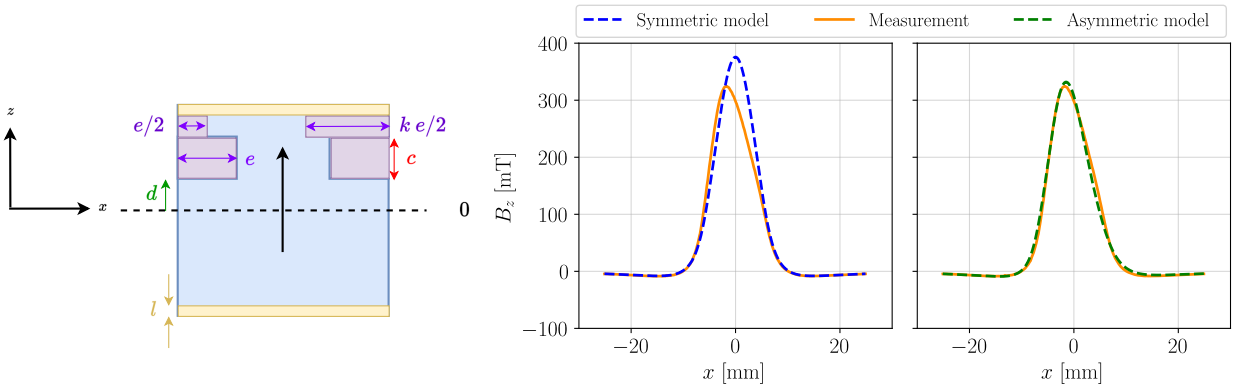

Figure 3.9: Model taking into account the asymmetry and comparison with the measurement at a distance d_m = 1.5 mm.

The last point, concerning the distance between the two extrema, can be modelled by introducing a small region of thickness l at both the top and bottom of the superconductor where no current density flows. This parameter allows for a reduction in the effective height of the superconductor, thereby decreasing the distance between the peaks. Since there is a discrepancy of approximately 0.5 mm between the peaks in the measurement and the model in Fig. 3.8, this gives an estimate for the value of l.

Up to now, all defects have been assumed to be symmetrical. To assess whether this assumption is realistic for the sample, a measurement above the top surface is carried out and compared to the symmetrical model. The measurement is shown in Fig. 3.9 (left). It can be observed that the profile above the top surface is not symmetric. To account for this, instead of considering a thickness $e/2$ on both sides (as illustrated in Fig. 3.8), a thickness of $e/2$ is used on the left and $k \times e/2$ on the right, where k is an additional fitting parameter. This new parameter allows the maximum value of B_z to shift to the left, introducing the desired asymmetry. Unlike with the permanent magnet, the maximum value is no longer considered to lie at the centre of the superconductor. The new centre is determined by calculating the mean between the two positions where the flux density changes sign. In Fig. 3.9 (right), the parameter is fitted with $k = 12$, which corresponds to an inactive layer of 2.4 mm on the right and 0.2 mm on the left. Moreover, the maximum value of B_z is seen to decrease when this model is considered. This can be explained by the fact that the model is a sum of ideal superconductors, each having its peak field at the centre. If the ideal superconductors are not aligned, their individual peaks do not coincide, so when summed, the resulting magnetic field is lower.

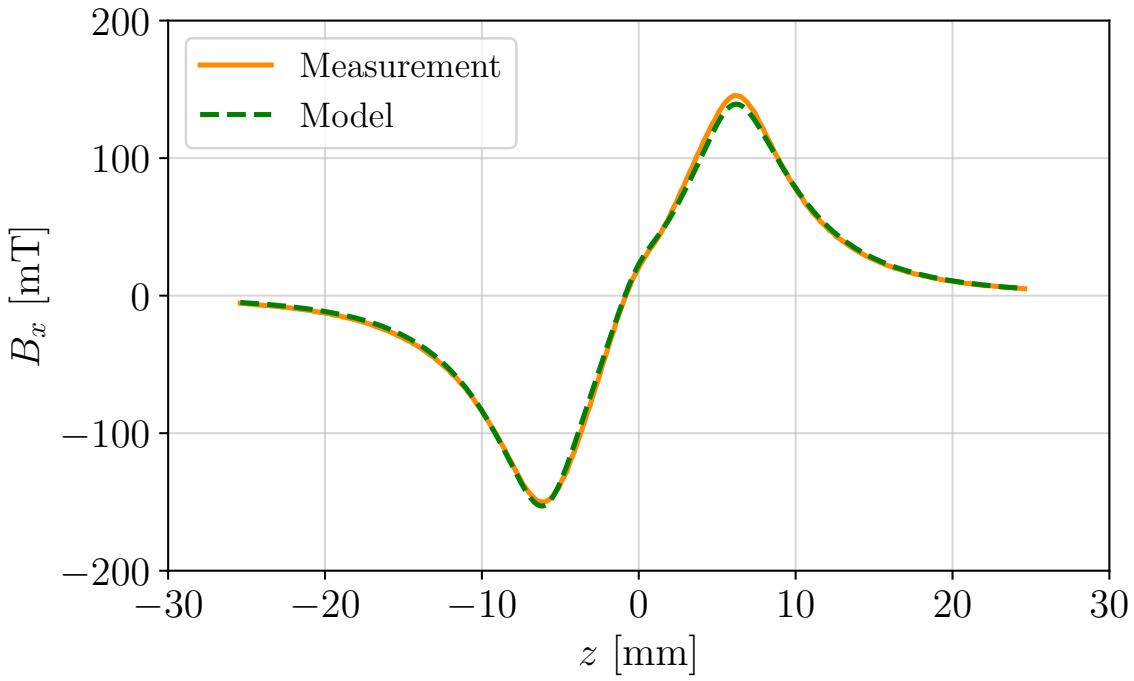

Figure 3.10: Measurement and model of the left superconductor at distance $d_m = 1.5$ mm with the different values of parameter given in Tab. 3.2.

By taking all the elements (c, d, e, l, and k) into account, it is possible to fit them in order to obtain a model that matches the measurement. The different lengths of the non-superconducting regions are summarised in Tab. 3.2. Except the defect located on the right (2.4 mm) it should be noticed that all defects are extremely small compared to the sample size (cube of 13 mm side), emphasizing the impact of tiny defects to the trapped field of a superconductor. One could naturally imagine other positions / extensions of defects or sources of non idealities (e.g. through a $J_c(B)$ dependence or a non-uniform $J_c(x, y, z)$ throughout the superconductor). This could lead to a difference between the measured trapped field profiles and the one expected for an ideal superconductivity with uniform J_c. The key points in the above analysis are that (a) the defects are assumed to be non superconducting zones oriented along the a-b planes of the bulk superconductor, which is consistent with cracks usually observable in their microstructure. (b) The effects need to be taken into account to model not only the flux distribution above the face perpendicular to the trapped flux density but also the flux distribution along one of the faces parallel to the trapped flux density. This is to model the flux density of the sample under investigation (here on the left part of the array) in a region that directly affects the flux density of the Halbach array. To verify the assumption of a constant critical current density in the various ideal superconductors used to construct this model, a final fit is performed for J_c, this time including the defects. It yields a value of $J_c = 2.5 \times 10^8$ A/m^2, identical to the value obtained when no defects were considered.

Parameters	c	d	e	l	$k \times e/2$
Length [mm]	1	0	0.4	0.5	2.4

Table 3.2: Table of the different length of the section that are not superconducting

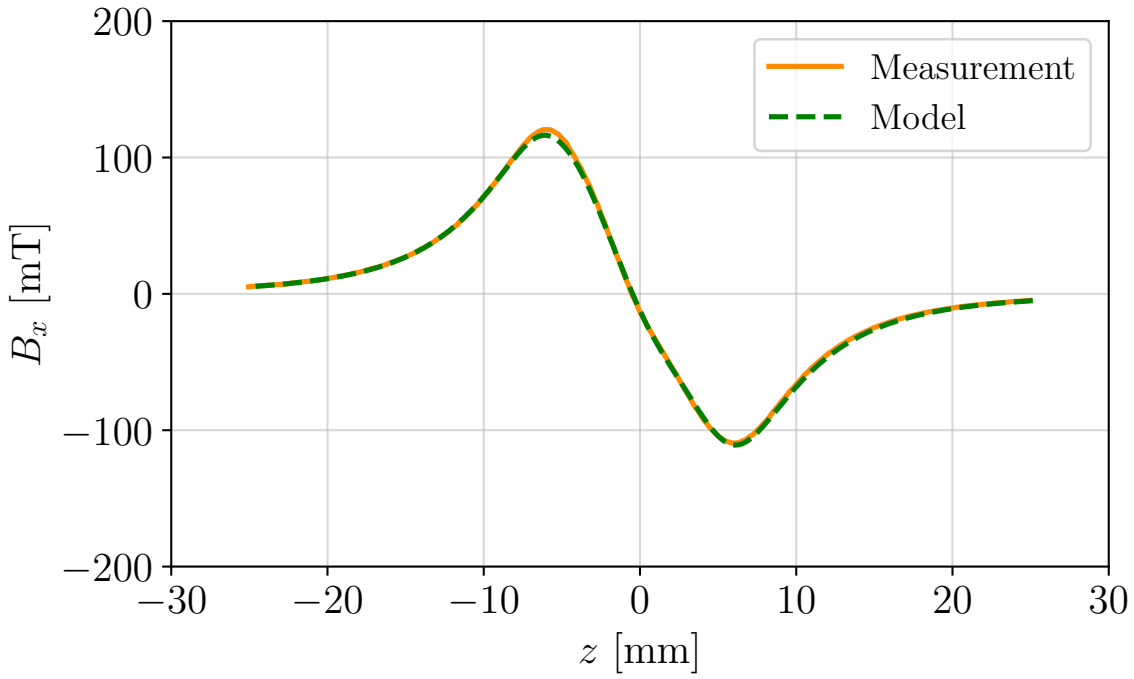

Figure 3.11: Measurement and model of the right superconductor with the c, d, e and l parameters. The measurement is done at a distance d_m = 2 mm.

Right superconductor

As for the left superconductor, a measurement along the face facing the region of interest for the Halbach array is carried out. Once again, an irregularities is measured and is model with the same ideas as the left sample. The results of the fitting is given in Fig. 3.11. Once again the critical current density is fitted to the measurement data and a value of 2.4 $\times 10^8$ A/m^2 is found.

An interesting observation is that the three superconductors have nearly the same critical current density J_c, yet the maximum values reported in Tab. 3.1 are different. This discrepancy can be explained by the fact that the measurement distance $d_m = 2.5$ mm in the table refers to the distance between the top surface of the superconductor and the Hall probe. For the left and right samples, however, it is assumed that a thin surface layer of the superconductor is not used. Even a small change in the measurement distance can significantly affect the magnetic field values obtained. This point is discussed in more detail in the next section, Sec. 3.3.

3.3 Source of errors

The measurement and the model are influenced by several sources of error. One major source is the distance between the sample and the Hall probe. To characterise this effect, a measurement is carried out along the z-axis up to the surface of the superconductor, as illustrated in Fig. 3.12. To estimate the associated error, the variation of B_z with respect to z is computed for different values of the distance d_m. By assuming linear behaviour in the vicinity of these points, it is possible to determine how the z-component of the magnetic field changes with the measuring distance. This distance may have a significant impact on the model and, consequently, on the fitted value of Jc. For instance, by taking an error on the distance of 0.2 mm, this leads to different relative error on the B_z measurement, these relative error are found by using the slope given in Tab. 3.3. The relative error are presented in Tab. 3.4. Moreover, Tab. 3.4 confirms that small defect in the superconductor can highly influence the

d_m [mm]	1	1.5	2	2.5
$\lvert dB_z/dz \rvert$ [mT/mm]	180	143	115	94

Table 3.3: Value of $\lvert dB_z/dz \rvert$ at different distance d_m.

d_m [mm]	1	1.5	2	2.5
Relative error [%]	7.4	6.9	6.4	6.1

Table 3.4: Value of the relative error for different distance d_m.

measurement. As the measurement is carried out close to the superconductor, the magnetic field B_z measured is higher and so the error. The increases of both the magnetic field and the error leads to say that the small defects in the superconductor are more noticeable as the measurement is carried out close to the surface.

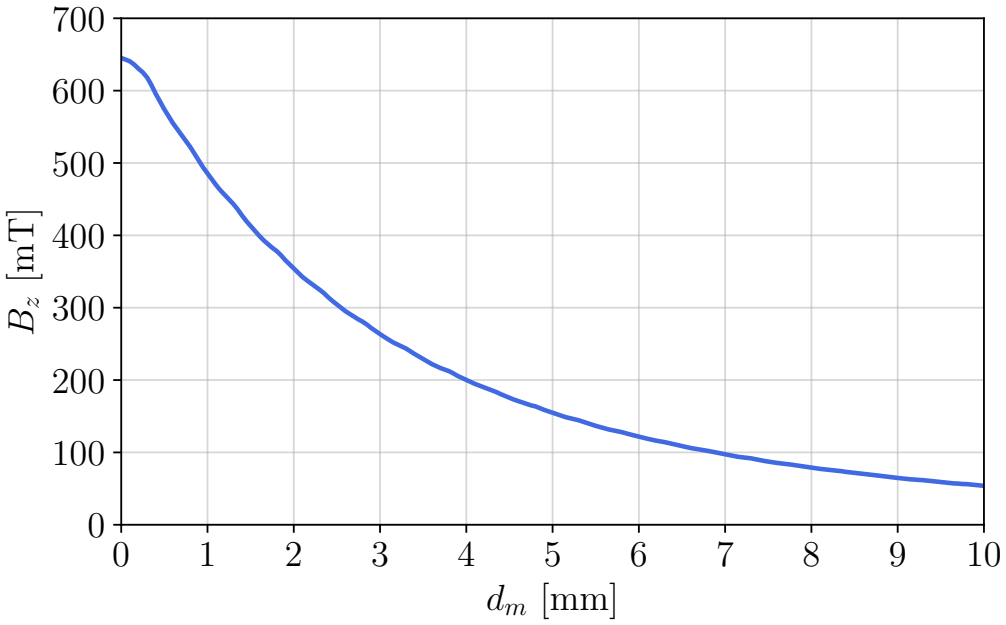

Figure 3.12: Measurement of B_z along d_m above the central superconductor.

Other sources of error may also occur, such as misalignment between the Hall probe and the sample. For example, if we consider an angle of $\alpha = 10°$, the relative error is given by $(1 - \cos\alpha)$, which leads to a relative error of approximately 1.5%. Another source of error can be flux creep: as the magnetic field decreases over time, the critical current density determined from one measurement may not be valid for another. Since measurements are not necessarily carried out at the same time, the magnetic field may be slightly lower than expected. For instance, consider the maximum magnetic field of Sample III from Tab. 3.1 (363 mT) as measured 45 minutes after magnetisation. Using Eq. 2.13 and assuming $n = 20$, it is possible to estimate the remaining trapped magnetic field after a certain time. After 10 minutes, the field is estimated to be 359 mT, corresponding to a relative error of about 1%.

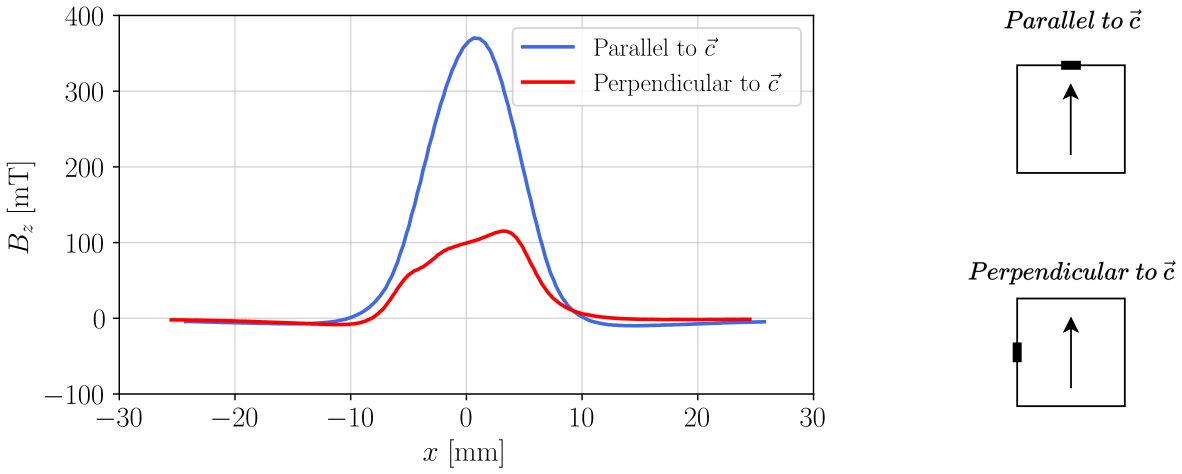

Figure 3.13: Measurement of B_z above the direction of magnetization when the magnetization is done perpendicularly to $\vec{c}$ and parallelly to $\vec{c}$ for the central superconductor. The black rectangle on the schematic on the right represents the seed of the superconductor.

The last source of error considered is related to the misalignment between the magnetic field and the c-axis during the magnetisation process. The worst-case scenario occurs when the sample is magnetised not along the c-axis but along the a or b-axis, i.e. perpendicularly to $\vec{c}$. To illustrate this, one sample is magnetised perpendicularly to $\vec{c}$ and compared to another magnetised parallel to $\vec{c}$, as shown in Fig. 3.13. The measured magnetic field is approximately three times lower for the perpendicular case, and the overall shapes of the profiles differ: the parallel case shows a fairly symmetrical curve, while the perpendicular one does not. This element is taken into account when considering demagnetization in the central superconductor as the demagnetization generates some current density in the planes perpendicular to $\vec{c}$. This illustration represents the worst-case situation, intended to highlight the impact of misalignment and emphasise the importance of proper orientation during magnetisation. In [34], the authors study how the maximum trapped field changes with the angle. They show that when the angle is less than 30°, the reduction in the maximum field remains below 4%.

Irrespective of the presence of possible cracks affecting the current flow parallel to the a-b planes, the reduced amplitude of the peak of the trapped flux profile when H is perpendicular to c remains observable. This reduction can also be explained by the anisotropy of the critical current density of the bulk superconductor. When the magnetic field is applied perpendicular to the c-axis, the current distribution is less favourable compared to the configuration where the field is parallel to the c-axis. For a field directed along the c-axis, as is the case for the magnetizing field applied to all bulk samples considered in this work, the supercurrents are induced in the a-b planes. This configuration corresponds to the critical current density that was determined experimentally in the previous experiments. When the magnetic field is directed along the a-b planes (perpendicular to c), the current loops, assumed to be parallel to the sample edges, are flowing partly along c and partly along a-b. If the critical current density is isotropic, the current loops induced in a square cross-section are also squared. In reality, the critical current density of bulk superconductors is anisotropic with $J_c||a\text{-}b > J_c||c$. The anisotropy ratio $J_c||a\text{-}b$ / $J_c||c$ determined experimentally on bulk superconductors at 77 K is typically close to 3 [35]. Fig. 3.14 shows the mapping of B_z in the x-y plane for magnetization along the c-axis (a), and for magnetization perpendicular to the c-axis (b). The colour bars are different in order to highlight more details in the mapping shown in (b). In (a), the mapping is symmetric and reaches a maximum value of 363 mT. In contrast, the mapping in (b) is asymmetric, and the location of the maximum value is shifted to the right compared to (a). This show a clear difference between the case when the

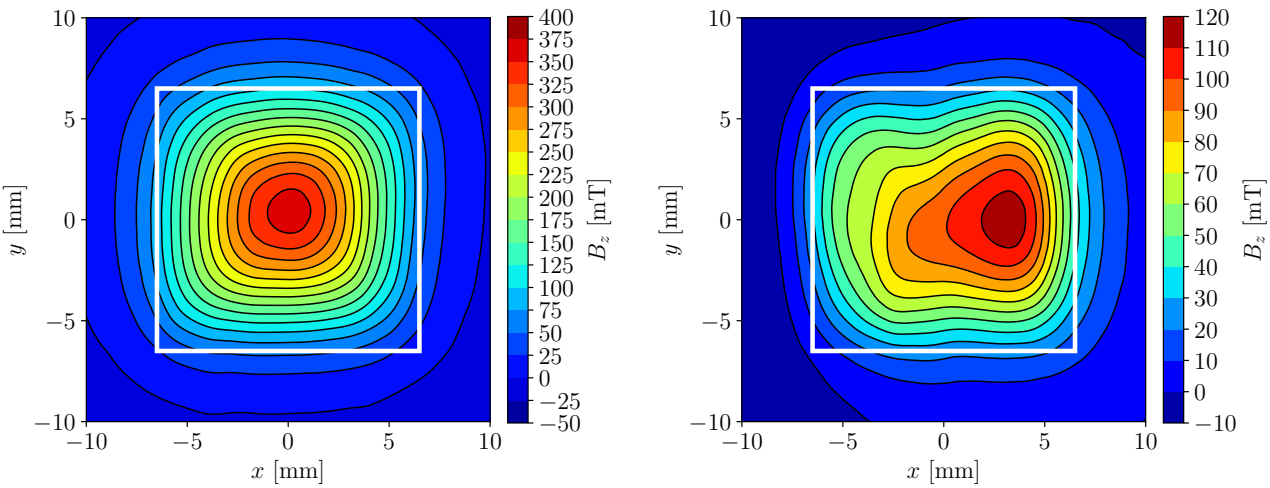

(a) Magnetization parallel to $\vec{c}$.

(b) Magnetization perpendicular to $\vec{c}$.

Figure 3.14: Mapping of B_z in the x-y plane for the central superconductor at distance d_m = 2.5 mm, when the sample is magnetised parallel to $\vec{c}$ and when it is magnetised perpendicular to $\vec{c}$.

current density is fully flowing in the a-b planes and when it only partially flows. The consequence is that current loops are rectangular and the sample magnetization and flux density depends on both $J_c||ab > J_c||c$. In such a configuration an anisotropic Bean model [36] should be used. However, the amplitude of the flux density generated in this configuration is expected to be mainly dictated by the smallest critical current of the two directions, i.e. $J_c||c$. In the present case the experimental ratio of the flux densities measured for the two field directions is about 3.1, in fair agreement with an expected anisotropy ratio $J_c||a$-b / $J_c||$c of ≈ 3. In the analysis of the Halbach array in the next chapter, it will be simply assumed that the current density associated with current loops induced by a field component parallel to a-b are squared are correspond to a critical current density $J_c||c$ which will be taken as (1/3) of the critical current density in the a-b plane.

CHAPTER 4

Linear Halbach array of three elements

The experimental set-up used to assemble the Halbach array is illustrated in Fig. 4.1. This set-up was created by M. Houbart for his PhD. It consists of five sample mounting frames on which the sample holders can be placed. These mounting frames can be moved towards the central one using lead screws driven by a DC motor. The approach speed is 1.25 mm/s. Several constraints were taken into account in the design of this set-up, including mechanical, magnetic, and cryogenic constraints, as detailed in his PhD thesis [21].

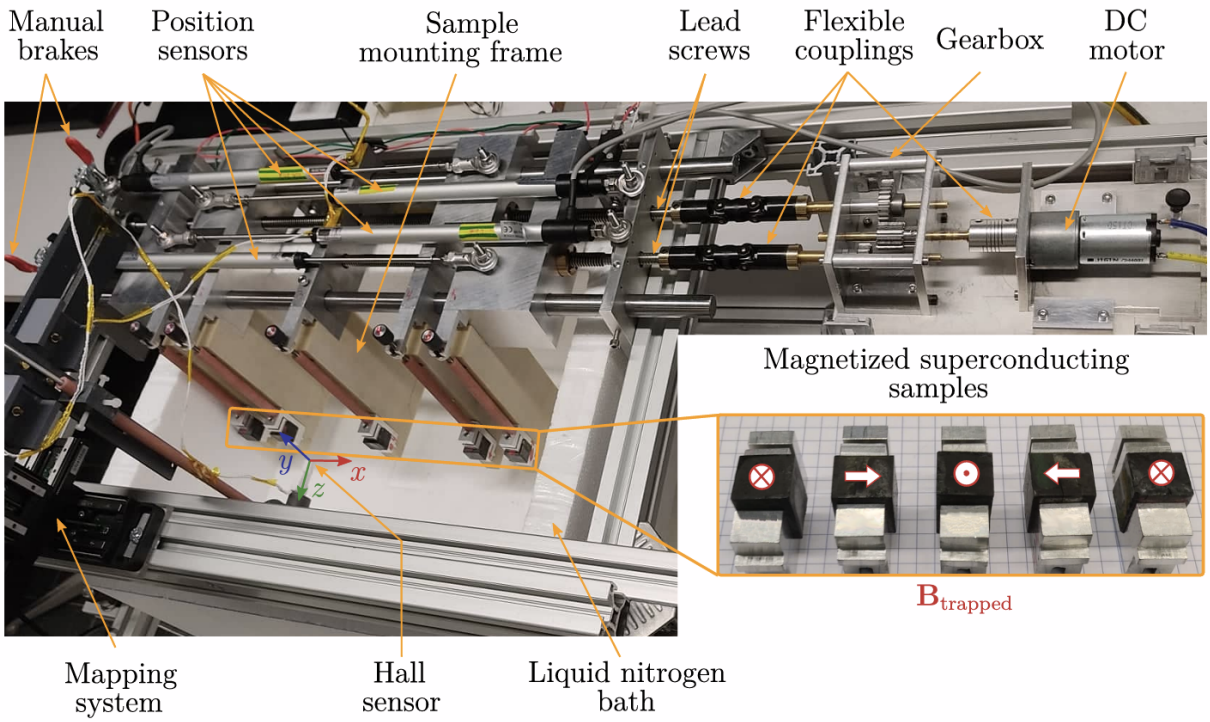

Figure 4.1: Photograph of the experimental set-up from [21].

In contrast to the previous chapter, where the x, y, and z axes were defined relative to a single sample, here, as more than one sample is used, the x, y, and z axes are defined relative to the central

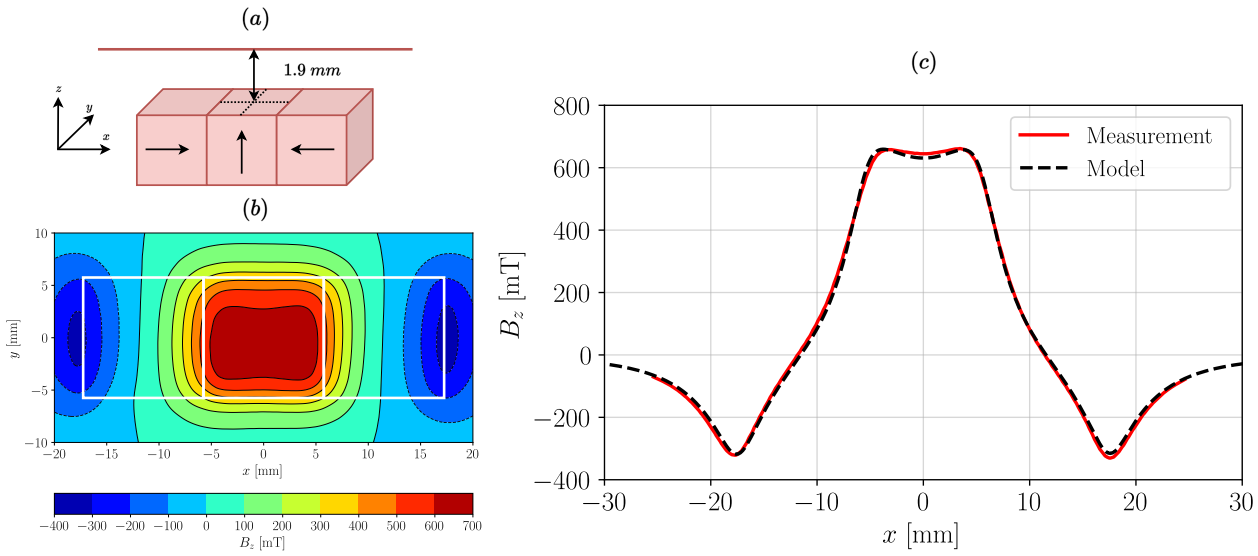

Figure 4.2: (a) Schematic illustration of the Halbach array made of permanent magnet with the new bases of axis. (b) Mapping of B_z in the x-y plane above the Halbach array. (c) Measurement of B_z along x at a distance $d_m = 1.9$ mm (red line) with a comparison with the model.

sample. This change affects the naming of the magnetic field measured along the lateral face of the sample and is important in Sec. 4.2. The new coordinate system is illustrated in Fig. 4.2 (a). In this chapter, measurements of the Halbach array made of permanent magnets are studied and compared with the model. Then, a Halbach array made of superconductors is investigated. As shown in [21], demagnetisation occurs during the assembly.

4.1 Permanent magnets

For the Halbach array made of permanent magnets, the measurement is carried out at room temperature and at a distance d_m of 1.9 mm, as shown in Fig. 4.2 (a). Fig. 4.2 (c) shows the measurement of B_z along the x-axis, along with a comparison to the numerical model. The model of the Halbach array corresponds to the sum of the individual magnetic flux densities, based on the surface current density described in Sec. 3.1. The model is in good agreement with the measurement, where the measurement is represented by a thick line and the model by a dashed line. This strong agreement indicates that the total magnetic field results from the simple addition of the fields from each permanent magnet, with no unexpected physical effects.

For applications, both the magnetic field and its gradient are important for generating high forces. It is therefore essential to examine the gradient. Since the analytical model is in good agreement with the measurements, the gradient can be computed numerically. The numerical results are shown in Fig. 4.3. Fig. 4.3 (a) and (b) show the norm of the magnetic field gradient for a single permanent magnet and for the Halbach array, respectively. Fig. 4.3 (c) presents a comparison of the gradient profiles for the single magnet and the assembled Halbach array at a distance d_m of 20 mm. From the two mappings, it can be observed that the region where the gradient exceeds 1 T/m (dark red colour) is more extended in space for the Halbach array than for the single permanent magnet. Moreover, the profile shows that the gradient of the Halbach array is nearly twice as large as that of the single magnet. Since both the magnetic field and its gradient are higher, this explains why Halbach arrays are of particular interest for applications requiring large forces.

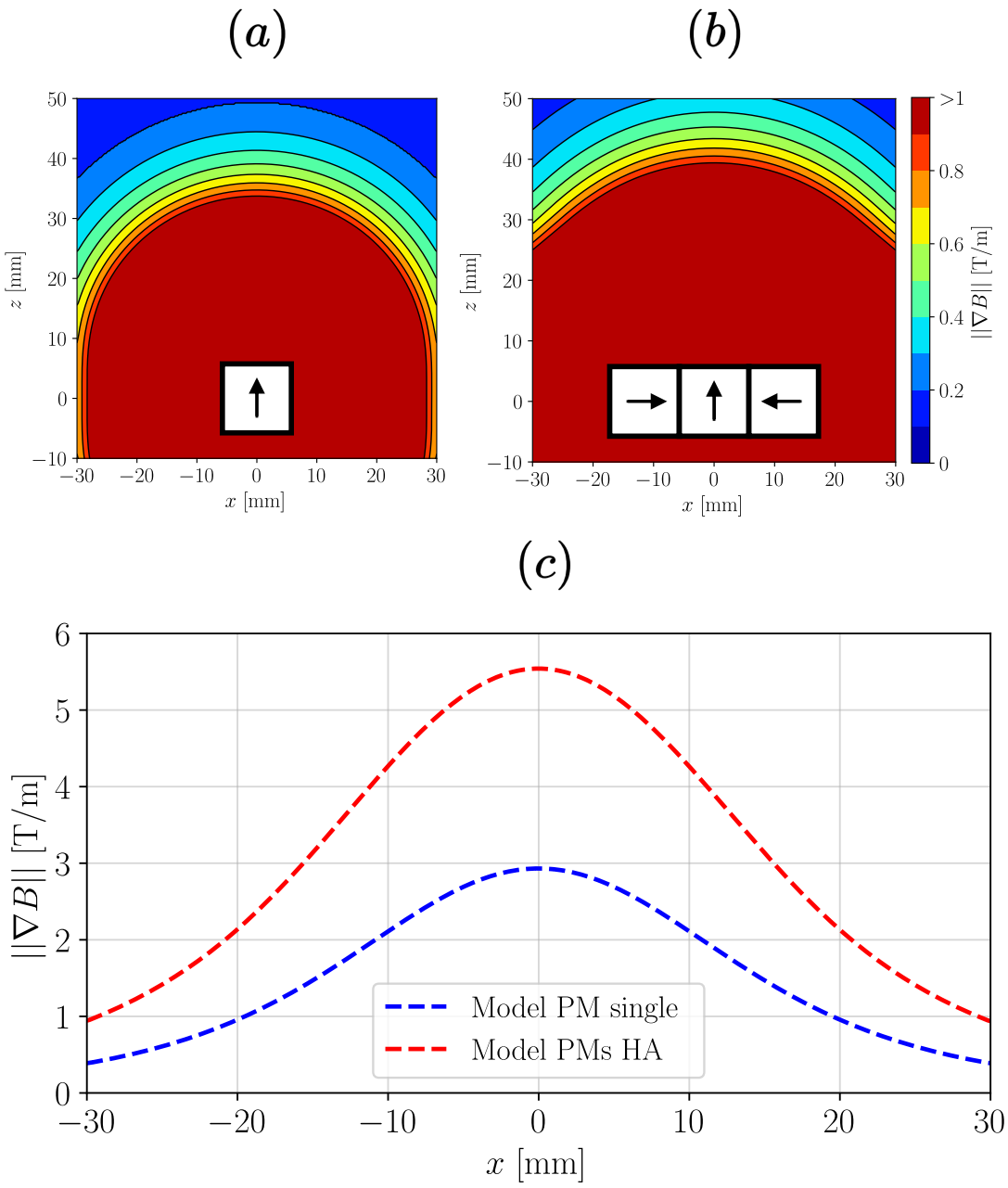

Figure 4.3: Magnetic gradient in the x-z plane for a single permanent magnet (a) and for an Halbach array of permanent magnets (b). Gradient at a distance $d_m = 20$ mm from the central permanent magnet along the x direction for a single permanent magnet and an Halbach array of permanent magnets (c).

4.2 Superconductors

Now, a superconducting Halbach array is assembled. To achieve this, the superconductors are positioned in their respective sample holders before the magnetisation process, to ensure that they are in contact. Then, they are magnetised one after another, as explained in Sec. 3.2. The critical current density of each sample is used in the model, along with the various parameters representing the defects. After assembly, since the magnetic flux density profile can be affected, a relaxation time of 45 minutes is observed before taking any measurements which are carried out at 77 K. Before the assembly, each sample is separated by a distance of at least 6 cm to avoid mutual influence.

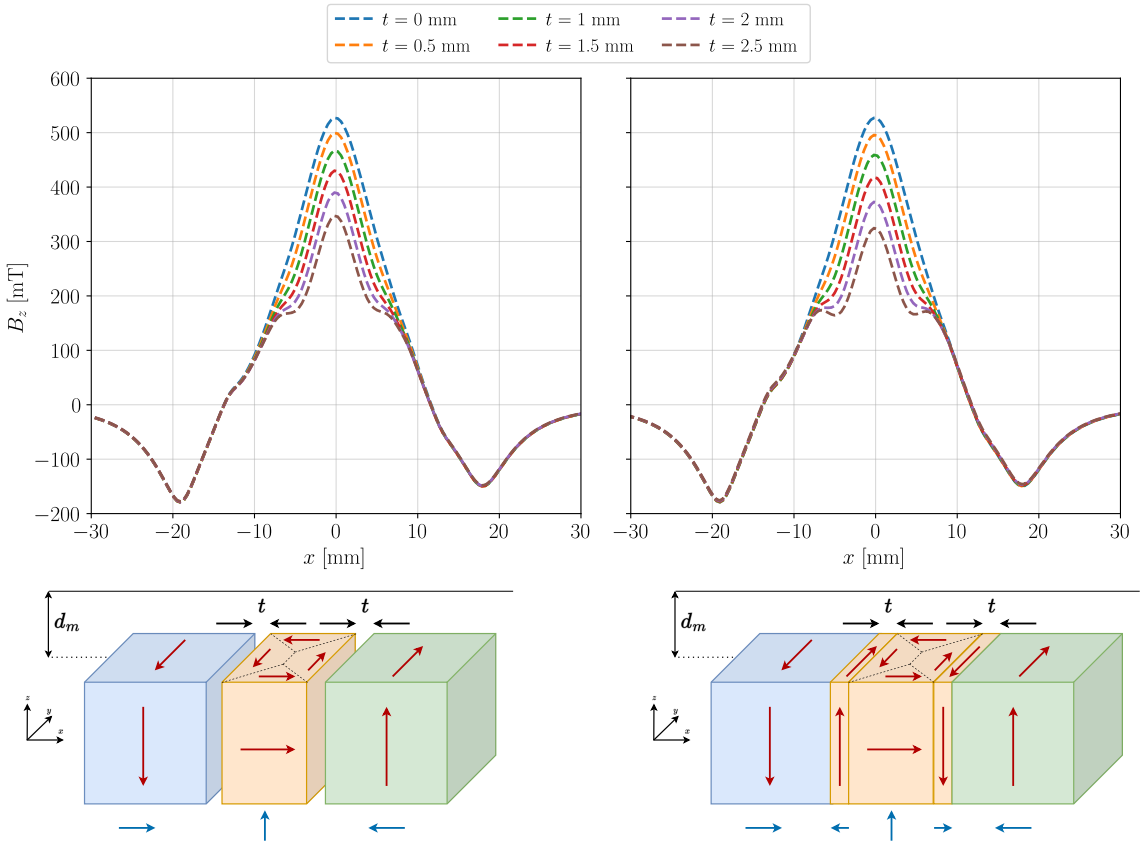

Figure 4.4: Model of the magnetic flux density B_z along x at 1 mm for the top for an Halbach array of superconductors. (left) without considering the counter flux, (right) considering the counter flux. For clarity of the schematic illustration, the size of the thickness t is shown bigger than the typical values expected (from 0 to 2.5 mm). The red arrows represents the current density flowing in each superconductor, the blue arrows below the sample represents the direction of magnetization. The colour on the superconductor are used to illustrate and delimite each superconductors.

When the superconductors are brought together to form a Halbach array, the two lateral ones generate a time-varying magnetic flux in the central superconductor. This time-varying flux induces a current density in the central superconductor. This induced current generates a magnetic flux density in the opposite direction to that produced by the lateral superconductors. This demagnetisation has two negative effects on the flux profile. First, it effectively ”reduces” the size of the central superconductor, meaning that the original magnetic field is also reduced. Second, the counter flux generated opposes the original flux. Towards the centre of the superconductor, the counter flux flows in the opposite direction to the original flux, thereby reducing the overall magnetic flux density. The induced current density flows in a plane that is not the a–b plane. As explained in Sec. 3.3, this results in a smaller generated magnetic field, approximately three times smaller than in the a–b plane. To account for this, the critical current density used for the central superconductor is divided by three in the regions affected by demagnetisation. In the model, this demagnetisation is assumed to be represented by two regions of thickness t. This parameter t is varied in Fig. 4.4. Fig. 4.4 (left) shows the magnetic flux density profile assuming that demagnetisation only reduces the effective size of the central superconductor, without generating a counter flux. Fig. 4.4 (right) shows the profile when the counter flux is also taken into account. In the left graph, the maximum magnetic field decreases as expected due to the smaller effective size of the central superconductor. In the right graph, the presence of the counter flux further decreases the magnetic field. For example, with a thickness t of 2.5 mm, the maximum field is 324 mT when the counter flux is taken into account, compared to 347 mT when it is not.

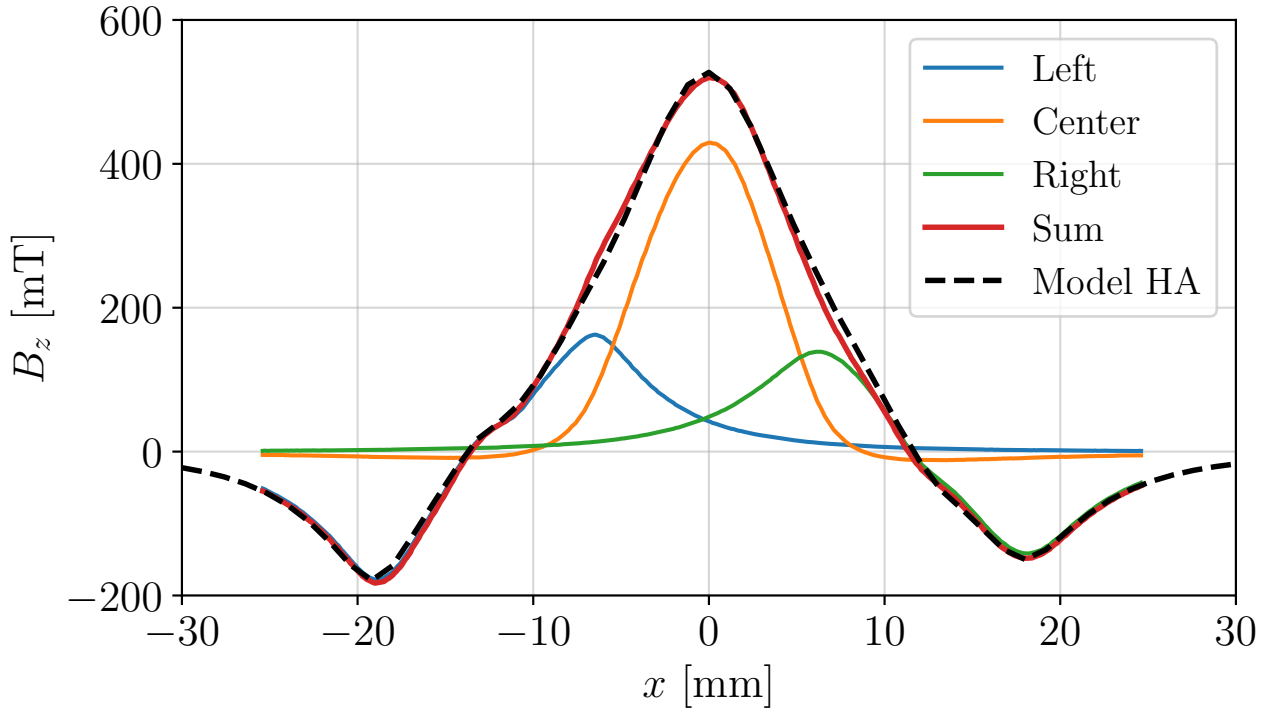

Figure 4.5: Measurement of each superconductor alone at a distance d_m = 1 mm (blue, orange and green lines). Sum of these measurements to have the magnetic flux density profile without demagnetization (red line) and comparison with the model without demagnetization (black dashed line).

In order to highlight the effect of demagnetisation, the samples are placed in their respective positions within the Halbach array, and the z component of the magnetic field is measured along the x-axis, one sample at a time. All the individual measurements are then summed to obtain the magnetic flux density profile that would be expected from a Halbach array without demagnetisation. This sum is then compared to the model. These measurements are shown in Fig. 4.5. It can be seen that the model assuming no demagnetisation matches the summed measurements quite well.

Once assembled, a relaxation time of 45 minutes is observed. To determine experimentally the parameter t used to account for demagnetisation, the maximum value of the model assuming a demagnetisation of the central sample is made to match the measured maximum of the Halbach array (HA) at a distance $d_m = 1$ mm. Fig. 4.6 shows the fitted model including demagnetisation (black dashed line), the measurement of the Halbach array (blue line), and the summed curve (light red) to illustrate the impact of demagnetisation. The thickness t found is 1.3 mm. One can see that the model fits the measurement quite well, except on the left side where a shoulder in the measurement shows a higher magnetic field than predicted by the model. By using parameters of the model that ensure that the modelled maximum flux density match the the experimental one, flux creep is not taken into account. The measurement of the Halbach array was carried out at least one and a half hour after the last sample was magnetised, due to individual measurements of each superconductor and the relaxation time after the assembly. As a result, the magnetic flux density trapped in each superconductor decreases over time. Thus, when measuring the magnetic flux density profile of the Halbach array, the total magnetic flux density is reduced due to the demagnetisation, as predicted by the model, but also by flux creep. By considering a value of 20 for the parameter n presents in Eq. 2.13, it is possible to estimate this decrease. The maximum value of B_z for the single central superconductor is 430 mT. With the equation, it leads to obtain a maximum magnetic field of 410 mT after one and a half hours. Consequently, the estimated thickness t may be slightly overestimated, leading to a stronger influence

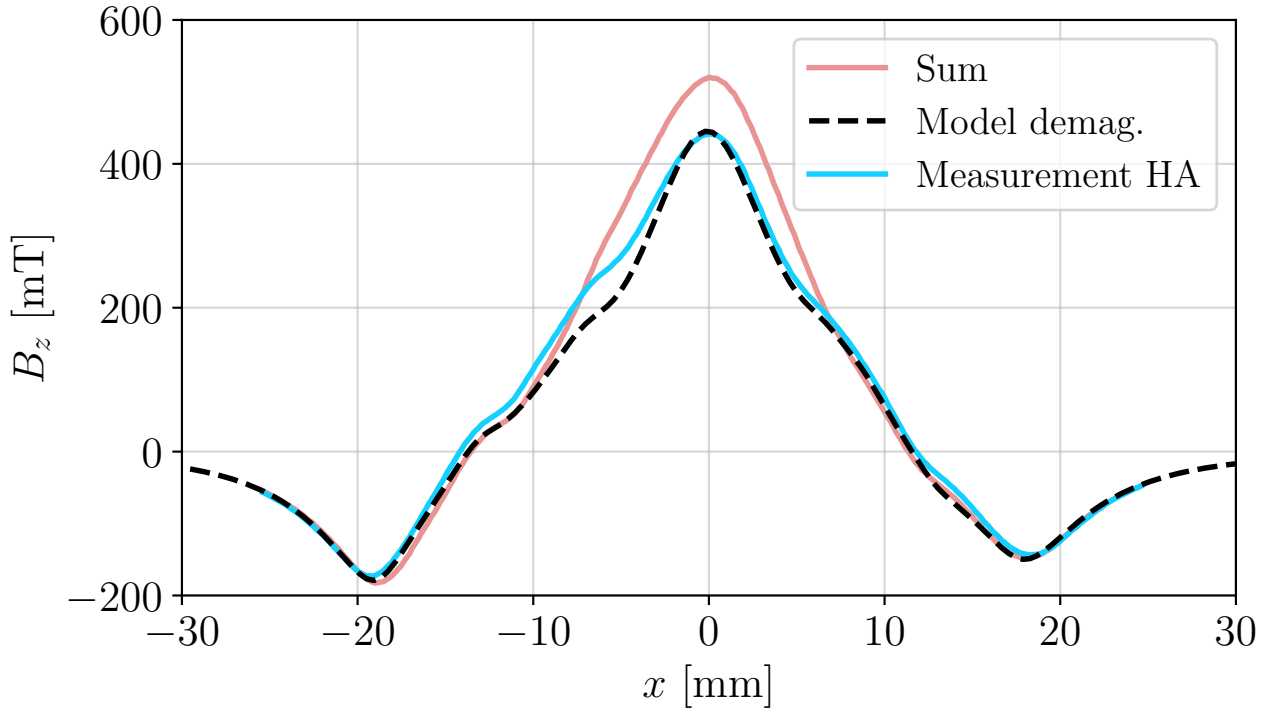

Figure 4.6: Magnetic flux density profile B_z along x of a superconducting Halbach array at a distance d_m = 1 mm. Sum of the single contribution of each superconductors (light red). Measurement of the assembled Halbach array (blue). Model considering a demagnetization in the central superconductor, with a thickness $t = 1.3$ mm (black dashed line).

on the modelled profile.

The model including demagnetisation is used to compute the magnetic field gradient. Fig. 4.7 (a) shows a map of the magnetic gradient in the x–z plane for a single central superconductor, while (b) shows the same for a Halbach array taking demagnetisation into account. Fig. 4.7 (c) presents the magnetic gradient along the x-axis at a distance $d_m = 20$ mm from the top of the central superconductor, for a single superconductor (black dashed line), a Halbach array with demagnetisation (green dashed line), and a Halbach array without demagnetisation (red dashed line). It can be observed that the magnetic gradient increases when using a Halbach array configuration compared to a single superconductor. However, this increase is smaller than expected due to the demagnetisation that occurs during the assembly process. This highlights the negative impact of demagnetisation.

In spite of this demagnetisation, the model reproducing at best the experimental results shows that the maximum gradient measured at 20 mm can reach 2.7 T/m , against 1.8 T/m for a single superconductor. Moreover, the zone where the gradient exceeds at given threshold (as an example, 1T/m) is 42 mm for the Halbach array, against 27 mm, i.e. an increase of 50 %. It should be also noted that the model considering the demagnetization and used to reproduce the experimental results takes into account the unavoidable defects (cracks) in the microstructure that were modelled in Sec. 3.2. Although a better performance would be expected if such cracks were not present, the experimental and modelling results shown in this chapter give evidence of increased performance of the Halbach array compared to a single superconductor, in spite of the defects affecting the current flow in the bulk superconductors.

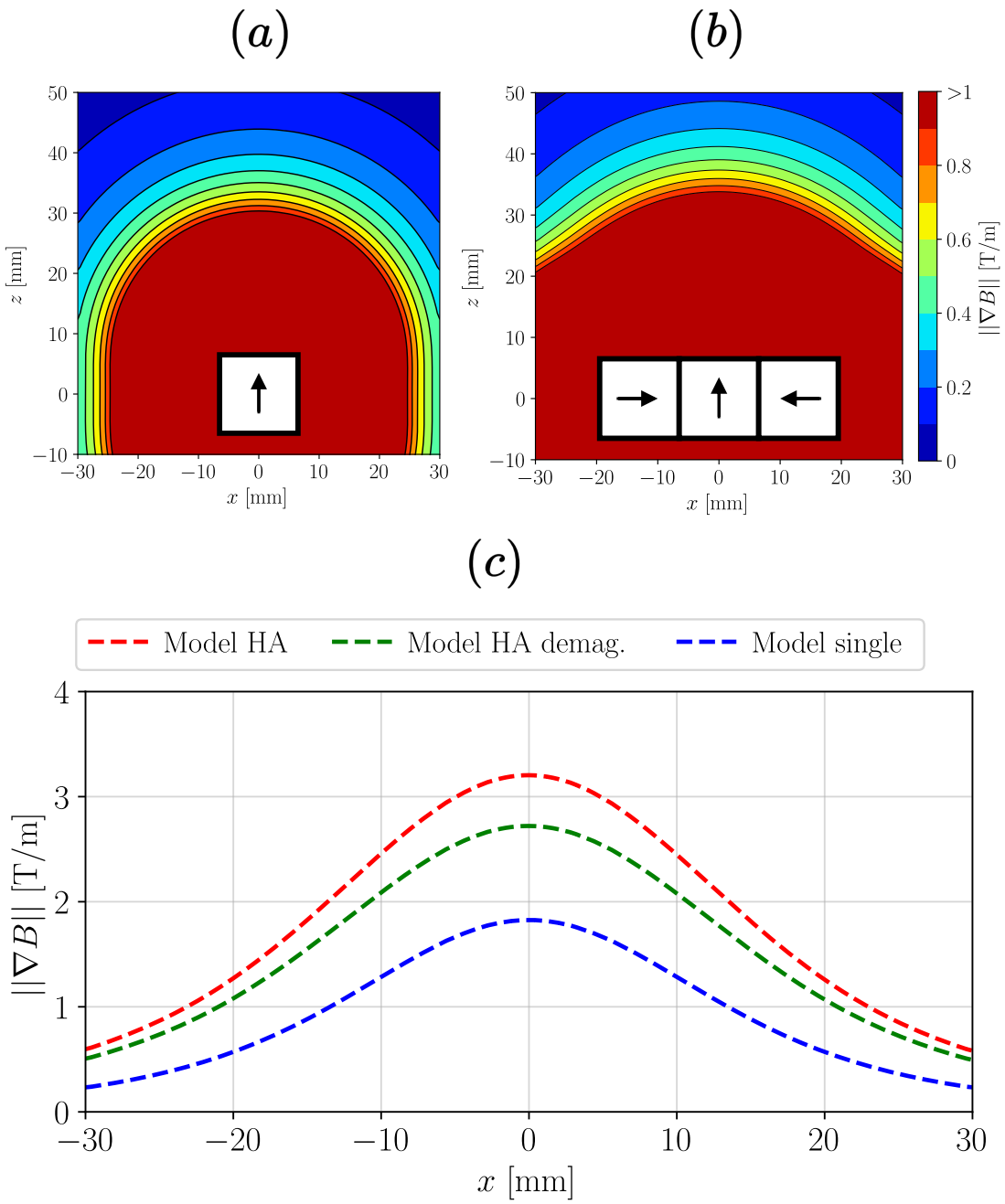

Figure 4.7: Magnetic gradient in the x-z plane for a single superconductor (a) and for an Halbach array of superconductors (b). Gradient at a distance d_m = 20 mm from the central superconductor along the x direction for a single superconductor and an Halbach array of superconductors (c).

CHAPTER 5

Halbach array with modified geometry

In this chapter, two new configurations of superconducting Halbach arrays are studied. The first, called the elevated Halbach array, consists of raising the two lateral superconductors. This configuration is expected to prevent demagnetisation in the central superconductor. The second, called the Halbach array with five superconductors, is a linear configuration in which two additional samples are placed at the extremities. In this case, a partial demagnetisation is expected to occur. These configurations were never investigated experimentally. Finally, a discussion is presented on the influence of sample size on both the magnetic flux density and the norm of the gradient.

5.1 Elevated Halbach arrays

The elevated Halbach array configuration was designed to reduce the demagnetisation observed in the standard three-element superconducting Halbach arrangement. To achieve this, two new sample holders were fabricated to vertically offset the lateral superconductors by 13 mm, the same as the side length of the central sample. This prevents direct alignment between the top faces of the lateral and central superconductors. Fig 5.1 shows the modified sample holder (left) compared to the previous sample holder and the assembled elevated configuration (right), where two distinct distances are introduced: d_m, the distance between the top face of the central sample and the measurement point, and d_l, the lateral distance from the side of a lateral superconductor to the same point. These distances are related by the equation $d_m = d_l + 13$ mm.

In the classical three-element superconducting Halbach array, demagnetisation occurs because the top faces of the lateral superconductors directly face the central one. This orientation exposes the central sample to a strong varying magnetic field when the lateral one are approaching, particularly at its lateral surface, leading to significant demagnetisation. In contrast, the elevated Halbach configuration prevents this direct interaction. The lateral superconductors are vertically offset, and their magnetic influence on the central superconductor is limited to the much weaker return flux. As this return flux generates a lower magnetic field variation, it does not induce notable demagnetisation. This mechanism also explains why demagnetisation only affects the central superconductor in the classical configuration. The lateral superconductors, which mainly experience the return flux from the central one, are subjected to much weaker magnetic variations and thus remain effectively magnetised. This

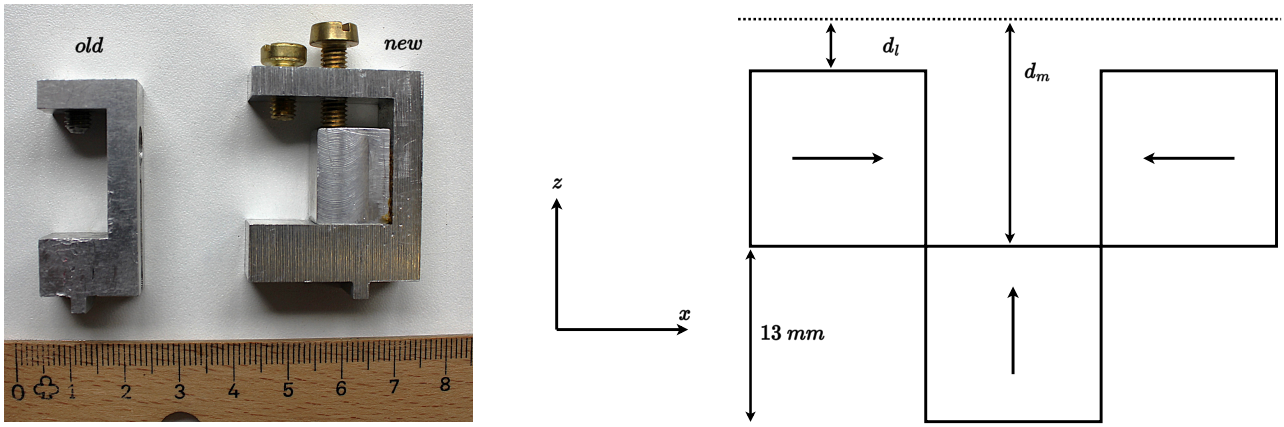

Figure 5.1: Photograph of the old and new sample holder (left). Schematic illustration of the configuration of the elevated Halbach array with the different distance d_m and d_l and the shift of 13 mm (right).

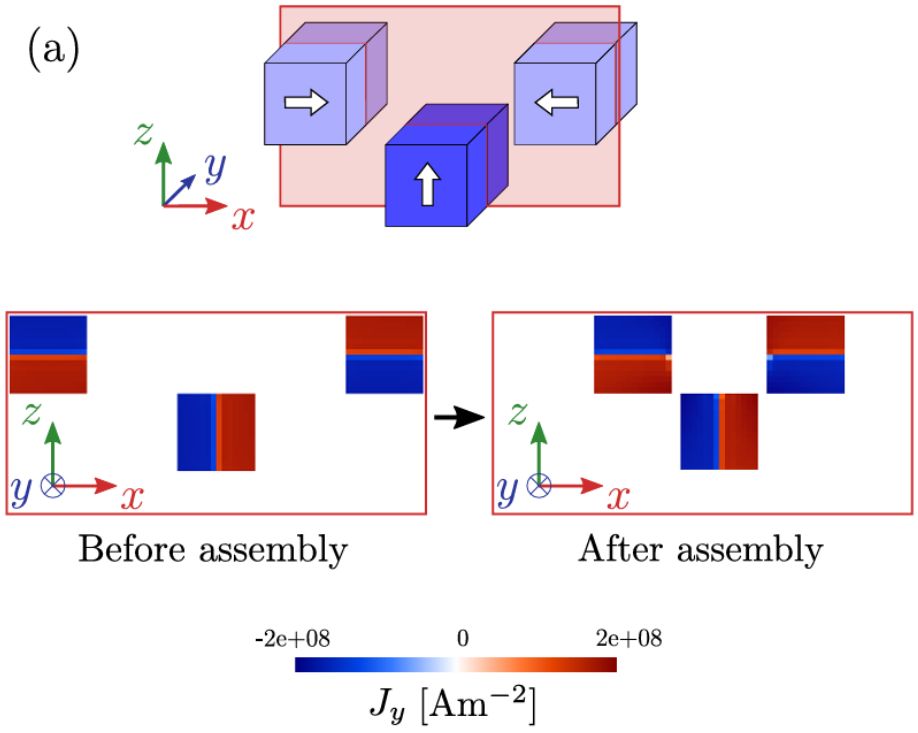

Figure 5.2: Results of the finite element method of the elevated Halbach array simulated from [21].

configuration was study numerically in [21] thanks to a finite element method simulation. The results of this simulation is shown in Fig. 5.2. The colour represents the distribution of J_c in the superconductors in the x-z plane. It is observed that there is not noticeable changes between the distribution of the critical current before and after the assembly. This confirms numerically that no demagnetization occurs for this configuration.

In order to experimentally verify that no demagnetisation occurs in the central superconductor, a measurement of B_z is carried out along the y-axis at a distance $d_m = 1.5$ mm. This measurement

line passes through the space between the two lateral samples and is illustrated in Fig. 5.4 (a). As in the previous section, the three samples are magnetised one after another, and the measurement is performed for each of them individually. Then, the sum of the three individual measurements is computed and compared to the measurement taken after assembling them into the elevated Halbach array. These results are shown in Fig. 5.4 (c). The measurements of the individual superconductors are shown by the blue, orange, and green lines. The sum of these individual measurements is represented by the red dotted line. Note that here the this dotted line does not represent the analytical model. The light blue line corresponds to the measurement of the elevated Halbach array. Fig. 5.4 (b) shows the mapping of B_z in the y–z plane, where the z-axis is represented by the parameter d_m. One can see that the sum of the individual measurements and the measurement of the elevated Halbach array almost perfectly match, confirming experimentally that no demagnetisation occurs in the central superconductor, as intended for this configuration.

An interesting observation from Fig. 5.4 is that the B_z value for the elevated Halbach array is lower than the magnetic field measured for the central superconductor alone. This is due to the two lateral superconductors, whose magnetic fields oppose that of the central one. This can be seen in the same graph, where the B_z vs y curves for the lateral samples are negative. Looking at the line where $y = 0$ mm in Fig. 5.4 (b), it can be observed that the z component of the magnetic field B_z decreases, then increases, and decreases again. The magnetic field transitions from a value between 50 and 100 mT (light blue), rises to a value between 100 and 150 mT (turquoise), and then returns to the 50–100 mT range. This variation is explained by the effect of the lateral superconductors: when close to the central one, their fields oppose the central field, reducing the total B_z. As the vertical distance increases, the lateral fields change direction and begin to align with the central field, increasing the total field. However, this increase does not fully compensate for the reduction caused by the increasing distance from the central superconductor.

To illustrate this phenomenon, an analytical model of an ideal superconductor is used, with a critical current density of $J_c = 2.5 \times 10^8$ A/m^2. In this model, no defects are included, to demonstrate that the observed behaviour is not caused by imperfections in the superconductor but is instead due to the geometrical configuration. Fig. 5.3 shows the B_z component along the z-axis, starting from the top surface of the central superconductor. For clarity, the range of the magnetic field is limited from –100 to 200 mT to better highlight the local maximum. Since the model assumes ideal superconductors, only one curve is used for the lateral sample, as both contribute symmetrically. However, both contributions are included in the curve for the Elevated Halbach Array. It is observed that the maximum value of B_z for the elevated Halbach array occurs around 12 mm above the surface, but this maximum remains lower than the magnetic field measured in the first 3 mm from the top surface.

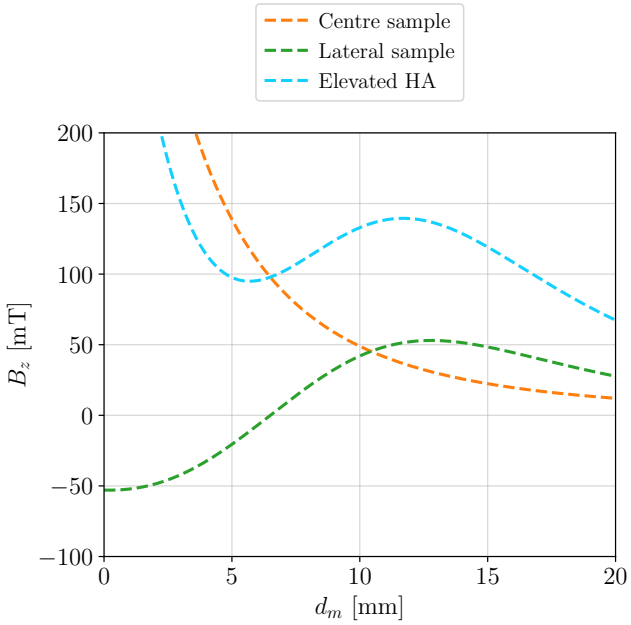

Figure 5.3: Model of the magnetic flux density B_z along x starting from the top of the central superconductor ($d_m = 0$ mm) for the central, one lateral sample and the elevated Halbach array (HA).

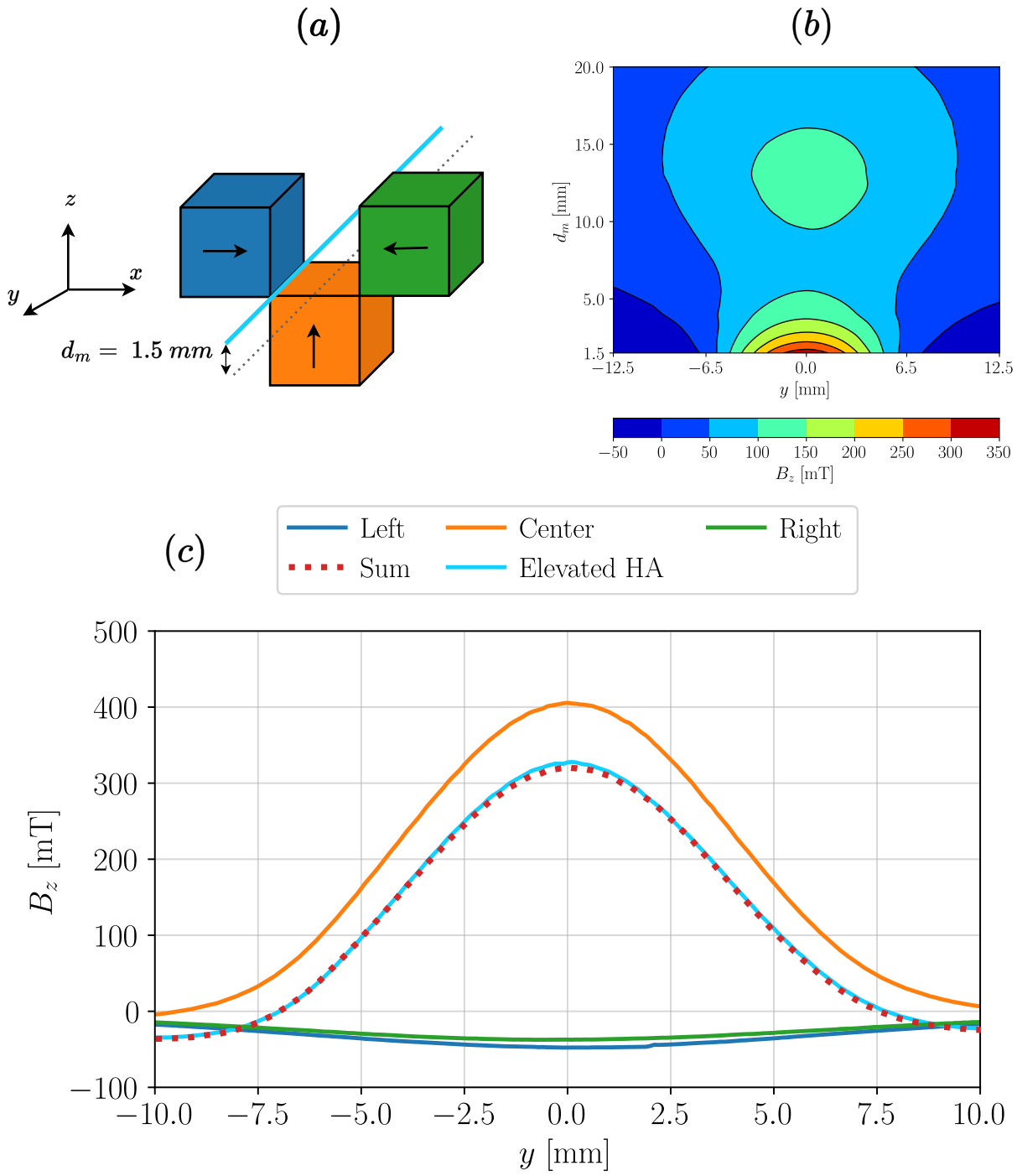

Figure 5.4: (a) Schematic illustration of the configuration where the colour corresponds to the colour of the single measurements. (b) Mapping of the magnetic field B_z in the y-z plane where the z axis is replaced with the distance d_m. (c) Measurement of each superconductor alone at a distance d_m = 1.5 mm (blue, orange and green lines). Sum of these measurements to have the magnetic flux density profile without demagnetization (red dotted line) and measurement of the elevated Halbach array (light blue line).

A second measurement of B_z is performed at a distance $d_l = 1.5$ mm (thus, $d_m = 14.5$ mm) along the x-axis, as illustrated in Fig. 5.5 (left). The measurement results are shown in Fig. 5.5 (right), where the measurement of the elevated Halbach array is represented by a light blue line, and the analytical model is shown as a dashed black line. One can observe that the model is in good agreement with the measurement. In comparison with the classical superconducting Halbach array, several differences can be highlighted. First, the overall shape of the two profiles differs. For the classical Halbach array, the profile exhibits a single peak, whereas for the elevated configuration, it has an "M" shape. This difference arises because, in the elevated configuration, the lateral superconductors contribute more significantly to the field, while in the classical configuration, the central superconductor dominates. Second, the maximum amplitude of B_z is lower in the elevated configuration than in the classical one. In the classical Halbach array, the maximum measured value was 432 mT, while for the elevated configuration, it is only 160 mT, approximately three times smaller. This can be explained by the fact that the central superconductor has the strongest influence on the magnetic flux density profile. In the elevated configuration, the measurement distance d_m is relatively large, so the contribution of the central sample to the measured magnetic field is quite small. To further illustrate the impact of the central superconductor in the elevated Halbach array, the analytical model is used to compute the magnetic flux density profile with and without the central superconductor. This comparison is shown in Fig. 5.6. The largest difference between the two curves occurs at $x = 0$ and is around 30 mT. This figure confirms that the peak in the classical configuration is due to the contribution of the central superconductor, while the "M" shape results from the lateral ones alone. It also demonstrates the relatively small influence of the central sample in the elevated configuration, as the maximum difference between the two profiles is only about 30 mT.

Regarding the gradient of flux density generated by the elevated Halbach array, the analytical model is used to compute the norm of the magnetic field gradient in the x–z plane for a single superconductor Fig. 5.7 (a) and for the elevated Halbach array configuration Fig. 5.7 (b). Additionally, the norm of the gradient is computed along the x-axis at a distance $d_l = 20$ mm (corresponding to $d_m = 33$ mm), as shown in Fig. 5.7 (c). This line corresponds to $z = 26.5$ mm in Fig. 5.7 (a) and $z = 39.5$ mm in Fig. 5.7 (b). In Fig. 5.7 (c), one can observe that the norm of the gradient is highest at $x = 0$ for the single superconductor at a distance $d_m = 20$ mm. This peak occurs within a region spanning from –5 mm to 5 mm, i.e. a 10 mm wide zone around the centre. However, the region where the gradient exceeds 1 T/m is broader for the elevated Halbach array than for the single superconductor. Specifically, this high-gradient region is approximately 36 mm wide for the elevated configuration, compared to about 27 mm for the single superconductor.

In comparison with the classical linear Halbach array made of three elements and measured at a distance of 20 mm above the array, the region above the 1 T/m threshold extends over 42 mm, approximately one and a half times larger than that of the elevated Halbach array. Moreover, the maximum norm of the gradient is 2.7 T/m for the classic Halbach array, compared to 1.8 T/m for the elevated one, nearly 66% as much. The main advantage of this new configuration is that it prevents the demagnetisation that occurs in the central superconductor in the linear Halbach array with three elements.

5.2 Halbach array with five superconductors

Up to this point, only three superconductors have been used. To create a Halbach array with five superconductors, two additional samples must be added. As mentioned in Sec. 3.2, samples I and V are used. More precisely, since sample V exhibits a higher maximum magnetic field (280.6 mT)

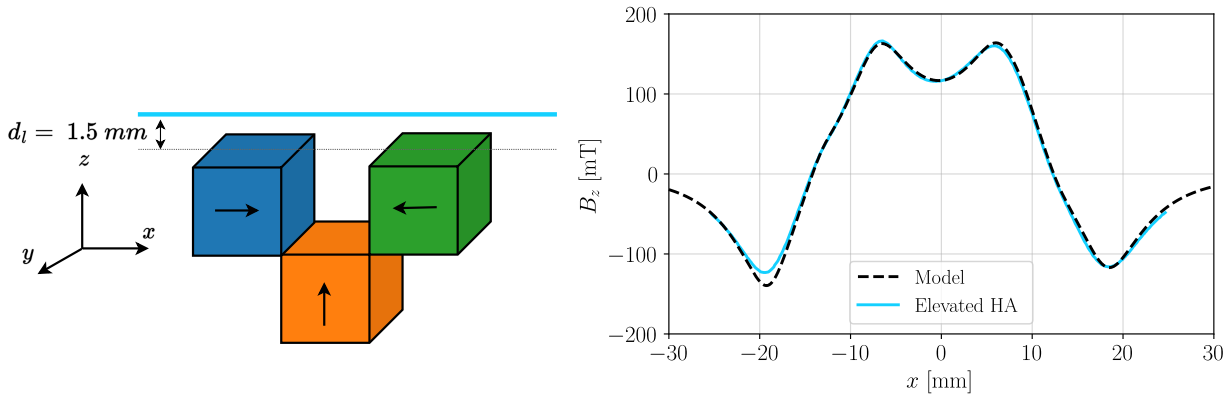

Figure 5.5: (left) Schematic illustration of the elevated Halbach array. (right) Measurement of B_z along the x axis of the elevated Halbach array at a distance d_l = 1.5 mm ($d_m = 14.5$ mm) in light blue line and comparison with the model black dashed line.

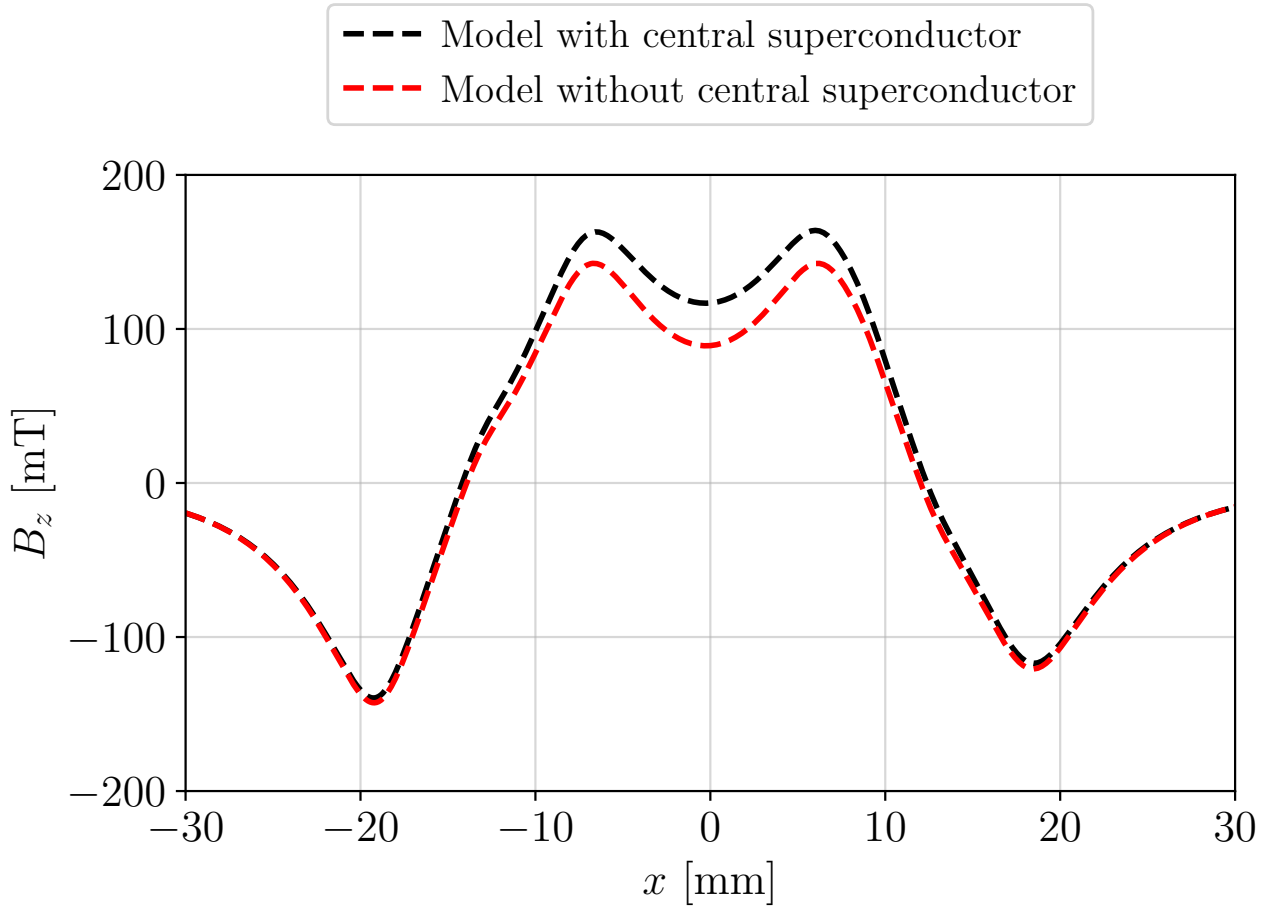

Figure 5.6: Comparison between the magnetic flux density profile with and without the central superconductor, respectively black and red dashed line, at a distance d_l = 1.5 mm ($d_m = 14.5$ mm).

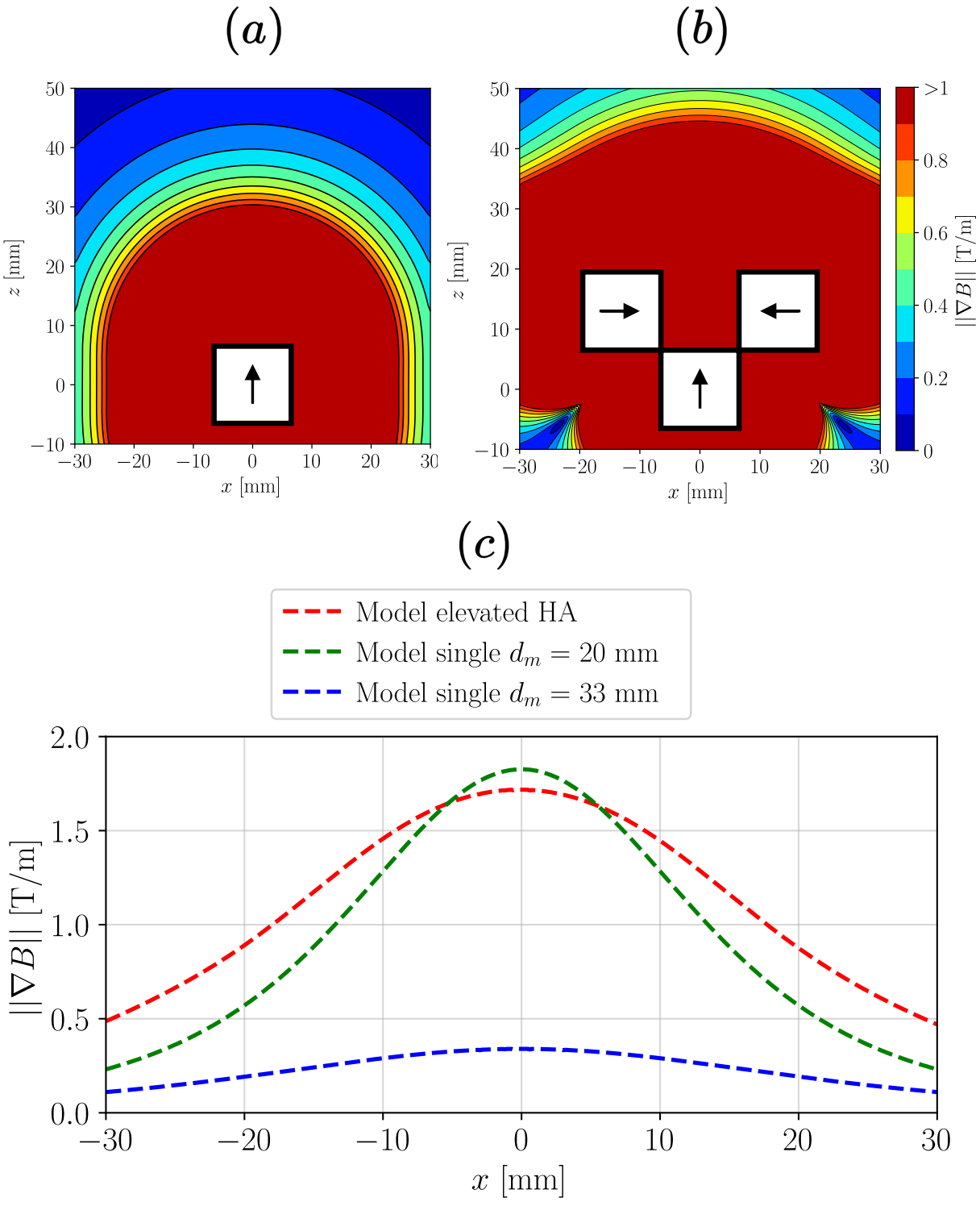

Figure 5.7: Magnetic gradient in the x-z plane for a single superconductor (a) and for an Halbach array of superconductors (b). Gradient norm at a distance d_l = 20 mm (d_m = 33 mm) along the x direction for a single superconductor and an elevated Halbach array of superconductors blue and red dashed line and comparison with a single superconductor at a distance d_m = 20 mm, green dashed line.

compared to sample I (247.8 mT), sample V is placed on the right side, where the existing right superconductor has a slightly lower magnetic field (292.3 mT) than the left one (298.2 mT). This arrangement is chosen to balance the magnetic field on both sides of the array. Since samples I and V have a lower maximum magnetic field than the others, defects are expected near the top of these superconductors. To model these defects, the key parameters used are l (representing a thin defective layer on the top surface of the superconductor) and the spacing $k \times e$. The critical current density is then fitted to the experimental data while accounting for these defects. For both samples, the fitted critical current density is $J_c = 2.4 \times 10^8$ A/m^2, with a defect layer thickness l of 0.7 mm for sample I and 0.6 mm for sample V. And a spacing $k \times e$ of 2.8 mm for sample I and 2.6 mm for sample II. A schematic illustration of the assemble is represented in Fig. 5.8

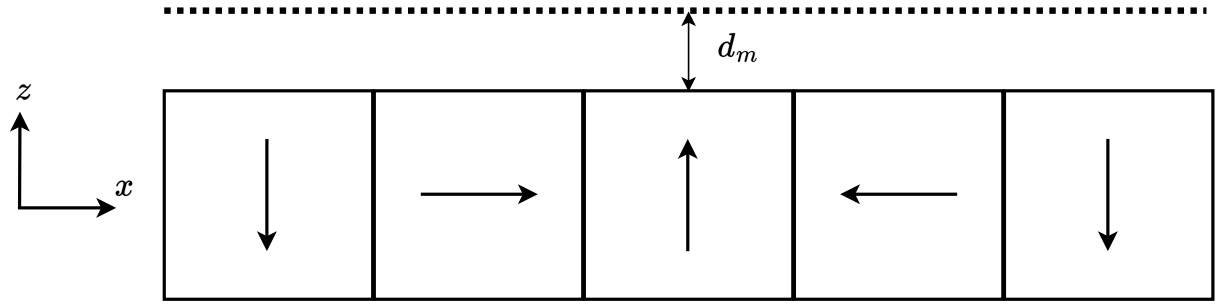

Figure 5.8: Schematic illustration of the Halbach array with five superconductors with the measurement distance of d_m = 1.5 mm. The arrows represent the direction of magnetization.

When assembling the Halbach array with five superconductors, demagnetisation is expected to occur in the central superconductor, as was observed in the three-element Halbach array. In addition, the two new end superconductors are also expected to experience demagnetisation. For the central superconductor, the demagnetised thickness t is kept at 1.3 mm, and this same value is used for the two end superconductors. This choice is justified by the fact that the magnetic fields coming from the top and bottom of the lateral superconductors are similar, and thus the time-varying fluxes at the ends are likely to generate counter-fluxes comparable to those affecting the central superconductor. Fig. 5.9 (a) shows the configuration of the five-element Halbach array with demagnetisation. The colours represent each superconductor, along with their demagnetised regions, where applicable. Since the 3-axis system used to move the Hall probe has a maximum range of 5 cm, and the configuration spans 6.5 cm, two separate measurements were performed: one on the left part of the configuration and one on the right. Because the 3-axis system had to be repositioned during the process, the two measurements are presented separately. Fig. 5.9 (c) shows the two measurements, along with the model including demagnetisation as illustrated in (a). Fig. 5.9 (b) displays a mapping of B_z in the x–y plane, where black contour lines represent 50 mT steps, and colour gradients correspond to 100 mT steps. In Fig. 5.9, one can observe that the model is in reasonably good agreement with the experimental data. On both sides, near the negative peaks, a shoulder appears, an effect attributed to demagnetisation, similar to what was shown in Fig. 4.6, and which was not present in the classical three-element Halbach array.

The magnetic field gradient is illustrated in Fig. 5.10. Figs. 5.10 (a) and (b) show the norm of the magnetic gradient in the x–z plane for a single superconductor and for the Halbach array with five elements, respectively. Fig. 5.10 (c) presents the norm of the magnetic gradient along the x-axis at a distance $d_m = 20$ mm, comparing the five-superconductor Halbach array (with and without demagnetisation) and a single superconductor. First, it can be observed that the region where the gradient exceeds 1 T/m extends over 78 mm. Compared to the configuration with three samples, where this region was 42 mm long, the five-element array nearly doubles the effective range. Moreover, the shape

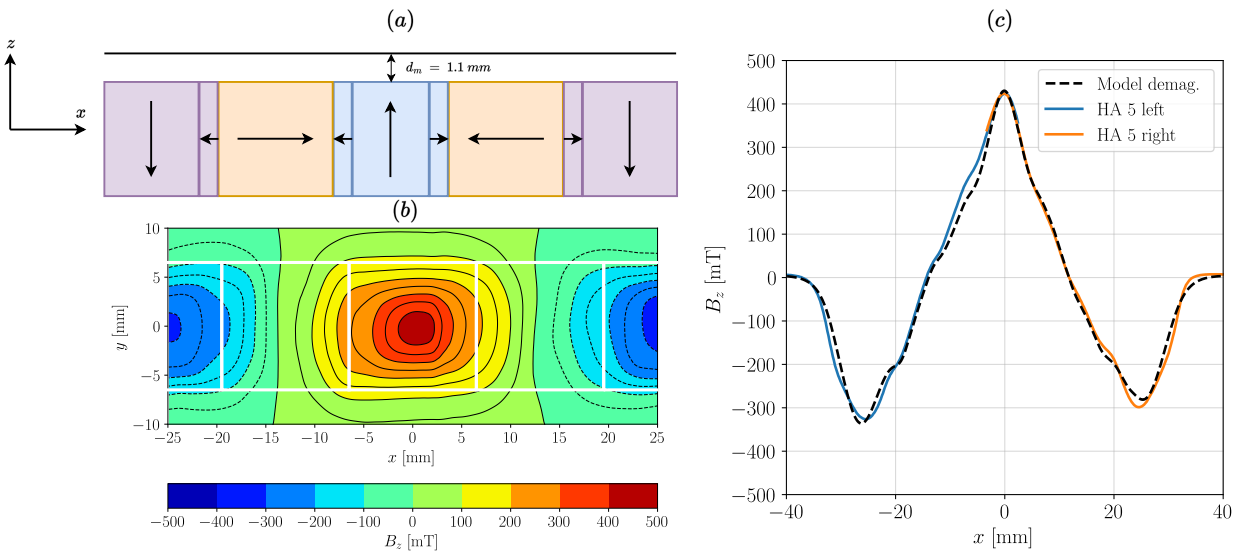

Figure 5.9: (a) Schematic illustration of the configuration with the arrows representing the direction of magnetization and the colours corresponds on the superconductors. (b) Mapping of Bz in the x-y plane carried out at a distance $d = 1.1$ mm. (c) Measurement of B_z in the x direction for the left and right part (blue and orange line) and comparison with the model (black dashed line).

of the curve differs significantly between the five-element configuration and both the three-element configuration and the single superconductor. In the five-element case, two shoulders appear on the left and right sides of the central peak. These shoulders are caused by the two end superconductors and are responsible for the extended region where the gradient remains above the threshold. However, the five-element configuration does not significantly increase the maximum gradient compared to the three-element configuration. The peak value reaches 2.8 T/m for the five-element array, while it was 2.7 T/m for the three-element version.

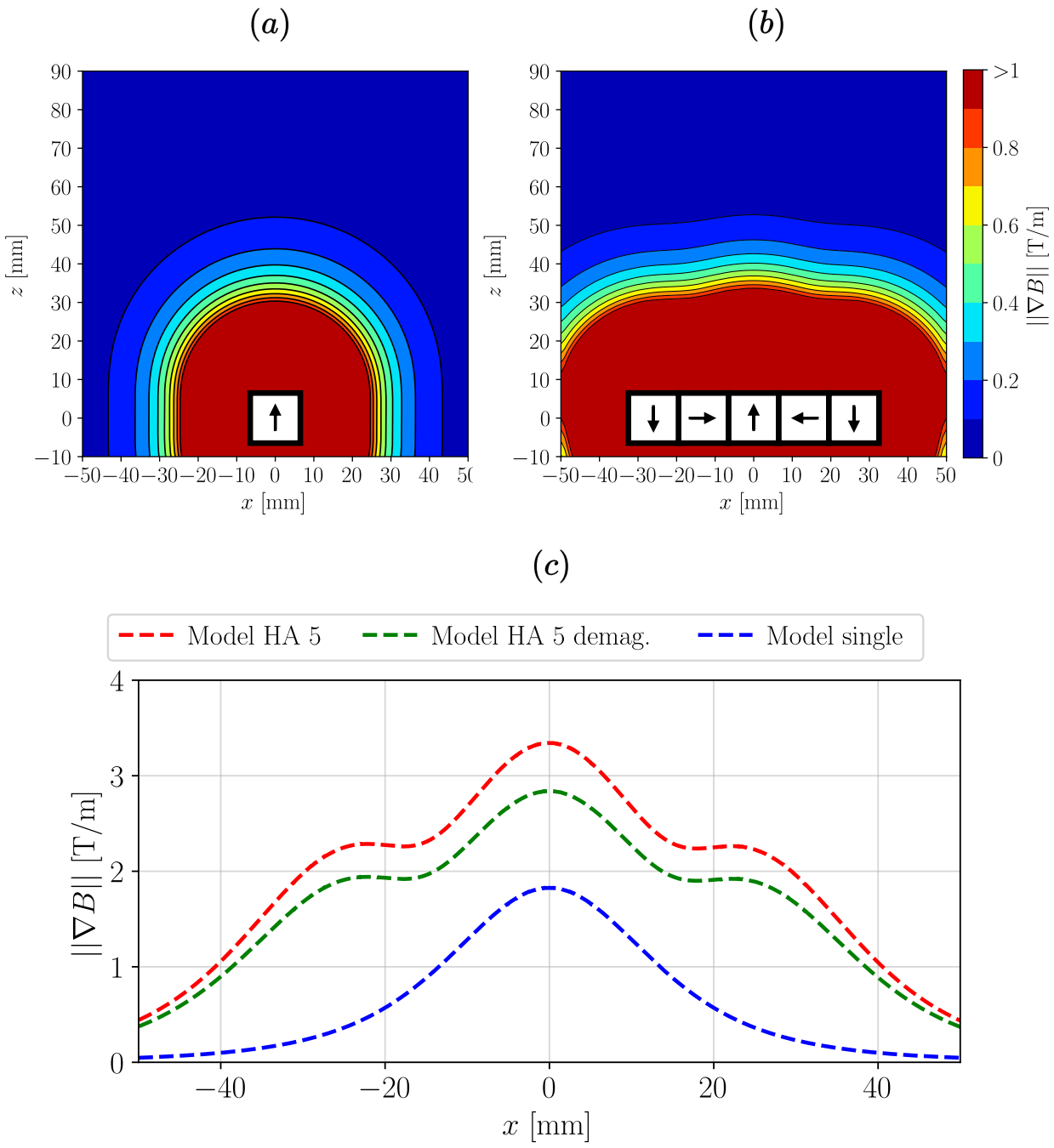

Figure 5.10: Magnetic gradient in the x-z plane for a single superconductor (a) and for an Halbach array of superconductors (b). Gradient at a distance d_m = 20 mm from the central superconductor along the x direction for a single superconductor and an Halbach array of superconductors (c).

5.3 Numerical comparison between permanent magnets and superconductors

Up to this point, no comparison has been made between the results obtained from the permanent magnet experiments (Nd-Fe-B) and those from the superconductor experiments (ATZ samples). Experimental results show that the norm of the magnetic field gradient is higher for the classical Halbach array made of permanent magnets, reaching a maximum value of 5.5 T/m, compared to 2.7 T/m for the superconducting array. These measurements were carried out using cubic samples with side lengths of 12 mm for the permanent magnets and 13 mm for the superconductors.

It is interesting to understand how both the magnetic field and the norm of its gradient evolve with the size l of the cubic sample. To enable this comparison, the analytical model is used to compute both the magnetic field and the norm of the magnetic gradient at a distance $d_m = 20$ mm from the top surface of the central superconductor. Several assumptions are made for this analysis. First, the surface current density K_c and the critical current density J_c are assumed to be 1.1×10^6 A/m and 2.5×10^8 A/m^2, respectively. Second, the superconductors are considered ideal, with a uniform critical current density throughout their volume. While this is a strong assumption, it is supported by results in [37], where a more uniform magnetic field distribution was achieved using improved fabrication methods. Third, since the comparison involves both single-sample experiments and Halbach array configurations, demagnetisation in the superconducting array must be taken into account. For a 13 mm sample, the demagnetised thickness t was experimentally found to be 1.3 mm. Given that demagnetisation occurs on both sides of the central superconductor, and the model assumes equal thickness on both sides, this results in two demagnetised regions of 1.3 mm each, representing approximately 20% of the central sample. As previously explained, the demagnetised thickness is expected to vary with the magnetic field induced by the lateral superconductors. According to the Bean model, the mean trapped field in an infinite slab is proportional to its thickness. In the case of a cubic superconductor, increasing the side length l should result in a proportionally stronger maximum trapped field, which in turn is expected to increase the demagnetised thickness. To reflect this scaling effect, the demagnetised thickness t is set to $l/10$ in simulations involving superconducting Halbach arrays.

Fig. 5.11 shows the evolution of the B_z component of the magnetic field as a function of the sample size l, measured at a distance $d_m = 20$ mm from the top surface, for various samples and configurations. First, it can be observed that a single permanent magnet produces a higher magnetic field than a single superconductor for sizes up to approximately 23 mm. Furthermore, the single permanent magnet also generates a stronger field than the superconducting Halbach array, at least for the sample sizes studied in this work. This behaviour changes when demagnetisation is not taken into account: in that case, the superconducting Halbach array surpasses the permanent magnet at a size of around 14 mm. When demagnetisation is included in the model, this crossover point shifts to approximately 17 mm. When comparing the superconducting configurations to the Halbach array made of permanent magnets, one sees that the latter remains more effective up to a size of 25 mm in the ideal (no demagnetisation) case, and up to 28 mm when demagnetisation is taken into account. Examining the graph more closely, it becomes apparent that the magnetic field B_z increases more rapidly with sample size in the superconducting configurations than in the permanent magnet ones. In the latter case, the curve tends to saturate, suggesting diminishing returns with increasing size. Another key advantage of superconductors is that their critical current density depends on temperature and increases as the system is cooled. For instance, if the current density is doubled compared to the value used in the other simulations, a single superconductor can generate a higher magnetic field than the superconducting Halbach array. In this case, it also outperforms the single permanent magnet for sizes

greater than 12.5 mm, which corresponds approximately to the size of the samples used in this master thesis. Finally, since the maximum magnetic field and gradient values for the five-superconductor configuration differ only slightly from those of the three-element configuration, the five-element case is not shown in Fig. 5.11 for clarity.

This saturation behaviour of permanent magnets, in contrast to the continued growth observed with superconductors, can also be explained analytically by examining the expressions of B_z above cylindrical samples. Cylindrical geometry is used here because fully analytical expressions are available for both permanent magnets and superconductors, as derived in [38]. For cubic samples, the model developed in Sec. 2.3 is only semi-analytical, since the third integral (in the case of superconductors) must be computed numerically. Consider a cylindrical sample of height h and diameter $2a$. The magnetic field above the surface of a permanent magnet is given by:

$$B_z(z) = \frac{1}{2}\mu_0 K_c \left[\frac{z+h}{\sqrt{a^2+(z+h)^2}} - \frac{z}{\sqrt{a^2+z^2}} \right], \tag{5.1}$$

for a distance $z > 0$ above the top surface. For a superconductor, the expression is:

$$B_z(z) = \frac{1}{2}\mu_0 J_c \left[(z+h)\ln\left(\frac{a+\sqrt{a^2+(z+h)^2}}{z+h} \right) - z\ln\left(\frac{a+\sqrt{a^2+z^2}}{z} \right) \right]. \tag{5.2}$$

To approximate the cubic sample case, we assume that the height and diameter are equal, i.e. $h = 2a$. In this configuration, the parameter $2a$ corresponds to the side length l of the cube. In the limit where the diameter $2a \to \infty$, the magnetic field above the surface of the permanent magnet tends to a constant saturation value: $\frac{K_c}{\sqrt{5}}$ In contrast, for the superconducting sample, the expression in Eq. 5.2 exhibits asymptotic linear behaviour. As a increases, the first term grows linearly, while the second term contains a logarithmic term that becomes negligible in comparison. Thus, the magnetic field for superconductors continues to increase with sample size, while it saturates for permanent magnets.

Regarding the norm of the magnetic field gradient, Fig. 5.12 presents the same configurations as before. The superconducting samples used in this master thesis do not allow for achieving a higher gradient than that generated by the permanent magnet. However, as the sample size increases, the gradient produced by the superconducting configurations continues to grow, while the gradient from the permanent magnet configuration tends to saturate. This difference can be explained by the distinct magnetic field profiles of superconductors and permanent magnets. In the case of superconductors, the trapped magnetic field has a conical shape, with its maximum at the centre along the x-direction. According to the Bean model, the average magnetic flux density trapped in a superconductor is proportional to the size of the sample. This explains the continued increase in the gradient with increasing l. For permanent magnets, the magnetic field profile along the x-axis resembles a step function above the magnet. As the magnet size increases, this step-like profile becomes slightly stronger but is mostly extended spatially rather than intensified. In the analytical model of the permanent magnet, where the magnetic field is generated by a surface current density K_c, increasing l also increases the distance between the lateral faces of the magnet and the point of interest. This reduces the influence of the surface current density at that point, causing the gradient to approach saturation.

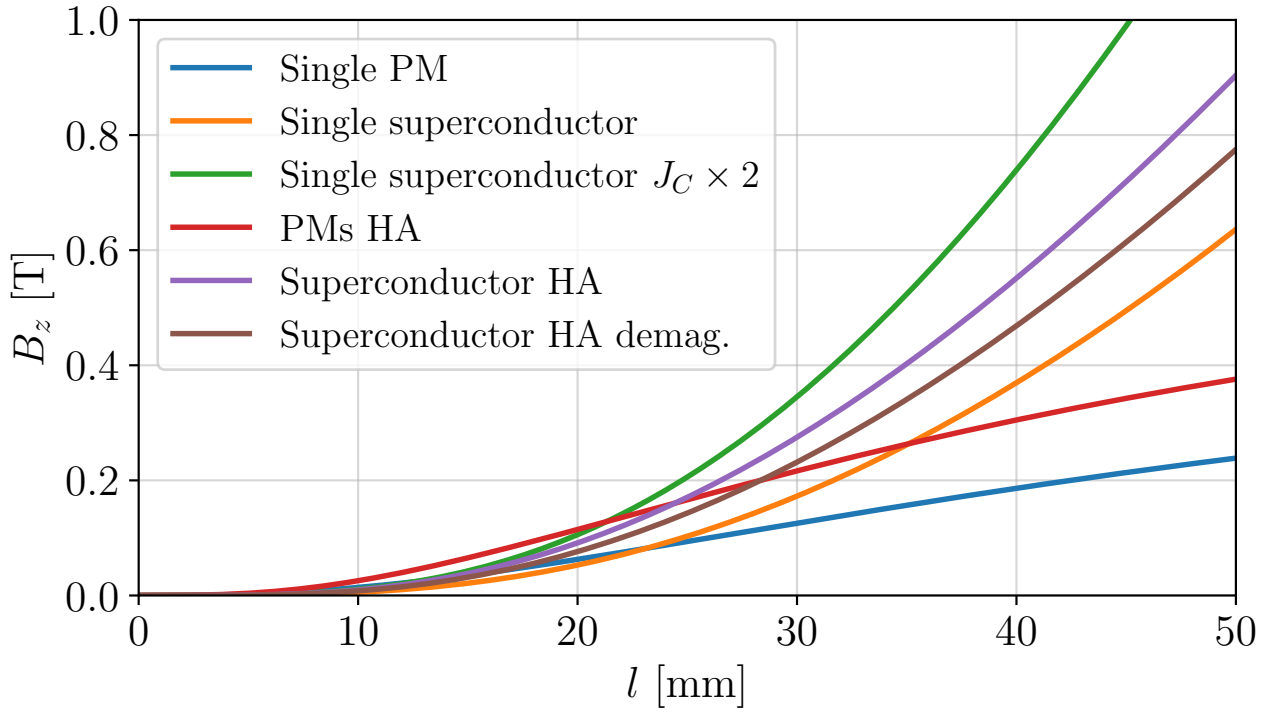

Figure 5.11: Flux density B_z at a distance $d_m = 20$ mm from the top surface as a function of the size of the sample l for different configurations of permanent magnet and superconductors.

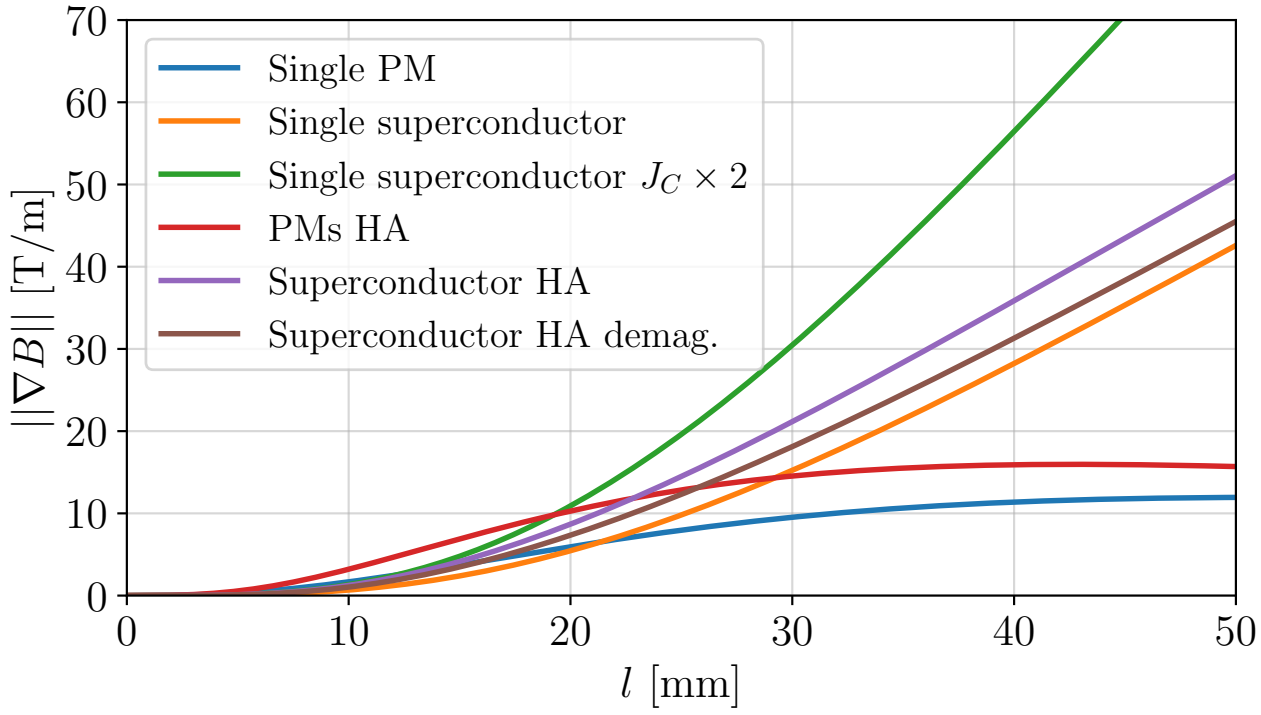

Figure 5.12: $||\nabla B||$ at a distance $d_m = 20$ mm from the top surface as a function of the size of the sample l for different configurations of permanent magnet and superconductors.

CHAPTER 6

Conclusion and perspectives

Conclusion

Halbach arrays are arrangements of permanent magnets with mutually perpendicular magnetization directions designed to increase both the flux density and the gradient of flux density on one side of the array. Although such arrays have been widely studied for conventional permanent magnets, it is only recently that such arrays were designed and fabricated with bulk superconductors acting as permanent magnets and called "bulk trapped field superconducting magnets". Compared to permanent magnets which are intrinsically limited by their saturation magnetization, bulk superconductors have the potential achieve much higher flux densities. In his PhD thesis [21] and the related journal paper [39], M. Houbart investigated for the first time methods to combine three bulk trapped field superconducting magnets to achieve large magnetic field gradients. The final goal is to obtain a system generating large gradient at a typical distance of ≈ 20 mm, i.e. a distance at which magnetic drug delivery can be achieved. This master thesis is the continuation of this work. Unlike the previous work where superconductors were fabricated at the University of Cambridge, the purpose here is to study, assemble and bulk superconductors commercially available from ATZ company. The final goal is to study new configurations that were never investigated experimentally : the elevated Halbach array and the linear Halbach array with five elements.

Chapter 2 presents the theoretical background on superconductors, along with the analytical models used to characterise the magnetic field generated by both permanent magnets and superconductors. The key point is that the magnetization of a bulk trapped field superconductor is caused by macroscopic, persistent current loops that are induced through a preliminary magnetization process. Although all the investigated samples have a cubic shape, it turns out that the commercially available superconductors have defects that impede the current flow. It results that the current loops do not flow in a uniform way over the sample cross section, which may differ from a square. The analytical models are extended to include the fact that current loops may flow in rectangular parts.

Chapter 3 focuses on the detailed characterisation of the various samples. For permanent magnets, the analytical model based on uniform surface currents shows a very good agreement with experimental data. This is not the case for superconductors that are expected to contain cracks and defects

that are mainly parallel to their a-b planes in which supercurrents flow. Although such defects have little impact on the flux density distribution above the faces parallel to the a-b planes, experimental results show that the possible cracks affect the flux density distribution close to the faces perpendicular to the a-b planes. For bulk superconductors that are neighbouring the central superconductor of a Halbach array, one of these lateral sides precisely faces the region of interest of the array. Such faces are therefore analysed to account for defects. The model is modified accordingly, representing superconductors as assemblies of superconducting and non-superconducting regions. The superconducting regions are modelled using the analytical approach introduced in Chapter 2. The model is found to reproduce satisfactorily the main non-idealities observed in the of the experimental magnetic flux distribution. In addition, potential sources of errors in the measurements are discussed, and their orders of magnitude are estimated.

Chapter 4 investigates a linear Halbach array composed of three commercially available superconductors. This chapter validates the model developed in Chapter 3 in the context of an assembled Halbach array. In this configuration, a partial demagnetisation of the central sample of the array is expected to occur. To highlight this behaviour, the superconductors are measured individually, and the sum of their measurements is used as a reference for the magnetic field in the absence of demagnetisation. First, the The model is compared to this sum and shows excellent agreement. Then, a "demagnetised thickness" t is introduced to simulate the partial demagnetization of the central sample. This thickness, experimentally determined by matching the maximum values of the model and the measurement, is found to be 1.3 mm, i.e. $\approx$ 20 % of the side of the cubic bulk superconductor as it happens at both side of the central superconductor. The demagnetisation leads to a reduction in the magnetic gradient compared to fully magnetized sample, similarly to previous works. In spite of the demagnetization and the non-idealities of the flux distribution, it is found that the region where the gradient exceeds 1 T/m is longer for the Halbach array than for a single superconductor.

Chapter 5 explores the two new configurations. The first, the elevated Halbach array, is designed to prevent the partial demagnetization of the central superconductor of the array. The analytical predictions are confirmed by experiments. Although the maximum magnetic gradient in this configuration is lower than that of a single superconductor, the region where the gradient exceeds 1 T/m is longer. Possible advantages of this configuration compared to the three-element classic Halbach array depends on which distance is considered from the array. At a given distance from the central superconductor, the region where the gradient exceeds a given threshold is larger, but this region at a given distance from the most elevated samples from the array, this region is shorter. The key advantage of the elevated configuration is the absence of demagnetization, rendering predictions easier with analytical expressions and no need to include any a priori unknown "demagnetization thickness" t. The second configuration, the Halbach array with five elements, is expected to exhibit demagnetisation in both the central superconductor and the two end elements. By using the same demagnetisation thickness t found in Chapter 3, the model shows good agreement with the experimental data. Regarding the magnetic gradient, the five-element configuration results in a region above the 1 T/m threshold that is almost twice as long as in the three-element case. However, the maximum gradient value remains nearly the same for both configurations. Relying on the satisfactory agreement between the theoretical predictions and the experimental data, the analytical model is then used to predict the amplitude of maximum flux density above a single sample and above the array consisting of three elements as a function of the size of the cubic permanent magnets and superconductors.

Perspectives

Superconducting Halbach arrays could potentially be improved by exploring various modifications. These modifications may concern both the geometry of the array and the geometry of the superconducting samples themselves. Fig. 6.1 illustrates some possible improvement strategies. In Fig. 6.1 (a), an elevated Halbach array is shown, with an elevation denoted by s. It has been observed that demagnetisation disappears when the lateral samples are elevated by a vertical shift s equal to the side length of the cubic sample. However, this also increases the measurement distance d_m. Therefore, a trade-off may exist between reducing or eliminating demagnetisation (by introducing a smaller shift than l) and limiting the increase in measurement distance. Finding an optimal value of s that balances both effects could be a valuable direction for future research. Fig. 6.1 (b) presents a new array design that may also help to avoid demagnetisation. In [21], an array using triangular samples on the left and right sides showed no signs of demagnetisation. The benefit brought by this absence of demagnetization was somehow overshadowed by the smaller flux density caused by the reduced amount of superconducting material. Using a trapezoidal central sample may yield a similar better result. Furthermore, since such a design would increase the size of the central sample and, consequently, the amount of trapped magnetic field. Both reduced demagnetisation and larger sample size could contribute to an increase in the magnetic gradient. Since various trapezoidal shapes are possible, numerical simulations exploring different angles θ could help identify at which point demagnetisation might start to occur. Finally, 6.1 (c), suggested in ref. [21] shows a configuration where the superconducting elements are placed in the same x–y plane. Although this arrangement is expected to experience demagnetisation, it could still offer advantages over a standard linear configuration. Studying experimentally this configuration would require substantial modifications of the experimental system to allow for a motion of magnetized samples in mutually perpendicular directions.

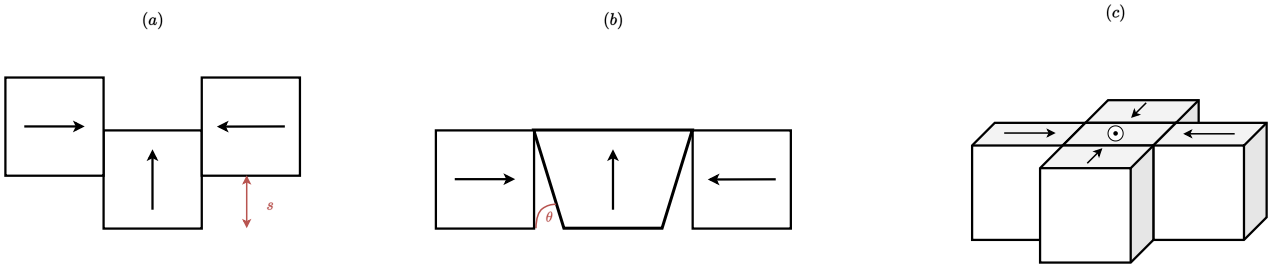

Figure 6.1: (a) Configuration where the shift s is studied. (b) Configuration where the parameter θ of the trapezoidal superconductor is studied. (c) 2D configuration in the x-y plane.

Results obtained in this work showed that the amplitudes of the flux density and the corresponding flux density gradients are comparable (and even smaller) than those obtained with permanent magnets. Keeping the operating temperature at 77 K, the first way of increasing the flux density is to use superconductors with less defects so that the critical current density can be considered as uniform throughout the sample. Recently, a new processing technique of bulk superconductors called 'single-direction melt growth (SDMG)' was developed [37]. Instead of relying on growth from a small seed single crystal placed on top of the pellet, the SDMG technique consists in using a large size bulk plate made of different rare earth element. The bulk superconductors processed this way have much more homogeneous superconducting properties. The second way of increasing the flux density is to increase the size of the sample. Since the typical maximum thickness (along the c axis) of the bulk pellets is of the order of that used in the present work ($\approx$ 10-15 mm), larger cubic samples should be made by stacking several bulk samples. Typical cylindrical materials with 60 mm diameter can be routinely fabricated, meaning that $\approx$ 30-40 mm side cubic elements could be obtained and assembled together.

If the mechanical system is able to counteract the forces between magnetized samples, theoretical results obtained in Chapter 5 show that such large samples offer the prospect of achieving gradients exceeding 15 T/m for samples larger than 30 mm.

APPENDIX A

Mathematical derivation of the x and z of $\vec{B}$ for a permanent magnet

A.1 Derivation of B_x

Starting from the Biot–Savart law for a surface current,

$$\vec{B} = \frac{\mu_0}{4\pi} \int\int_S \frac{\vec{K_c} \times (\vec{x_m} - \vec{x_p})}{||\vec{x_m} - \vec{x_p}||^3} \, ds, \tag{A.1}$$

, along the x-direction, and assuming K_c to be constant, this gives:

$$B_x = \frac{\mu_0 \times K_c}{4\pi} \int_{-\frac{l}{2}}^{\frac{l}{2}} \int_{-\frac{l}{2}}^{\frac{l}{2}} \frac{(z_p - z_m)}{\sqrt{(x_p - x_m)^2 + (y_p - y_m)^2 + (z_p - z_m)^2}^3} \, dy_m \, dz_m, \tag{A.2}$$

where l is the size of the cubic permanent magnet. By applying Fubini's theorem, this becomes:

$$B_x = \frac{\mu_0 \times K_c}{4\pi} \int_{-\frac{l}{2}}^{\frac{l}{2}} \int_{-\frac{l}{2}}^{\frac{l}{2}} \frac{(z_p - z_m)}{\sqrt{(x_p - \frac{l}{2})^2 + (y_p - y_m)^2 + (z_p - z_m)^2}^3} \, dz_m \, dy_m. \tag{A.3}$$

From this, it is possible to perform a change of variables,

$$u = (x_p - \frac{l}{2})^2 + (y_p - y_m)^2 + (z_p - z_m)^2 \tag{A.4}$$

$$du = -2(z_p - z_m) \tag{A.5}$$

The integral becomes,

$$B_x = \frac{\mu_0 \times K_c}{4\pi} \int_{-\frac{l}{2}}^{\frac{l}{2}} \int_{u_{low}}^{u_{up}} -\frac{1}{2} \frac{1}{\sqrt{u}^3} \, du \, dy_m. \tag{A.6}$$

where u_{up} and u_{low} represent the upper and lower limits of the integral for the variable u. The integral with respect to u can be solved.

$$B_x = \frac{\mu_0 \times K_c}{4\pi} \int_{-\frac{l}{2}}^{\frac{l}{2}} \left[\frac{1}{\sqrt{u}} \right]_{u_{low}}^{u_{up}} dy_m, \tag{A.7}$$

$$B_x = \frac{\mu_0 \times K_c}{4\pi} \int_{-\frac{l}{2}}^{\frac{l}{2}} \left[\frac{1}{\sqrt{(x_p - \frac{l}{2})^2 + (y_p - y_m)^2 + (z_p - z_m)^2}} \right]_{-\frac{l}{2}}^{\frac{l}{2}} dy_m. \tag{A.8}$$

Let α^2 be defined as:

$$\alpha^2 = (x_p - \frac{l}{2})^2 + (z_p - z_m)^2, \tag{A.9}$$

with $\alpha > 0$. The integral then becomes,

$$B_x = \frac{\mu_0 \times K_c}{4\pi} \int_{-\frac{l}{2}}^{\frac{l}{2}} \left[\frac{1}{\sqrt{\alpha^2 + (y_p - y_m)^2}} \right]_{-\frac{l}{2}}^{\frac{l}{2}} dy, \tag{A.10}$$

$$B_x = \frac{\mu_0 \times K_c}{4\pi} \int_{-\frac{l}{2}}^{\frac{l}{2}} \left[\frac{1}{\alpha} \frac{1}{\sqrt{1 + (\frac{y_p - y_m}{\alpha})^2}} \right]_{-\frac{l}{2}}^{\frac{l}{2}} dy_m. \tag{A.11}$$

Another change of variable can be performed for t,

$$t = \frac{y_p - y_m}{\alpha} \tag{A.12}$$

$$dt = -\frac{1}{\alpha}, \tag{A.13}$$

the integral becomes

$$B_x = \frac{\mu_0 \times K_c}{4\pi} \int_{t_{low}}^{t_{up}} \left[\frac{-1}{\sqrt{1 + (t)^2}} \right]_{-\frac{l}{2}}^{\frac{l}{2}} dt. \tag{A.14}$$

which can be solved and leads to,

$$B_x = -\frac{\mu_0 \times K_c}{4\pi} \left[[\sinh t]_{-\frac{l}{2}}^{\frac{l}{2}} \right]_{t_{low}}^{t_{up}}, \tag{A.15}$$

$$B_x = -\frac{\mu_0 \times K_c}{4\pi} \left[\left[\sinh \frac{y_p - y_m}{\alpha} \right]_{-\frac{l}{2}}^{\frac{l}{2}} \right]_{-\frac{l}{2}}^{\frac{l}{2}}, \tag{A.16}$$

$$B_x = -\frac{\mu_0 \times K_c}{4\pi} \left[\left[\sinh \frac{y_p - y_m}{\sqrt{(x_p - \frac{l}{2})^2 + (z_p - z_m)^2}} \right]_{-\frac{l}{2}}^{\frac{l}{2}} \right]_{-\frac{l}{2}}^{\frac{l}{2}}. \tag{A.17}$$

A.2 Derivation of B_z

Starting from the Biot–Savart law for a surface current,

$$\vec{B} = \frac{\mu_0}{4\pi} \int \int_S \frac{\vec{K_c} \times (\vec{x_m} - \vec{x_p})}{||\vec{x_m} - \vec{x_p}||^3} \, ds, \tag{A.18}$$

, along the z-direction, and assuming K_c to be constant, this gives,

$$B_z = -\frac{\mu_0 \times K_c}{4\pi} \int_{-\frac{l}{2}}^{\frac{l}{2}} \int_{-\frac{l}{2}}^{\frac{l}{2}} \frac{(x_p - \frac{l}{2})}{\sqrt{(x_p - \frac{l}{2})^2 + (y_p - y_m)^2 + (z_p - z_m)^2}^3} \, dy_m \, dz_m, \tag{A.19}$$

Let β be defined as

$$\beta^2 = (x_p - \frac{l}{2})^2 + (z_p - z_m)^2, \tag{A.20}$$

The integral becomes,

$$B_z = -\frac{\mu_0 \times K_c \times (x_p - \frac{l}{2})}{4\pi} \int_{-\frac{l}{2}}^{\frac{l}{2}} \int_{-\frac{l}{2}}^{\frac{l}{2}} \frac{1}{\sqrt{\beta^2 + (y_p - y_m)^2}^3} \, dy_m \, dz_m, \tag{A.21}$$

$$B_z = -\frac{\mu_0 \times K_c \times (x_p - \frac{l}{2})}{4\pi} \int_{-\frac{l}{2}}^{\frac{l}{2}} \int_{-\frac{l}{2}}^{\frac{l}{2}} \frac{1}{\beta^3} \frac{1}{\sqrt{1 + \left(\frac{y_p - y_m}{\beta}\right)^2}^3} \, dy_m \, dz_m, \tag{A.22}$$

It is possible to perform a change of variables, such as

$$, \frac{y_p - y_m}{\beta} = \tan t \tag{A.23}$$

$$t = \arctan \frac{y_p - y_m}{\beta} \tag{A.24}$$

$$-\frac{1}{\beta} dy_m = \frac{1}{\cos^2 t} dt, \tag{A.25}$$

The integral with respect to t becomes:

$$B_x = \frac{\mu_0 \times K_c \times (x_p - \frac{l}{2})}{4\pi} \int_{-\frac{l}{2}}^{\frac{l}{2}} \int_{t_{low}}^{t_{up}} \frac{1}{\beta^2} \frac{1}{\sqrt{1 + (\tan t)^2}^3} \frac{1}{\cos^2 t} dt \, dz_m, \tag{A.26}$$

$$B_z = \frac{\mu_0 \times K_c \times (x_p - \frac{l}{2})}{4\pi} \int_{-\frac{l}{2}}^{\frac{l}{2}} \int_{t_{low}}^{t_{up}} \frac{1}{\beta^2} \frac{1}{\sqrt{\frac{1}{\cos^2 t}}^3} \frac{1}{\cos^2 t} dt \, dz_m, \tag{A.27}$$

$$B_z = \frac{\mu_0 \times K_c \times (x_p - \frac{l}{2})}{4\pi} \int_{-\frac{l}{2}}^{\frac{l}{2}} \int_{t_{low}}^{t_{up}} \frac{1}{\beta^2} \frac{1}{\sqrt{1 + (\tan t)^2}^3} \frac{1}{\cos^2 t} dt \, dz_m, \tag{A.28}$$

$$B_z = \frac{\mu_0 \times K_c \times (x_p - \frac{l}{2})}{4\pi} \int_{-\frac{l}{2}}^{\frac{l}{2}} \int_{t_{low}}^{t_{up}} \frac{\cos t}{\beta^2} dt \, dz_m, \tag{A.29}$$

$$B_z = \frac{\mu_0 \times K_c \times (x_p - \frac{l}{2})}{4\pi} \int_{-\frac{l}{2}}^{\frac{l}{2}} \left[\frac{\sin t}{\beta^2}\right]_{t_{low}}^{t_{up}} dz_m, \tag{A.30}$$

$$B_z = \frac{\mu_0 \times K_c \times (x_p - \frac{l}{2})}{4\pi} \int_{-\frac{l}{2}}^{\frac{l}{2}} \left[\frac{\sin t}{\beta^2}\right]_{t_{low}}^{t_{up}} dz_m, \tag{A.31}$$

$$B_z = \frac{\mu_0 \times K_c \times (x_p - \frac{l}{2})}{4\pi} \int_{-\frac{l}{2}}^{\frac{l}{2}} \left[\frac{\sin\left(\arctan \frac{y_p - y_m}{\beta}\right)}{\beta^2}\right]_{-\frac{l}{2}}^{\frac{l}{2}} dz_m, \tag{A.32}$$

The last expression, $\sin\left(\arctan\left(\frac{y_p - y_m}{\beta}\right)\right)$, can be rewritten as follows:

$$\sin\left(\arctan\frac{y_p-y_m}{\beta}\right)=\frac{\frac{y_p-y_m}{\beta}}{\sqrt{1+\left(\frac{y_p-y_m}{\beta}\right)^2}} \tag{A.33}$$

The integral becomes,

$$B_z=\frac{\mu_0\times K_c\times(x_p-\frac{l}{2})}{4\pi}\int_{-\frac{l}{2}}^{\frac{l}{2}}\left[\frac{1}{\beta^2}\frac{\frac{y_p-y_m}{\beta}}{\sqrt{1+\left(\frac{y_p-y_m}{\beta}\right)^2}}\right]_{-\frac{l}{2}}^{\frac{l}{2}}dz_m, \tag{A.34}$$

$$B_z=\frac{\mu_0\times K_c\times(x_p-\frac{l}{2})}{4\pi}\int_{-\frac{l}{2}}^{\frac{l}{2}}\left[\frac{y_p-y_m}{\beta^3}\frac{1}{\sqrt{1+\left(\frac{y_p-y_m}{\beta}\right)^2}}\right]_{-\frac{l}{2}}^{\frac{l}{2}}dz_m, \tag{A.35}$$

$$B_z=\frac{\mu_0\times K_c\times(x_p-\frac{l}{2})}{4\pi}\int_{-\frac{l}{2}}^{\frac{l}{2}}\left[\frac{y_p-y_m}{\beta^2}\frac{1}{\sqrt{\beta^2+\left(\frac{y_p-y_m}{\beta}\right)^2}}\right]_{-\frac{l}{2}}^{\frac{l}{2}}dz_m, \tag{A.36}$$

$$B_z=\frac{\mu_0\times K_c\times(x_p-\frac{l}{2})}{4\pi}\int_{-\frac{l}{2}}^{\frac{l}{2}}\left[\frac{y_p-y_m}{(x_p-\frac{l}{2})^2+(z_p-z_m)^2}\frac{1}{\sqrt{(x_p-\frac{l}{2})^2+(z_p-z_m)^2+(y_p-y_m)^2}}\right]_{-\frac{l}{2}}^{\frac{l}{2}}dz_m, \tag{A.37}$$

For simplicity, let

$$a=x_p-\frac{l}{2} \tag{A.38}$$

$$b=y_p-y_m \tag{A.39}$$

The integral becomes

$$B_z=\frac{\mu_0\times K_c\times(a)}{4\pi}\int_{-\frac{l}{2}}^{\frac{l}{2}}\left[\frac{b}{(a)^2+(z_p-z_m)^2}\frac{1}{\sqrt{(a)^2+(z_p-z_m)^2+(b)^2}}\right]_{-\frac{l}{2}}^{\frac{l}{2}}dz_m, \tag{A.40}$$

(A.41)

From this, it is possible to apply the following change of variables,

$$t=z_p-z_m \tag{A.42}$$

$$dt=-dz_m, \tag{A.43}$$

B_z becomes

$$B_z=-\frac{\mu_0\times K_c\times(a)}{4\pi}\int_{t_{low}}^{t_{up}}\left[\frac{b}{(a)^2+(t)^2}\frac{1}{\sqrt{(a)^2+(b)^2+(t)^2}}\right]_{-\frac{l}{2}}^{\frac{l}{2}}dt, \tag{A.44}$$

(A.45)

Another change of variables is possible here.

$$t = \sqrt{a^2+b^2}\tan u \tag{A.46}$$

$$dt = \sqrt{a^2+b^2}\frac{1}{\cos^2 u}du \tag{A.47}$$

Which leads to

$$B_z = -\frac{\mu_0 \times K_c \times (a)}{4\pi}\int_{u_{low}}^{u_{up}}\left[\frac{b}{(a)^2+(a^2+b^2)\tan^2 u}\frac{1}{\sqrt{(a)^2+(b)^2+(a^2+b^2)\tan^2 u}}\frac{\sqrt{a^2+b^2}}{\cos^2 u}\right]_{-\frac{l}{2}}^{\frac{l}{2}}du, \tag{A.48}$$

$$B_z = -\frac{\mu_0 \times K_c \times (a)}{4\pi}\int_{u_{low}}^{u_{up}}\left[\frac{b}{(a)^2+(a^2+b^2)\tan^2 u}\frac{1}{\sqrt{(a^2+b^2)\times(1+\tan^2 u)}}\frac{\sqrt{a^2+b^2}}{\cos^2 u}\right]_{-\frac{l}{2}}^{\frac{l}{2}}du, \tag{A.49}$$

$$B_z = -\frac{\mu_0 \times K_c \times (a)}{4\pi}\int_{u_{low}}^{u_{up}}\left[\frac{b}{(a)^2+(a^2+b^2)\tan^2 u}\frac{1}{\sqrt{(a^2+b^2)\times(\frac{1}{\cos^2 u})}}\frac{\sqrt{a^2+b^2}}{\cos^2 u}\right]_{-\frac{l}{2}}^{\frac{l}{2}}du, \tag{A.50}$$

$$B_z = -\frac{\mu_0 \times K_c \times (a)}{4\pi}\int_{u_{low}}^{u_{up}}\left[\frac{b}{(a)^2+(a^2+b^2)\tan^2 u}\frac{\cos u}{\sqrt{(a^2+b^2)}}\frac{\sqrt{a^2+b^2}}{\cos^2 u}\right]_{-\frac{l}{2}}^{\frac{l}{2}}du, \tag{A.51}$$

$$B_z = -\frac{\mu_0 \times K_c \times (a)}{4\pi}\int_{u_{low}}^{u_{up}}\left[\frac{b}{(a)^2(1+\tan^2 u)+b^2\tan^2 u}\frac{\cos u}{1}\frac{1}{\cos^2 u}\right]_{-\frac{l}{2}}^{\frac{l}{2}}du, \tag{A.52}$$

$$B_z = -\frac{\mu_0 \times K_c \times (a)}{4\pi}\int_{u_{low}}^{u_{up}}\left[\frac{b}{(a)^2\left(\frac{1}{\cos^2 u}\right)+b^2\frac{\sin^2 u}{\cos^2 u}}\frac{\cos u}{1}\frac{1}{\cos^2 u}\right]_{-\frac{l}{2}}^{\frac{l}{2}}du, \tag{A.53}$$

$$B_z = -\frac{\mu_0 \times K_c \times (a)}{4\pi}\int_{u_{low}}^{u_{up}}\left[\frac{b}{(a)^2+b^2\sin^2 u}\cos u\right]_{-\frac{l}{2}}^{\frac{l}{2}}du, \tag{A.54}$$

With another change of variables,

$$v = \sin u \tag{A.55}$$

$$dv = \cos u, \tag{A.56}$$

It becomes,

$$B_z = -\frac{\mu_0 \times K_c \times (a)}{4\pi}\int_{v_{low}}^{v_{up}}\left[\frac{b}{(a)^2+(b^2)v^2}\right]_{-\frac{l}{2}}^{\frac{l}{2}}dv \tag{A.57}$$

$$B_z = -\frac{\mu_0 \times K_c}{4\pi}\int_{v_{low}}^{v_{up}}\frac{1}{a}\left[\frac{b}{1+(\frac{bv}{a})^2}\right]_{-\frac{l}{2}}^{\frac{l}{2}}dv \tag{A.58}$$

Another change of variables can be applied,

$$w = \frac{b\,v}{a} \tag{A.59}$$

$$dw = \frac{b}{a} dv \tag{A.60}$$

It becomes

$$B_z = -\frac{\mu_0 \times K_c}{4\pi} \int_{w_{low}}^{w_{up}} \left[\frac{1}{1+(w)^2} \right]_{-\frac{l}{2}}^{\frac{l}{2}} dw \tag{A.61}$$

$$B_z = -\frac{\mu_0 \times K_c}{4\pi} \left[[\tan w]_{-\frac{l}{2}}^{\frac{l}{2}} \right]_{w_{low}}^{w_{up}} \tag{A.62}$$

$$B_z = -\frac{\mu_0 \times K_c}{4\pi} \left[\left[\tan \frac{b\,v}{a} \right]_{-\frac{l}{2}}^{\frac{l}{2}} \right]_{v_{low}}^{v_{up}} \tag{A.63}$$

$$B_z = -\frac{\mu_0 \times K_c}{4\pi} \left[\left[\tan \frac{b\,\sin u}{a} \right]_{-\frac{l}{2}}^{\frac{l}{2}} \right]_{u_{low}}^{u_{up}} \tag{A.64}$$

$$B_z = -\frac{\mu_0 \times K_c}{4\pi} \left[\left[\tan \frac{b\,\sin\left(\arctan \frac{t}{\sqrt{a^2+b^2}}\right)}{a} \right]_{-\frac{l}{2}}^{\frac{l}{2}} \right]_{t_{low}}^{t_{up}} \tag{A.65}$$

Using the same relation as in Eq. A.33, it becomes:

$$B_z = -\frac{\mu_0 \times K_c}{4\pi} \left[\left[\tan \frac{b}{a} \frac{\frac{t}{\sqrt{a^2+b^2}}}{\sqrt{1+\left(\frac{t}{\sqrt{a^2+b^2}}\right)^2}} \right]_{-\frac{l}{2}}^{\frac{l}{2}} \right]_{t_{low}}^{t_{up}} \tag{A.66}$$

$$B_z = -\frac{\mu_0 \times K_c}{4\pi} \left[\left[\tan \frac{b}{a} \frac{t}{\sqrt{a^2+b^2+t^2}} \right]_{-\frac{l}{2}}^{\frac{l}{2}} \right]_{t_{low}}^{t_{up}} \tag{A.67}$$

$$B_z = -\frac{\mu_0 \times K_c}{4\pi} \left[\left[\tan \frac{(y_p - y_m)}{(x_p - \frac{l}{2})} \frac{(z_p - z_m)}{\sqrt{(x_p - \frac{l}{2})^2 + (y_p - y_m)^2 + (z_p - z_m)^2}} \right]_{-\frac{l}{2}}^{\frac{l}{2}} \right]_{-\frac{l}{2}}^{\frac{l}{2}} \tag{A.68}$$

Eqs. A.17 and A.68 can be modified to match the expression given in [21].

APPENDIX B

Mapping of the superconducting sample

Fig. B.1 Shows different mapping of B_z in the x-y plane of the superconducting sample. The measurement is carried out at a distance d_m = 2.5 mm from the top surface of each.

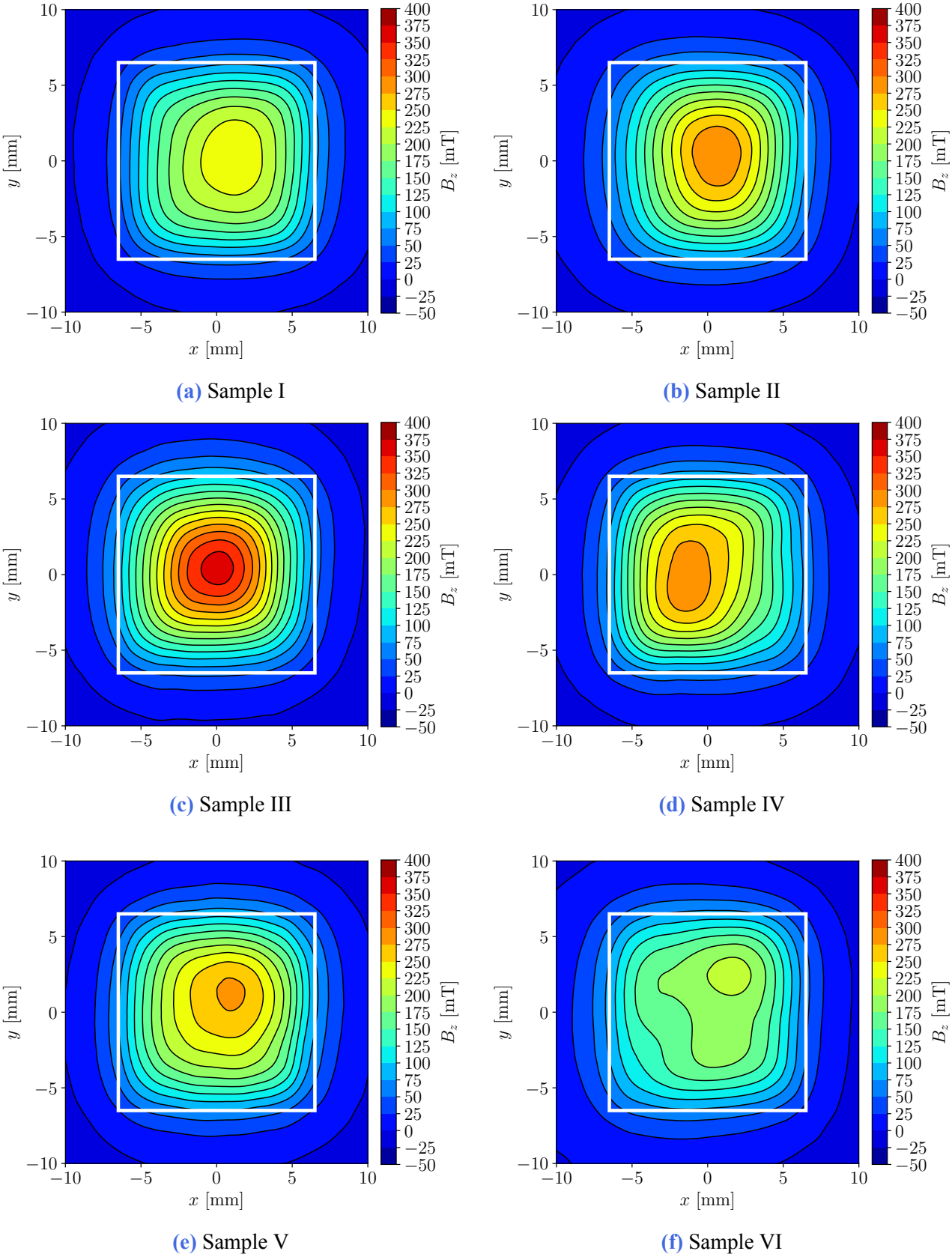

(a) Sample I

(b) Sample II

(c) Sample III

(d) Sample IV

(e) Sample V

(f) Sample VI

Figure B.1: Mapping of B_z in the x-y plane for each sample at a distance d_m = 2.5 mm.

Bibliography

1. Senapati, S., Mahanta, A. K., Kumar, S. & Maiti, P. Controlled drug delivery vehicles for cancer treatment and their performance. *Signal Transduction and Targeted Therapy* **3,** 7 (2018).
2. Alexiou, C. *et al.* A High Field Gradient Magnet for Magnetic Drug Targeting. *IEEE Transactions on Applied Superconductivity* **16,** 1527–1530 (2006).
3. Gleich, B. *et al.* Design and Evaluation of Magnetic Fields for Nanoparticle Drug Targeting in Cancer. *IEEE Transactions On Nanotechnology* **6,** 164–170 (2007).
4. Pankhurst, Q. A., Connolly, J., Jones, S. K. & Dobson, J. Applications of magnetic nanoparticles in biomedicine. *Journal of Physics* (2003).
5. Mallinson, J. One-sided fluxes – A magnetic curiosity? en. *IEEE Transactions on Magnetics* **9,** 678–682 (1973).
6. Halbach, K. Design of permanent multipole magnets with oriented rare earth cobalt material. *Nuclear Instruments and Methods* **169,** 1–10 (1980).
7. Halbach, K. Physical and optical properties of rare earth cobalt magnets. *Nuclear Instruments and Methods in Physics Research* **187,** 109–117 (1981).
8. Seok-Myeong Jang, Sang-Sub Jeong & Sang-Do Cha. The application of linear Halbach array to eddy current rail brake system. *IEEE Transactions on Magnetics* **37,** 2627–2629 (2001).
9. Bala, M. J., Roy, D. & Sengupta, A. *The Performance Enhancement of BLDC Motor Using Halbach Array Rotor* in *2020 IEEE 1st International Conference for Convergence in Engineering (ICCE)* (IEEE, Kolkata, India, 2020), 405–409.
10. Praveen, R. P. *et al.* A Novel Slotless Halbach-Array Permanent-Magnet Brushless DC Motor for Spacecraft Applications. *IEEE Transactions on Industrial Electronics* **59,** 3553–3560 (2012).
11. Hyung-Woo Lee, Ki-Chan Kim & Ju Lee. Review of maglev train technologies. *IEEE Transactions on Magnetics* **42,** 1917–1925 (2006).
12. Kang, J. H., Driscoll, H., Super, M. & Ingber, D. E. Application of a Halbach magnetic array for long-range cell and particle separations in biological samples. *Applied Physics Letters* **108,** 213702 (2016).
13. Barnsley, L. C., Carugo, D., Owen, J. & Stride, E. Halbach arrays consisting of cubic elements optimised for high field gradients in magnetic drug targeting applications. en. *Physics in Medicine and Biology* **60,** 8303–8327 (Nov. 2015).
14. Fohr, F. & Volbers, N. A high-saturation Fe-27Co material with microalloying additions. *AIP Advances* **8,** 047701 (2018).
15. Brown, D., Ma, B.-M. & Chen, Z. Developments in the processing and properties of NdFeb-type permanent magnets. *Journal of Magnetism and Magnetic Materials* (2002).

16. Bjørk, R. & Insinga, A. R. Explaining Browns paradox in NdFeB magnets from micromagnetic simulations. *Journal of Magnetism and Magnetic Materials* **571,** 170510 (2023).
17. De Andrade, R. *et al.* A superconducting high-speed flywheel energy storage system. *Physica C: Superconductivity* **408-410,** 930–931 (2004).
18. Durrell, J. H. *et al.* Bulk superconductors: a roadmap to applications. *Superconductor Science and Technology* **31,** 103501 (2018).
19. Hull, J. & Murakami, M. Applications of bulk high-temperature Superconductors. *Proceedings of the IEEE* **92,** 1705–1718 (2004).
20. Tomita, M. & Murakami, M. High-temperature superconductor bulk magnets that can trap magnetic fields of over 17 tesla at 29 K. *Nature* **421,** 517–520 (2003).
21. Houbart, M. *Investigation of methods for combining several trapped field superconducting magnets to obtain large magnetic field gradients* PhD thesis (University of liège, 2024).
22. Orlando, T. P. & Delin, K. A. *Foundations of applied superconductivity* 612 pp. (1990).
23. Kamerlingh Onnes, H. Further experiments with liquid helium. C. On the change of electric resistance of pure metals at very low temperatures, etc. IV. The resistance of pure mercury at helium temperatures. *Communications from the Physical Laboratory of the University of Leiden* **120b,** 1–14 (1911).
24. Abrikosov, A. A. Nobel Lecture: Type-II superconductors and the vortex lattice. *Reviews of Modern Physics* **76,** 975–979 (2004).
25. Bean, C. P. Magnetization of Hard Superconductors. *Physical Review Letters* **8,** 250–253 (1962).
26. Bean, C. P. Magnetization of High-Field Superconductors. *Review of Modern Physics* **36,** 31–39 (1964).
27. Wimbush, S. C. & Strickland, N. M. A Public Database of High-Temperature Superconductor Critical Current Data. *IEEE Transactions on Applied Superconductivity* **27,** 1–5 (2017).
28. Strickland, N. M., Hoffmann, C. & Wimbush, S. C. A 1 kA-class cryogen-free critical current characterization system for superconducting coated conductors. *Review of Scientific Instruments* **85,** 113907 (2014).
29. Cardwell, D. *et al.* Round robin measurements of the flux trapping properties of melt processed Sm–Ba–Cu–O bulk superconductors. *Physica C: Superconductivity* **412-414,** 623–632 (2004).
30. Yamasaki, H. & Mawatari, Y. Current–voltage characteristics and flux creep in melt-textured $YBa_2C_3O_{7-\delta}$. *Superconductor Science and Technology,* 202–208 (2000).
31. Zhang, X. *et al.* Study of Critical Current and n-Values of 2G HTS Tapes: Their Magnetic Field-Angular Dependence. *Journal of Superconductivity and Novel Magnetism* **31,** 3847–3854 (2018).
32. Baumann, J., Shi, Y., Weerakonda, D., Durrell, J. H. & Cardwell, D. A. Understanding the porosity and its effects on the superconducting properties of YBCO single grains. *Journal of the European Ceramic Society* **43,** 1542–1547 (2023).
33. Dusoulier, L. *et al.* Interactions in $YBa_2Cu_3O_{7-x}$ aqueous suspensions. *Materials Chemistry and Physics* **116,** 368–375 (2009).
34. Li, Z., Ida, T., Miki, M. & Izumi, M. Trapped Flux Behavior in Melt-Growth GdBCO Bulk Superconductor Under Off-Axis Field Cooled Magnetization. *IEEE Transactions on Applied Superconductivity* **27,** 1–4 (2017).
35. Vanderbemden, P. *et al.* Superconducting properties of natural and artificial grain boundaries in bulk melt-textured YBCO. *Physica C: Superconductivity* **302,** 257–270 (1998).
36. Gyorgy, E. M., Van Dover, R. B., Jackson, K. A., Schneemeyer, L. F. & Waszczak, J. V. Anisotropic critical currents in $Ba_2YCu_3O_7$ analyzed using an extended Bean model. *Applied Physics Letters* **55,** 283–285 (1989).

37. Motoki, T., Yanai, Y., Nunokawa, K. & Shimoyama, J.-i. Fabrication of high-performance YBa_2Cu_3 Oy melt-textured bulks with selective grain growth. *Applied Physics Express* **13,** 093002 (2020).
38. Chen, I.-G., Liu, J., Weinstein, R. & Lau, K. Characterization of YBa2Cu3O7, including critical current density *J c* , by trapped magnetic field. *Journal of Applied Physics* **72,** 1013–1020 (1992).
39. Houbart, M. *et al.* Trapped magnetic field distribution above a superconducting linear Halbach array. *Superconductor Science and Technology* **35,** 064005 (2022).